NASA Contractor Report 3671

End Wall Flow Characteristics and Overall Performance of an Axial Flow Compressor Stage

N. Sitaram and B. Lakshminarayana

GRANT NSG-3032
FEBRUARY 1983

NASA

NASA Contractor Report 3671

End Wall Flow Characteristics and Overall Performance of an Axial Flow Compressor Stage

N. Sitaram and B. Lakshminarayana
The Pennsylvania State University
University Park, Pennsylvania

Prepared for
Lewis Research Center
under Grant NSG-3032

National Aeronautics
and Space Administration

Scientific and Technical Information Branch

1983

SUMMARY

The existing literature on the complex endwall flows in the axial flow turbomachines is reviewed critically. This review also indicates the possible future directions for research on endwall flows in axial flow compressors.

Theoretical investigations on the rotor blade endwall flows in axial flow compressors reported here include the secondary flow calculation and the development of the momentum integral equations for the prediction of the annulus wall boundary layer. The equations for secondary vorticity at the rotor exit are solved analytically. The solution includes the effects of rotation and the viscosity. The momentum integral equations derived include the effect of the blade boundary layers.

The axial flow compressor facility of the Department of Aerospace Engineering at The Pennsylvania State University, which is used for the experimental investigations of the endwall flows, is described in some detail. The overall performance and other preliminary experimental results are presented. Extensive radial flow surveys are carried out at the design and various off design conditions. These are presented and interpreted in this report.

The following experimental investigations of the blade endwall flows are carried out.

1. Rotor blade endwall flows: The following measurements are carried out at four flow coefficients. (a) The rotor blade static pressures at various axial and radial stations (with special emphasis near the blade tips). (b) The hub wall static pressures inside the rotor blade passage at various axial and tangential stations.

2. IGV endwall flows: The following measurements are carried out at the design flow coefficient. (a) The boundary layer profiles at various axial and tangential stations inside the blade passage and at the blade exit. These measurements are made with a five-hole probe of very small diameter (1.65 mm) head. The static and stagnation pressures and three components of mean velocities are obtained. (b) Casing static pressures and limiting streamline angles inside the blade passage.

All these measurements are presented and interpreted in this report. The secondary flow is found to be strong in the inlet guidevane. Substantial effects of tip clearance are observed in the blade pressure distribution taken in the tip region of the blade.

TABLE OF CONTENTS

NOMENCLATURE

AVR	axial velocity ratio
$a_{b'}, a_{n'}$	distance between neighboring streamlines in b' and n' directions, respectively
B	blockage factor due to blade thickness coefficient of secondary loss correlation
C	blade chord, m (in.)
C_D	drag coefficient
C_f	skin friction coefficient
C_ℓ	lift coefficient
C_{ℓ_o}	camber expressed as design lift coefficient of an isolated airfoil
C_p	static pressure coefficient = $(p_\ell - p_1)/q_1$
$C_{p_{loss}}$	stagnation pressure loss coefficient, $(P_{o_1} - P_{o_\ell})/q_e$
$C'_{p_{loss}}$	stagnation pressure loss coefficient, $2(P_{o_1} - P_{o_\ell})/\rho U_t^2$
$C_{p_{pitch}}$	$(P_4 - P_5)/D$, Figs. 27 and 28
C_{p_s}	static pressure coefficient, $(p_\ell - p_a)/q_e$
$C_{p_{static}}$	$(\bar{P} - p)/D$, Figs. 27 and 28
$C_{p_{total}}$	$(P_1 - P_o)/D$, Figs. 27 and 28
$C_{p_{yaw}}$	$(P_2 - P_3)/D$, Figs. 27 and 28
C_{p_o}	stagnation pressure coefficient $(P_{o_\ell} - p_a)/q_e$
C_1, C_2, C_3, C_4	constants used in equivalent diffusion factor definition. Their values depend on blade type.
D	$(P_1 - \bar{P})$
D_{eq}	equivalent diffusion factor, $= \cos\beta_2/\cos\beta_1 \{C_1 + C_2(i - i_{ref})C_3 + C_4 \cos^2\beta_1/\sigma \; V_{x_1} (W_{\theta_1} - W_{\theta_2})\}$
D_f	force defect
F	blade force per unit span
H	shape factor = δ^*/θ^*

h	blade span, m
i	blade incidence, degrees
K	ratio of circulation at the blade tip/circulation at the mid span/constant of proportionality
N_B	number of blades
P_o	stagnation pressure, N/m^2
$\bar{P}$	average of side holes of five hole probe, $(P_2 + P_3 + P_4 + P_5)/4$, N/m^2 (Figs. 27 and 28)
p	static pressure, N/m^2 (psi)
PS, SS	pressure and suction surface, respectively
q	dynamic pressure based on inlet relative velocity for rotor (inlet absolute velocity for stationary blade rows)
R	nondimensional radius = r/r_t
	radius of curvature of blade camber line, m (ft)
Re	Reynolds number
r	radius, m (ft.)
r,θ,x	cylindrical coordinate system
S	throttle spacing, m
s	blade spacing, m (ft.)
s,n,b	intrinsic coordinate system
s,n,r	streamline coordinate system, s is along the projection of the external (or edge of the annulus wall boundary layer) streamline on the cylindrical surface, n is normal to it in that plane, and r is in the radial direction
T	turbulence intensity normalized by free stream velocity
t	blade maximum thickness, m (ft.)
U	rotor blade speed, m/sec (ft./sec)
V	velocity, m/sec (ft./sec)
V_b	belt speed, m/sec
V_τ	friction velocity, m/sec ($\sqrt{\tau_o/\rho}$)

W	relative velocity, m/sec
X	axial distance from the leading edge, m (ft.)
x,y,z	rectangular coordinate system
x,θ,r	axial, tangential, and radial coordinate system, respectively
YS	normalized distance (w.r.t local blade spacing) along tangential direction
Z	nondimensionalized axial distance from the leading edge $= X/C_{x_t}$
α	pitch angle from five hole probe, degrees absolute flow angle, degrees, $= \tan^{-1}(V_\theta/V_x)$
β	relative flow angle, degrees $= \tan^{-1}(W_\theta/V_x)$ yaw angle from five hole probe, degrees
β^*	blade angle, degrees
Γ	blade circulation
δ	boundary layer thickness, m (ft.) flow deviation angle, degrees
δ^*	boundary layer displacement thickness, m (ft.), Appendix B
ε	limiting streamline angle, degrees
ζ	rotor stagnation pressure loss coefficient (based on inlet dynamic head of the flow); relative vorticity, radians/sec
η	efficiency
θ	distance from the blade suction surface, degrees blade turning angle, degrees
θ^*	boundary layer momentum thickness, m (ft.), Appendix B
λ	blade stagger angle, degrees
ν	kinematic viscosity, m^2/sec tangential force defect thickness, m
ν_t	eddy viscosity, m^2/sec
Π	Cole's function
ρ	air density, $dyne/cm^2$ (lb m/ft.^{2})
σ	blade solidity - C/s

τ	tip clearance, m, shear stress, kg/m^2, radius of torsion of the streamline, m
$\bar{\phi}$	camber angle, degrees
$\bar{\phi}$	flow coefficient - V_x/U_t
ψ	pressure rise coefficient $(P_{o_2} - P_{o_1})/\frac{1}{2} \rho U_t^2$
ψ_E	Euler pressure rise coefficient, $2(V_{x_2}V_{\theta_2} - V_{x_1}V_{\theta_1})/U_t^2$
ψ_s	stagnation pressure rise coefficient for the stage static pressure coefficient
Ω	rotational speed, radians/sec
ω	absolute vorticity, radians/sec

Subscripts

a	atmosphere
b	blade
e	boundary layer edge
h	hub
in	compressor inlet
ℓ	local
m	mean
ms	midspan
n	normalized values
o	stagnation quantities
p	pressure surface
r,θ,x	components along r,θ,x coordinate system
ref	reference
s	suction surface
s,n,b	along s,n,b coordinate system (Fig. 2)
s,n,r	along s,n,r coordinate system

t	tip
x,y,z	along x,y,z coordinate system
x,θ,r	axial, tangential, and radial coordinate system, respectively
1,2,3,4,5	refer to the tubes of five hole probe
1	blade inlet
2	blade exit

Superscripts

—	mass averaged quantities
——	passage averaged quantities
═══	overall quantities
'	relative system
∿	without considering endwall effects

INTRODUCTION

Flow near the endwall region of an axial flow compressor rotor and IGV blade is extremely complicated due to the interaction of strong secondary and tip leakage flows, skewed boundary layers on the annulus walls and the blades, and the scraping vortex. The complex nature of the endwall flow is illustrated in Figure 1. Most of the investigations both theoretical and experimental, carried out so far are confined to a study of one of these flow phenomena in the absence of other effects. In an actual rotor, all these flow phenomena exist and interact. The flow is further complicated due to the influence of rotation and streamline curvature.

The present investigation was undertaken with the following objectives.

1. To review the state-of-the-art of endwall flows in axial flow turbomachinery.

2. To measure the endwall flow in the rotor and the guide vane of an axia flow compressor*. This data is useful for understanding the flow field in the region and eventual development of endwall flow model for the design and analysis of compressors.

3. To calculate momentum integral parameters of the endwall flow in a rotor blade, including the effects of the rotor blade and annulus wall boundary layers, and secondary and tip clearance flows.

4. To calculate the secondary flow field in the endwall region of axial flow compressor rotors, including the effects of viscosity and rotation.

5. To measure the design and the off design performance compressor stage and the rotor blade static pressures.

A comprehensive review of the analytical and experimental investigation of endwall flows in axial flow turbomachines is provided. This is followed by the secondary vorticity analysis, which includes the effect of rotation and the viscosity.

The experimental investigation is carried out using the axial flow compressor facility of the Department of Aerospace Engineering and with the assistance of G. Kane and J. Fetterolf. The description of the facility is given later. The overall design and off-design performance of the compressor stage, measurement of the inlet flow and exit flow from each blade row and the rotor blade static pressures at various axial and radial stations are given*.

Momentum integral equations for the annulus wall boundary flow, which includes the annulus wall boundary layer as well as the three dimensional blade boundary layer (Cole's profile for the streamwise profile and the Mager's profile for the radial component is assumed), is given in Appendix A.

---

* Only the unpublished data is incorporated in this report.

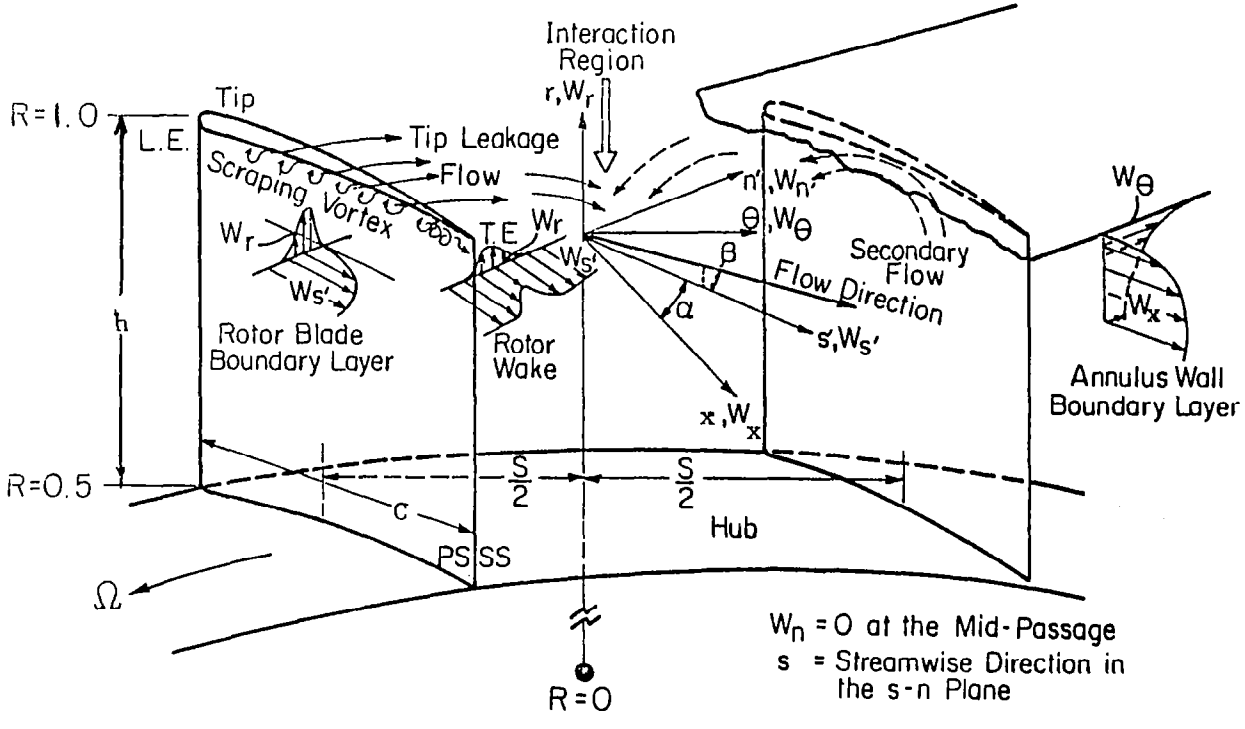

Figure 1. Nature of Rotor Blade Endwall Flows

REVIEW: ENDWALL FLOWS IN AXIAL FLOW TURBOMACHINES

Importance and Need for Study of Endwall Flows in Turbomachines

Flow in the axial flow turbomachinery can be divided into three regions, a free-stream or mid-span region and two end-wall regions, one at the hub and another at the tip. The extent of each of these regions depend on many parameters, such as loading, inlet boundary layer profile, etc. The flow in the free-stream region has been successfully analyzed and predicted by means of two-dimensional cascade theories and correlations based on experimental data. Many of the turbomachines designed on the basis of cascade theories and experimental correlations give good agreement with the flow in the freestream region, but very poor agreement in the end-wall regions. The losses in the free-stream region are usually very small and are caused mainly by the boundary layers developed on the blades, wakes, and the spanwise mixing of the boundary layers and wakes.

The flow in the end wall regions is highly complex, with regions of very high losses. These regions are sources of major inefficiency in turbomachinery. The flow in these regions is strongly three dimensional and turbulence and viscosity play major roles. In addition to the boundary layers on the blades, there are boundary layers on the annulus walls, which are discontinuous due to alternating moving and stationary blade row. The blade boundary layers interact with the annulus wall and hub wall boundary layers to produce a complex turbulent flow. The flow picture is further complicated by the leakage of working fluid through the clearance at the tip of an unshrouded rotor blade row and axial clearance at the tip of a shrouded rotor blade row and the hub of the rotor blade row. These clearances, necessary for preventing physical contact between rotors and stationary annulus, result in unsteady flows, noise and cavitation. The flow, which is already complex, is furthermore complicated in transonic turbomachinery by the interaction with the shock waves. The complexity of the flow is illustrated in Figure 1. The interaction between various phenomena is not shown.

The complex situation at the endwall region modifies the flow from the design conditions. The increased incidence causes the turbomachine blade row to stall in the endwall regions first and the stall margin is reduced, thus effectively reducing the operating range. Any improvement in the stall margin and operating range of a turbomachine should come from the better understanding and improvement of the endwall flow.

At entry to the subsequent row, the picture is further complicated since each blade passage now sees an unsteady inlet flow, which although basically turbulent, contains large scale ordered periodic motions due to local blade passing. The time mean of this endwall inflow has the appearance of a highly skewed layer resulting in a severe variation of incidence into the subsequent blade in the boundary layer.

The complications of endwall flows in an actual rotor has encouraged many researchers to study the endwall flows in cascades, where the various phenomena can be separated and their effect on the cascade performance can be studied. The theoretical work was conducted mainly on cascade endwall flows in view of its simplicity, but the flow in an actual rotor is much different from that of a cascade and cascade results cannot be directly translated into use for the rotor design and the performance prediction. This fact is recognized and attempts to understand and model the rotor endwall flows are being made.

Table I lists many excellent reviews devoted to the endwall flows in axial flow turbomachines. The list is by no means exhaustive and many other excellent reviews are found in other published and unpublished (mainly theses, for example [1,2]) works. The present review concentrates on recent work on endwall flows. The purpose of this review is to provide a source of various works, to delineate the achievements and limitations of present methods and to indicate areas of further research and necessary improvements. Various geometrical and flow parameters on which these phenomena depends, and effects of these phenomena on the performance of the turbomachinery are described by Lakshminarayana [3].

Annulus Wall Boundary Layers

In this section, the investigations specifically directed towards understanding and modelling of annulus wall boundary layers in turbomachines are reviewed. It should be noted that the annulus wall boundary layers interact with other endwall flow phenomena (for example, endwall secondary flows would be present, whenever the annulus wall boundary layers are turned through blade rows), even though some investigators made attempts to study annulus wall boundary layers, by eliminating or minimizing the presence of other endwall flow phenomena. Also the major objective of annulus wall boundary layer investigations is to include its effects in the performance and design analysis of turbomachinery, for which the first step is the calculation of inviscid flow.

Annulus Wall Boundary Layer Calculation Methods

Before describing the application of conventional boundary layer theories to annulus wall and blade boundary layers prediction, the following differences between them should be mentioned.

1. The centrifugal or Coriolis effects present in turbomachines modify the turbulence structure in the boundary layers.

2. The free stream turbulence and unsteadiness that exist in turbomachines change both the basic equations used (momentum integral, entrainment, and shear stress) and the assumed form of the velocity profiles. The velocity profiles (especially cross-flow profile) needs to be modified for the effects of blade surfaces.

TABLE I - LIST OF REVIEWS ON THE ENDWALL FLOWS IN AXIAL FLOW CASCADES AND TURBOMACHINES

S No.	Author and Reference	Phenomenon and Period Covered
1	J. H. Horlock and H. J. Perkins [26]	Theoretical and experimental research on annulus wall boundary layers.
2	J. H. Horlock [194]	Reviews research on the annulus wall and blade boundary layers up to 1970.
3	J. H. Horlock [111]	Reviews research on the secondary flows beyond 1973.
4	J. H. Horlock and B. Lakshminarayana [112]	Reviews work on various types of secondary flows during the period 1963-73.
5	B. Lakshminarayana and J. H. Horlock [113]	Reviews research on secondary and tip clearance flows up to 1963.
6	J. Dunham [131]	Reviews cascade secondary flow losses in turbines with emphasis on loss correlations.
7	Y. Senoo [196]	Secondary flows in centrifugal impeller.
8	S. Otsuka [195]	An extensive review of secondary flows in cascades and axial flow turbomachines.
9	J. P. Johnston [82]	Reviews the effects of rotation on boundary layers in turbomachine rotors.
10	J. Reeder [158]	A bibliography on tip clearance effects.
11	B. Lakshminarayana [3]	This paper classifies the sources of losses, the flow and geometric parameters on which they depend, reviews various available methods for their evaluation.

3. In integral theories, the pitch-wise averaging of momentum equation gives raise to some additional terms. The variation of these terms and blade force in the boundary layer generates additional integrated terms, known as defect forces.

4. Tip clearance affects the growth of annulus wall boundary layer and its effects should be taken into account in the boundary layer calculation.

Various calculation schemes available for the annulus wall boundary layers, especially in bounded region (by blade surfaces) are described below.

The annulus wall boundary layers are quite different from the conventional boundary layers, but many investigators looked upon it as a three-dimensional boundary layer problem and modified the conventional boundary layer calculation methods to predict the annulus wall boundary layer growth. The other group of researchers, mainly interested in predicting cross-flow velocities, treated it largely as an inviscid problem, which could be solved through the equation for the streamwise component of vorticity. It is to this line of research that the expression (endwall) secondary flow theory is usually applied. The relationship between these two approaches has been and remains somewhat ambiguous; in particular, it was not entirely clear whether they were simply alternative ways of looking at the same phenomenon, or whether they in fact had to be combined to give a true picture of physics involved. In the last few years some of this ambiguity has been resolved and secondary flow theories have been successfully utilized in predicting the annulus wall boundary layer growth. In the following sections the previous investigations (both theoretical and experimental) on annulus wall boundary layers are reviewed. However, it should be noted that it is very difficult to separate the interaction between annulus wall boundary layers and other endwall flow phenomena (especially in the experimental investigations of rotating or stationary blade rows).

The secondary flow investigations are reviewed in a later section.

The annulus wall boundary layer represents a particularly formidable problem for a boundary layer calculation scheme since it is three-dimensional, asymmetric and turbulent flow of the strong interaction type, that is, there is no easy separation of the main stream from the boundary layer flow. In addition, it interacts with boundary layers on the blades, secondary flows and clearance flows. Additionally there are centrifugal and Coriolis forces in the case of rotating blade forces. However, recent attempts to assess the growth of annulus wall boundary layers are meeting with some success. All or most all of these methods are based on conventional boundary layer calculation methods. They are all integral methods employing axisymmetric approximations to the flow. The tangential pressure gradients imposed by the presence of blades are taken into account in an approximate fashion, by means of blade force defects. The complexity of the flow and complicated geometry prohibited application of differential methods to annulus wall boundary layer calculation.

Railly and Howard [4] appear to have made one of the first attempts to develop annulus wall boundary layer calculation scheme for turbomachinery. Later their approach was modified and improved to account for the basic differences between the conventional boundary layers and the annulus wall boundary layers. They derived momentum equations for the axial and tangential directions, with the usual boundary layer assumptions, such as constant static pressure and blade forces (which are accounted for by uniformly distributed body forces) across the boundary layer. The wall shear stress expression for the flat-plate based on a one-seventh power law mean velocity profile and cross-flow profile based on the experimental data of Gruschwitz's [5] on an unbounded three-dimensional boundary layer were used along with the mainstream flow calculated using the actuator disc theory. The calculated displacement thickness agree fairly well with experimental values from a three-stage axial flow comparison but the skew angle is not well predicted.

Jansen [6] and Stratford [7] developed simple boundary layer calculation methods for predicting the blockage. Both methods use conventional boundary layer assumptions and "flat plate" expressions for streamwise profiles, wall shear stress and shape factor. Both methods consist essentially of solving only one momentum equation (meridional direction in Jansen's method and axial direction in Stratford's method).

All the above methods suffer from the conventional boundary layer assumptions. Smith [8] questions the assumption of constant blade force through the annulus wall boundary layer. Because of the fall-off in axial velocity in the endwall region, the mean flow direction is closer to the tangential direction and, therefore, the force is more nearly axial. The axial component of blade force does not fall off in the annulus wall boundary layers, but the tangential component does. Because of the tangential component fall-off the shaft work input to the end-wall boundary layers is reduced, and the efficiency loss there is not as large as had been previously believed.

Smith [8], therefore, defines a new boundary layer parameter, the tangential force thickness ν, which is a measure of the tangential force deficit. Neglecting tangential shear stresses on the hub and casing wall and also between adjacent stream surfaces, he defines the tangential force thickness,

$$\nu_h = \frac{1}{r_h F_{\theta_e}} \int_{r_h}^{r_h+\delta_h} (F_{\theta_e} - F_\theta) r dr \qquad (1)$$

and

$$\nu_t = \frac{1}{r_t F_{\theta_e}} \int_{r_t-\delta_t}^{r_t} (F_{\theta_e} - F_\theta) r dr \qquad (2)$$

where F_θ = tangential blade force per unit span (subscript "e" indicates mainstream value)

$$= 2\pi\, r_2\, \rho\, V_{x_2}\, \frac{[r_2 V_{\theta_2} - r_1 V_{\theta_1}]}{(r_1 + r_2)/2}$$

Later investigations confirm the existence of the blade force deficit and included it in the annulus wall boundary layer calculations.

Two main calculation methods have been developed more recently: one due to Mellor and Wood [9] and the other due to Horlock and Hoadley [10]. Since later investigators followed and improved one of these methods, these methods will be described briefly. In both cases the three-dimensional motion equations are averaged across the blade pitch, which resulted in second order terms due to blade-to-blade variation of flow quantities. Mellor and Wood [9] retain these terms, while Horlock and Hoadley [10] neglect them. As usual the mainstream momentum equations are subtracted from the boundary layer momentum equations and the differences are integrated across the boundary layer to obtain momentum integral equations.

Mellor and Wood [9] retain the blade force terms in the difference equations. Their argument is based on Mellor and Strong's [11] observation of "equilibrium" annulus wall boundary layers in multistage compressors. Their existence is directly related to the skewed nature of the annulus wall boundary layer as discussed by Moore and Richardson [12], Taylor [13], and Johnston [14]. On the other hand, von Karman type solution developed by Railly and Howard [4], Jansen [6], and Stratford [7] predicts indefinitely growing boundary layers in multistage compressors. Their momentum integral equations are

$$\frac{d}{dx}\left(\bar{V}_{x_e}\, \theta^*_x\right) + H_x \theta^*_x\, \bar{V}_{x_e}\, \frac{d\, \bar{V}_{x_e}}{dx} = \frac{d}{dx}\left(\frac{\bar{V}_e^2}{2} F_x\right) + \frac{\bar{\tau}_{o_x}}{\rho} \tag{3}$$

$$\frac{d}{dx}\left(\bar{V}_{x_e}\, \bar{V}_{\theta_e}\, \theta^*_\theta\right) + H_x \theta^*_x\, \bar{V}_{x_e}\, \frac{d\, \bar{V}_{\theta_e}}{dx} = \frac{d}{dx}\left(\frac{\bar{V}_e^2}{2} F_\theta\right) + \frac{\bar{\tau}_{o_\theta}}{\rho} \tag{4}$$

where $\bar{V}_e = \bar{V}^2_{x_e} + \bar{V}^2_{\theta_e}$ (pitch averaged mainstream velocities)

$H = \delta^*_x/\theta^*_x$

$\bar{\tau}_o$ = pitch-averaged annulus wall shear stress.

and x, θ are coordinates aligned with the axial and tangential directions respectively.

The integrated blade force defects F_x and F_θ include contributions from the wall shear stress on the blade surface as well as the static pressure variation through the boundary layer. Mellor and Wood further integrated the above equations between inlet and exit of a blade row. Since there are four unknowns, F_x, F_θ, θ^*_x and θ^*_θ at blade exit, four equations are

necessary. The additional two relations are obtained by relating F_x to F_θ on the assumption of constant blade force angle in the boundary layer and relating θ^*_x and θ^*_θ by means of a simple secondary flow analysis. Empirical values for C_f, H_x and K, to account for clearance leakage flow, were used. Mellor and Balsa [15] and Balsa and Mellor [16] used this theory with the simple mainstream calculation scheme of Mellor [17] to predict the overall performance of several different compressors. They used a high value of C_f of 0.010 (about three times that for a flat plate) to account for the adverse pressure gradient. Good agreement could be produced for a particular speed line by adjusting the independent parameters, but other speed lines were not predicted well using the same values. A major feature of this calculation scheme is prediction of stall and surge of the various compressors.

Hirsch [18] reformulated Mellor and Wood's theory in streamline coordinate system and related the shape factor and skin friction coefficient to the boundary layer thickness. He suggested these parameters should also be dependent on the mean flow rate and speed. He also suggested low values of C_f (0.003) where there is no tip leakage and higher values of C_f (0.025) when there is leakage. Later, Hirsch [19] used his method, along with the finite element mainstream calculation method of Hirsch and Warzee [20] and assumed velocity profiles in the boundary layer to predict the flow in axial flow compressors.

This method is later improved by DeRuyck et al. [21, 22] and extended to compressible case by DeRuyck and Hirsch [23]. Their theory was used to develop correlations for force defects and end-wall blockage. DeRuyck and Hirsch's method provides good agreement with the low speed and the high speed (including transonic) compressor overall performance (including prediction of the stall), spanwise velocity profile, annulus wall blockage and defect forces. Their method needs to be extended to the annulus wall boundary layer calculation inside blade passage, similar to the method of Comte, Ohayon and Papailiou [24], who calculate the annulus wall boundary layers inside the compressor cascade passage.

Horlock and Hoadley [10] integrated the pitch-averaged quantities numerically through the blade fow. Cole's velocity profile was used for the streamwise profile and the Mager's expression was used for the cross-flow profile. Final closure was obtained through Head's entrainment function. The result is four simultaneous first-order ordinary differential equations which are integrated numerically to obtain the independent parameters. The boundary layer thickness, δ, Cole's wake amplitude factor, Π, the skin friction coefficient, C_f, and the cross-flow angle at the wall ε_o. The discrepancy between the theory and experimental results was attributed to the neglect of blade force defect terms and use of Mager's cross flow velocity profile, which does not include a cross-over.

Marsh and Horlock [25] included the blade force defect terms on the basis of order-of-magnitude analysis. By assuming that the axial pressure gradient is transmitted to the boundary layer and that the cross flow is small they derived the following expression for tangential force defect:

$$F_{\theta_e} - F_\theta = \rho\left(\overline{V_{x_e}^2} - \overline{V_x^2}\right)\frac{d\theta_e}{dx} \qquad (5)$$

where θ_e = flow turning at the boundary layer edge.

This expression was then used in a modified Horlock and Hoadley method.

Horlock and Perkins [26] summarized the work done at the Cambridge University up to 1973. This work includes various theoretical methods for different cases such as the axisymmetric case, pitch-averaged case, inclusion of blade boundary effects [27] and inclusion of tip clearance effects [1]. The limitations of Mager's and other conventional cross-flow velocity profiles for the case of bounded boundary layers is recognized and a new cross-flow velocity profile based on secondary flow theory is derived [28]. Marsh and Horlock [25] and Daneshyar et al. [29] compared various methods for the annulus wall boundary layer methods. Their major conclusion is that the present through-flow calculation schemes do not provide accurate predictions for the primary flow. They also conclude that the simplest method of Stratford [7] gave the best predictions of axial blockage, axial displacement and momentum thicknesses, even for Gregory-Smith's [30] high deflection guide vanes.

In recent years, secondary flow theories to determine the cross-flow are being widely used. Railly and Sharma [31] and Sockol [32] have been particularly successful in predicting the boundary layer through a single-stage compressor and the highly loaded cascade, respectively.

In the case of turbines, where the variations across the pitch are very large due to strong secondary vorticity, the above type of analysis (pitch averaging) is not suitable. Detailed three-dimensional analyses are necessary. Carrick [33] compared his experimental results in a turbine cascade without and with inlet skew with three methods of calculation.

1. Pitch-averaged boundary layer analysis similar to Lindsay's [1] method.

2. The Stuart and Hetherington [34] analysis (including dissipation).

3. A three-dimensional boundary layer analysis based on developments of work by Dring [35] and Smith [36].

He concluded that the integral type of analysis is valid only for about 30 percent of the chord length in a cascade. The three-dimensional boundary layer analysis gives a fair description of the flow (it is integrated with secondary flow analysis which gives the velocities at the boundary layer). Finally, the detailed calculations of Stuart and Hetherington give a surprisingly good description of the flow, even without allowance for viscosity.

Booth [37] improved Dring's method by including energy equation and obtained aerodynamic losses.

The complete three-dimensional calculation methods of Patankar et al. [38] and Pratrap and Spalding [39] should be mentioned as the most potential methods for the solution of the three-dimensional flow through a cascade, or rotating blade rows, including the endwall region.

Experimental Investigations on Annulus Wall Boundary Layers

The experimental investigations on the annulus wall boundary layers can be divided into the two following groups.

1. Cascades: The experimental data on the cascades consists of earlier investigations of detailed traverse of the exit flow only and recent investigations, which include detailed traverses inside the blade passage.

2. Rotors: The experimental data on the rotors can be classified into two categories: spanwise traverses of flow properties at the rotor inlet and exit. These types of traverses are made for many rotors to determine their performance characteristics. However, some investigators have made careful traverses, sometimes systematically varying annulus wall boundary layer thickness (and other parameters). The other category consists of detailed traverses (i.e., blade-to-blade) of flow at the rotor exit and inside the blade passages.

It should be noted that many of the investigations on cascades and rotors consists of the interaction effects between annulus wall boundary layers and other endwall flow phenomena. Various investigators have measured total pressure losses and swirl angles at the exit of cascades (example: Lakshminarayana [40] in compressor cascades, Turner [41] in turbine cascades and Horlock [42] in a compressor stator). This kind of information should be considered as preliminary, since it would not give insight into the development of boundary layer inside the blade passage. Only recently such investigations on cascades and rotors are undertaken. It should be mentioned that many of these studies are undertaken with a view of understanding endwall secondary flows and reducing them.

One of the earlier investigations worth mentioning is the smoke visualization tests in a plane compressor cascade by Hansen et al. [43]. The cross-flow on the endwall and the roll-up of the boundary layer into a streamwise vortex can be clearly seen. In addition, the vortex was very persistent and could be seen to produce a separation where it "struck" the pressure surface of a downstream blade. Similar flow visualization tests were conducted on turbine nozzle blades and turbine rotors and are summarized in Johnsen and Bullock [44].

The first measurements inside a compressor cascade blade passage were probably taken by Moore and Richardson [12]. Skewed inlet boundary layer was generated with a transverse jet and this was found to reduce the growth of the momentum thickness compared with the case of a collateral inflow. The skewed inlet flow is more representative in the case of a real machine. Blade loading, measured using static pressure taps, was found to

decrease towards the endwall. This seems to indicate that the usual boundary layer assumption of zero pressure gradients normal to the wall does not apply to the annulus wall boundary layers. In a parallel work, Senoo [45] continued work on Turner's [41] apparatus, adding measurements inside the blade passage. His most interesting finding was the boundary layer at the throat and was laminar irrespective of the nature of the inlet boundary layer. Senoo [46] also developed an integral three-dimensional laminar calculation method, which predicted the observed flow fairly well. However, its use is limited, since in real machines, relaminarization is prevented due to the high levels of free-stream turbulence.

Table II lists recent investigations inside cascade blade passages. Most of these investigations consist of velocity and pressure measurements acquired with two-dimensional probes (exceptions are Bario et al. [47], Langston et al. [48], and Marchal and Sieverding [49]) and flow visualization experiments. These experimental data should be useful for the improvement of annulus wall boundary layer calculation methods. The major conclusions to be derived from these experiments are observation of leading edge vortex in the case of turbine cascades, confinement of passage vortex near the suction surface, endwall corner (leading to corner stall) in the compressor cascades. Carrick [33], Klein [50], and Bindon [51] showed secondary vorticity increases with the skewness of the inlet flow.

In the case of rotors, flow traverses are customarily made at the inlet and exit. These traverses normally consist of a single tangential traverses without much concern for the boundary layer region. However, Smith's [8] data consists of a number of equidistant tangential surveys on a multistage axial flow compressor with various types of blading. Mahoney et al. [52], Boxer [53], Fujii et al. [54], and Ikui et al. [55] systematically varied the inlet boundary layer thickness and concluded that the maximum decrease in efficiency is about 2.5 percent when the boundary layers occupy half the blade span. Bois et al. [56] measured the three-dimensional annulus wall boundary layers in a transonic axial flow compressor and obtained good comparison with theoretical prediction of modified Mellor and Wood's [9] method.

A number of studies have been made at Cambridge University, partly in support of the endwall calculation schemes which have been developed there. They only involved flow traverses (i.e., only at a particular tangential location) at the inlet and exit of the rotor and tangential survey at the exit of cascades (with the exception of Daneshyar [27] and Carrick [33]). Details of these experiments are given in Horlock and Perkins [26]. Bitterlich and Rubner [57] made measurements in a single-stage subsonic axial flow compressor mainly to investigate the effects of the boundary layer on the mainstream flow (such as disturbances to the radial equilibrium).

Detailed flow field traverses at the rotor exit and inside the rotor blade passage are necessary for understanding the endwall flows and are being undertaken only recently. The ensemble average technique developed by Lakshminarayana and Poncet [58] was used by Hirsch and Kool [59],

Table II. List of Experimental Investigations of Endwall Flows Inside Cascade Blade Passage

S No.	Author and Reference	Profile	C_{ms}(m)	σ_{ms} (C/s)	h/C_{ms}	ϕ_{ms}	λ_{ms}	τ/C_{ms}	$V1_{ms}$ (m/sec)	β_{1ms}	θ_{ms}	AVR_{ms}	i_{ms}	$\delta^*_{x_1}/h$	$V_b/V1_{ms}$
I.	Plane Compressor Cascades														
1a	Salvage [134]	NACA 65-4A_{10}-10	0.127	0.992	1.008	10°	49.5°	0	31.2	56°	8°	1.056	1.5°	0.026	
1b	Salvage [134]	NACA 65-18A_{10}-10	0.127	0.998	1.002	45°	23°	0	34.6	43.6°	32.2°	1.063	-1.9°	0.018	
2a	Flot [182]	NACA 65-12A_{10}-10	0.130	1.25	2.1	30°	30°	0	44.6	48.3°	27.4°	1.124		0.039	
2b	Flot [182]	NACA 65-12A_{10}-10	0.130	1.25	2.1	30°	30°	0	47.0	56.2°	31.8°	1.210		0.100	
2c	Flot [182]	NACA 65-12A_{10}-10	0.130	1.25	2.1	30°	30°	0.011	46.8	55.5°	30.9°	1.220		0.092	
2d	Flot [182]	NACA 65-12A_{10}-10	0.130	1.25	2.1	30°	30°	0.022	46.1	56.6°	30.7°	1.250		0.133	
2e	Flot [182]	NACA 65-12A_{10}-10	0.130	1.25	2.1	30°	-15°	0	44.9	20.4°	44.2°	1.080		0.014	
3	Bario et al. [47]	Double Circular Arc	0.079	1.645	1.266	30°	35.24°	0	High Sub-sonic	51°	24°		1°	0.0266	
II.	Annular Compressor Cascades														
4a	Daneshyar [27]	British C4	0.152	1.409	3.0	0	0	0	18.6	0	∿0	∿1.0	0	0.0136	
4b	Daneshyar [27]	British C4	0.152	1.409	3.0	0	12°	0	18.6		∿0	∿1.0	12°	0.0136	
5	Kummel [198]	NACA 65 Series	0.070	0.967	1.736			0	63.8						
III.	Plane Turbine Cascades														
6	Langston et al. [48]		0.344	1.281	0.808		35°	0	33.5	44.7°	∿18°		0.7°	0.010	
7a	Carrick [33]		0.152	1.0	3.0			0	25.0	40°	79°		-8°	0.044	0
7b	Carrick [33]		0.152	1.0	3.0			0	25.0	40°	79°		-8°	0.047	0.5
7c	Carrick [33]		0.152	1.0	3.0			0	25.0	40°	79°		-8°	0.057	0.9
8a	Marchal & Sieverding [49]	Nozzle Blade	0.120	1.379	0.833	67.7°	-42.5°	0	34.0	0	67.8°			0.0092	
8b	Marchal & Sieverding [49]	Nozzle Blade	0.120	1.379	0.833	67.7°	-42.5°	0	34.0	0	68.3°			0.0313	
8c	Marchal & Sieverding [49]	Rotor Blade	0.127	1.460	0.787	69.8°	-38.5°	0	34.0	30°	69.6°			0.0162	
9a	Bailey [197]	Turbine IGV	0.272	1.295	0.617			0	28.7	0				Thick	
9b	Bailey [197]	Turbine IGV	0.272	1.295	0.617			0	28.7	0				Thin	
9c	Bailey [197]	Turbine IGV	0.272	1.295	1.866			0	28.7	0				Thin	
10	Bario et al. [47]	Turbine Rotor	0.130	1.307	2.108		-53.3°	0	Low Sub-sonic	48.50°	12.5°			0.0323	
IV.	Annular Turbine Cascades														
11	Sjolandar [2]	T_6 Profile	0.076	1.091	0.667	50°	34°	0	42	0	45°			0.013	
12a	Bindon [51]	T_6 Profile	0.076	1.091	0.667	50°	34°	0	42	0	45°			0.019	1.0
12b	Bindon [51]	T_6 Profile	0.076	1.091	0.667	50°	34°	0	32	0	45°			0.024	2.0

DeRuyck et al. [21] and Davino and Lakshminarayana [60,61]. Dring et al. [62] used rotor mounted pressure probes to measure rotor exit flow in an axial-flow fan at four axial stations and four flow coefficients. In addition, they measured blade static pressure and limiting streamlines. Even though, the flow is nearly two dimensional in the midspan of blade passage, the flow is highly three dimensional at the rotor exit. The complex interaction between the various endwall flow phenomena is illustrated in the above investigations. Recently, investigations inside the rotor blade passage were reported by Sitaram et al. [63] and Davino [64]. The former measured the pressure and velocity fields and the latter measured the velocity and turbulence fields in the blade passage of a moderately loaded axial flow compressor rotor.

Loss Correlations and Methods of Reducing Losses

Most of the loss correlations available are only for the overall losses and they predict the overall decrease in efficiency.

Johnsen and Bullock [44] observed higher losses at the annulus regions and gave different correlation curves as function of diffusion factor and blade heights. Smith's [8] correlation includes the tangential force thicknesses. For high hub/tip radius ratio, their expression for the efficiency including the endwall effects is given by

$$\eta = \tilde{\eta}\,\frac{[1 - (\delta_h^* + \delta_t^*)/h]}{[1 - (\nu_h + \nu_t)/h]}$$

where $\tilde{\eta}$ is efficiency without considering the endwall effects.

Koch and Smith [65] generalized the above equation for various compressors

$$\eta = \frac{\bar{\eta}[1 - (2\bar{\delta}^*/\bar{s})(\overline{s/h})]}{[1 - (2\bar{\nu}/2\bar{\delta}^*)(2\bar{\delta}^*/\bar{s})(\overline{s/h})]} \qquad (6)$$

where overbar "——" represents the average of rotor and stator mean-diameter values. They developed correlations for other losses and obtained good agreement for measured and correlated overall efficiency.

The most versatile loss correlation is due to Hanly [66], who used Coles' [67] velocity profile for collateral inlet boundary layer, and obtained the spanwise variation of losses in a plane compressor cascade as a function of the diffusion parameter, $(p_2 - p_1)/q_1$ and $\delta_{x_1}^*/C$. Some of his assumptions, such as independence of losses on the blade shape, were later questioned, but his correlation agrees quite well with the experimental results. Similar correlation for the rotors and stators would be very useful in the preliminary design of turbomachinery.

It should be noted that the various methods tried to reduce losses in the endwall region mainly reduce the endwall secondary flows. One method, which may reduce the direct losses due to the annulus wall boundary layers is suction of the flow in the corners between the convex

surface of the blades and the annulus walls. Stratford [68] and Peacock [69] have applied this method in high speed and low speed plane compressor cascades, respectively. Peacock found that removing 0.4 to 0.6 percent of the passage flow was sufficient to eliminate corner separation entirely, whereas Stratford required 1.3 percent flow removal to accomplish this. Stratford measured a resulting 40 percent decrease in the total pressure loss. Taking the pumping work, he concluded there is still an overall gain of the order of 25 percent.

Hartmann et al. [70] have tried various methods, including wall suction, suction slit, blowing, blade surface suction, and tandem blades, to reduce the stator end-wall losses. The most successful was the suction slit at the intersection of the blade suction surface and the hub wall (similar to Stratford and Peacock's method). With a suction flow rate of 0.2 percent of the passage flow, an overall stage efficiency improvement of 1.5 percent was observed. They discussed application of similar method to delay tip stall thus increasing the stall margin of the rotor. This consists of 4 percent bleed through the honeycomb casing insert over the rotor blade. A marked improvement in the operating range of the rotor was observed, even without the suction through the treated casing insert. Many experimental investigations, consisting of various casing treatments, were conducted to understand the flow mechanism with casing treatment. Discussion of these investigations is beyond the scope of the present review.

Blade Boundary Layers

Boundary layers developing on the blade surfaces of turbomachinery are turbulent and three dimensional. Most of the previous investigations were conducted on plane cascades and these results can not be transferred to the blade boundary layers in an actual machine since these are affected by Coriolis forces and higher free-stream turbulence. In the case of rotor, additional forces due to rotation affect the cross-flow and the turbulence structure. The interaction between shock waves and blade boundary layers complicate the calculation of boundary layers even in plane transonic cascades. In addition, these boundary layers interact with the annulus wall boundary layer at the hub and tip and produce complex flows. Finally, these boundary layers develop into wakes and produce unsteady flows onto the succeeding blade row resulting in unsteady forces and associated noise. In the following, a review of theoretical and experimental investigations on the blade boundary layers and wakes is given, emphasizing the recent studies in rotors.

Theoretical Investigations

Papailiou [71] gives an excellent summary of the methods used for the calculation of two dimensional boundary layers. The boundary layer on the blade of an actual machine may be part laminar, part transitional and part turbulent. Laminar separation may occur before transition. Seyb [72,73] has undertaken comprehensive calculation of these boundary layers for a two-dimensional compressor cascade. Dunham [74]

compares various methods of calculating the separation length on the compressor cascades. In the case of blade boundary layer, the momentum thickness increases with the increasing axial velocity ratio across the cascade. Dunham [75] compares his calculation method with the measured boundary layer growth on the suction surface of blades.

Momentum integral and approximate differential techniques have been successfully applied to predict the boundary layer growth on rotating helical blades, simplified case of actual turbomachinery. A few examples are laminar boundary layer studies on single helical blades by Fogarty [76] and Horlock and Wordsworth [77]. Banks and Gadd [78] and Lakshminarayana et al. [79] calculated turbulent boundary layer growth on rotating blades of large stagger angle. The latter obtained good comparison of momentum thickness and limiting streamline angle between their theoretical and experimental results. Their method was later extended to cross-channel pressure gradients by Anand and Lakshminarayana [80], who obtained good agreement with the experimental results in four flat bladed inducers. Lakshminarayana and Govindan [81] extended this method to include surface curvature effects, which are important in axial fans and compressors and obtained good agreement with various experimental data.

The effect of rotation on the velocity profile is to modify the Coles' profile as given below

$$\frac{V_s}{V_\tau} = \left[\frac{1}{0.4} - \left(\frac{\gamma \Omega \nu}{V_\tau^2}\right)\left(\frac{yV_\tau}{\nu}\right)\right] \ln\left(\frac{yV_\tau}{\nu}\right) + 5.5 \qquad (7)$$

where "γ" is a dimensionless factor of proportionality, approximately equal to one to account for rotation effect. y is the coordinate normal to the wall. The above equation was first derived by Johnston [82]. Comparison with the data on a centrifugal impeller blade of Litvai and Preszler [83, 84] give good agreement.

All the methods described earlier are direct or analytical methods, i.e., given blade geometry and flow conditions, the boundary layer growth along the blade is calculated. In the inverse or the design method, the cascade geometry is determined to obtain a given velocity distribution (example of which are Staniz's [85] method for two-dimensional incompressible channel flow and Shekar and Norbury's [86] method for two-dimensional compressible cascade flow). In recent years, boundary layer calculating method is used to determine optimum blade shape that gives minimum loss for given inlet and outlet condition. These methods are based on the dissipation-integral method of LeFoll [87]. This method has been successfully used in the design of high-turning incompressible axial flow compressor blade [88], a small incompressible turbine blade [89], compressible cascade [90], and compressible diffuser [91]. All these examples are two-dimensional and this method needs to be extended to three-dimensional flows for use in the design of blades in an actual machine.

The flow in the corner of blade surface and annulus walls is very complex, due to the interaction of boundary layers on the blades and the annulus walls. The simple calculation methods such as that by Perkins [92] who investigated the flow in a corner with zero pressure gradient, may not be valid for an actual rotor. More sophisticated methods are necessary.

Experimental Investigations

Earlier experimental investigations carried out consist of the boundary layer measurements and a study of the effect of various parameters, such as inlet turbulence, Reynolds number, etc., on the boundary layer growth and losses in plane cascades. The reader is referred to Lakshminarayana [3] for details of these investigations. Recent investigations concentrate on the detailed measurements of the boundary layer in high speed plane cascades (turbine cascades by Oldfield, et al. [93], and Sharma et al. [94] and compressor stator blades by Meauze [95]). Transition of the boundary layer on the suction surface was observed in the above cases, which confirms such observations in a stator blade by Walker [96].

The complexities involved in measuring the boundary layer on a rotor blade prompted many investigators to study the boundary layer growth on the rotating channel walls (examples: Moon [97], Moore [98], Halleen and Johnston [99]) and simple turbomachine geometries (examples: Litvai and Preszler's [83,84] low speed radial impellers, a low speed single helical blade of Lakshminarayana et al. [79], and flat plate inducer channel of Gorton and Lakshminarayana [100] and Anand and Lakshminarayana [80]). The last two studies examine the effect of rotation on the turbulent structure of a fully developed boundary layer in a rotating channel of simple geometry. Such experimental investigations on an actual axial turbomachinery blade are very essential and are slowly forthcoming.

For further details on the experimental investigations the reader is referred to Johnston [82]. Many excellent reviews on the wakes of linear and annular cascades and rotors are available (example: Reynolds and Lakshminarayana [101] on rotor wake, and Ravindranath [102] on linear and annular cascade wakes).

Loss Correlations and Methods of Reducing Losses

Most of the loss correlations available are for the plane cascades only. Lieblein's [103] correlation is based on the turbulent boundary layer theory and correlates the momentum thickness, hence loss coefficient, with the diffusion factor for plane compressor cascades.

Similar correlations are reported for turbine cascades by Stewart et al. [104] and compressor cascades by Schlichting [105]. Papailiou [106] improved Lieblein's correlation and obtained the following relation between blade exit momentum thickness and the equivalent diffusion factor

$$(\theta^*/C)_2 = K\, D_{eq}^3 \tag{8}$$

Koch and Smith [65] extend this correlation for the compressible case basing on the compressible turbulent boundary layer method of Herring and Mellor [107]. They used their correlation in the prediction of overall efficiency of compressors.

All the above correlations are two-dimensional, while the boundary layers in actual machine are three-dimensional in nature with increased mixing and losses due to centrifugal forces. These effects need to be included in the loss correlations.

The losses due to the blade boundary layers constitute only a small percentage of the total losses in an actual machine. Hence, little effort is spent in reducing them. However, tandem cascades and slotted cascades are investigated and found to decrease the overall losses in the rotors. (Example: Slotted rotor blades were used by Sheets [108] in a single stage blower and by Sheets and Brancourt [109] in a multistage axial pump.) Additional theoretical and experimental studies of the viscous flow through such tandem and slotted blade rows are needed. The slotted and tandem blades seem to reduce the corner stall and, hence, improve the stalling performance of turbomachinery.

Secondary Flows

The term "secondary flows" in the turbomachinery has often been used to differentiate between the real flow and primary flow, i.e. either the axisymmetric or inviscid three-dimensional flow, thus including tip leakage flow, scrapping vortex and other real fluid effects. In this section, only the following types of secondary flows are discussed. They are,

1. "Endwall secondary flows," due to the turning of the annulus or the hub wall boundary layer through the cascade.

2. "Corner stall" at the corner of the annulus or the hub wall and the blade suction surface. This is due to interaction of the secondary flows with the boundary layer on the blade.

3. A "horse shoe vortex," observed first by Armstrong [110] to loop around the leading edge close to its junction with the wall and extend downstream. Its motion is such that the secondary flows may be enhanced near the pressure side and diminish near suction surface, but the effect is apparently dependent upon incidence.

4. "Mainstream secondary flows" arising due to the trailing vortices caused by radial variation in circulation. The radial variation in circulation in turbomachinery may be due to the radial variation of pressure, density (in case of subsonic turbomachinery) and temperature (in case of turbines). The direction of the trailing vortices is opposite to that of the endwall secondary flow vortex.

Endwall secondary flows, corner stall and horse shoe vortex could be attributed primarily to the existence of the annulus or hub wall boundary layers. As such, many of the experimental investigations on the annulus or hub wall boundary layers contribute to the understanding of these secondary flows. Also endwall secondary flow theories have been recently used in the annulus wall boundary layer calculation methods. There are excellent reviews on this topic (Horlock [111], Horlock and Lakshminarayana [112], and Lakshminarayana and Horlock [113]). Only the recent advances are reviewed in this section.

Theoretical Investigations

In many of the earlier theories, the secondary flow was predicted using the inviscid vorticity equations. Viscosity only needs to be invoked as the agent producing the non-uniform velocity profile of the incoming annulus wall boundary layers and no account of the boundary layer growth is considered in the calculation of secondary vorticity. These equations are not reproduced here, but the reader is referred to the reviews by Lakshminarayana and Horlock [113], Horlock and Lakshminarayana [112], and Horlock [111].

Lakshminarayana and Horlock [114] have derived the most comprehensive secondary vorticity equations for compressible, stratified and viscous flow both in stationary and rotating coordinate systems. These equations have been used by many investigators to calculate the secondary vorticity due to various effects. Billet [115] has calculated the secondary flow in a rotor with non-uniform inlet flow. Lakshminarayana [116] investigated the secondary vorticity development due to the radial temperature gradients and concludes that with the temperature gradients typically found in turbines the secondary vortices due to the temperature and velocity gradients are of the same order or magnitude. Furthermore, with the usual temperature and velocity profiles (both having maxima near the midspan) the secondary vorticities developed have opposite signs and therefore tend to cancel each other. Physically, the denser fluid near the endwalls tends to be centrifuged towards the outside of the bend while the cross-channel pressure gradient tends to drive it towards the inside. Lakshminarayana's results clearly show that the effects of the radial temperature gradients can not be neglected in the turbine blade rows and perhaps not even some highly-loaded compressors stages with large temperature gradients.

In recent years, the secondary flow theories have been extensively used in the calculation of flow, especially the annulus wall boundary layers in one, two or three blade rows of turbomachines. A few examples are Horlock [42] on a stationary row of twisted guide vanes, Billet [115], Gregory-Smith [30] on isolated rotors, Lakshminarayana [117] on an axial flow inducer rotor, Dixon [118] on an entire compressor stage, DeRuyck et al. [21] on a high speed isolated rotor, Kawai and Adachi [119] on a stator row with various hub/tip ratios and Adachi et al. [120] on a rotor row with various hub/tip ratios. The last three investigations are concerned with detailed traverses (i.e., blade-to-blade) at the blade row exit whereas the former investigations give only pitch averaged

comparison. In all these investigations the agreement between the theory and the experiment is only qualitative, even when the tip clearance effects are taken into calculation [121]. This clearly demonstrates the necessity of including the viscous effects in the calculation of the endwall secondary flow, even though inviscid theory proved valuable in the preliminary estimation of secondary vorticity in high aspect ratio and small cambered blades.

The complexity of flow between the annulus wall and blade surface, resulting in corner stall, precludes any but simplest corner flow analysis (example: Gessner [122], Renken [123], Perkins [92], and Gersten [124]). These models are too idealistic for its application to a real machine, where the flow is highly three dimensional and the rotation substantially alters the flow. In the case of a rotor, the corner separation near the hub is less severe compared to a stationary hub since the blade boundary layer is thrown outwards.

Theoretical investigations suggest that the effects of mainstream secondary flows due to the spanwise variation of lift are small. But in modern turbomachines the spanwise variation of lift is very large and the mainstream secondary flow effects may be large. Recent attempts by McCune and Hawthorne [125] and Tan [126] take these effects into consideration.

In recent years major advances have been made in the numerical calculation of three-dimensional flows. The inviscid three-dimensional calculation methods of Stuart and Hetherington [34] to the calculation of the turbine endwall flow by Carrick [33] is already mentioned. For good agreement between calculation and endwall flow in the cascades and rotors, viscosity must be taken into consideration. The methods of Dodge [127], Ghia et al. [128], and Ghia and Sokhey [129] are valid only for cases with small secondary flows. For turbomachinery, where secondary flows are large, Briley and McDonald [130] coupled the classical secondary flow theory and the "extended" boundary layer theory to obtain good comparison with the experimental data of Langston et al. [48], including the development of corner vortices. In all the above approaches, laminar flow is assumed. But in actual turbomachines, the flow near the endwalls is almost always turbulent. Hence, approaches to account for turbulence effects are needed.

Experimental Investigations

The earlier investigations on secondary flows were confined to the exit traverses of pressures and two-dimensional velocity fields in linear and annular cascades. The reader is referred to Lakshminarayana and Horlock [113], Horlock and Lakshminarayana [112], and Dunham [131] for details of these investigations. Only recently, the three-dimensional flow inside cascades and rotors are being measured. Details of these investigations on cascades are given in Table II and on rotors in Table III.

The earlier investigations of cascade exit traverses by Gersten [132], Scholz [133], and Lakshminarayana [40] are worth mentioning. These investigators systematically studied the effect of the incoming boundary layer thickness on secondary flows (and also tip clearance flows) at various solidities, stagger angle and blade incidences. These investigations include both the turbine and the compressor cascades and the major conclusion was that the secondary flow losses in compressor cascades were much larger than those in turbine cascades.

Recently, Salvage [134] has done a comprehensive measurement of secondary flow (and also annulus wall boundary layers) in a cascade with NACA 65-series A_{10} camber line blades. He varied solidity, blade camber angle (i.e., loading) blade incidence, blade stagger angle, and inlet boundary layer thickness. His measurements include the inlet and the exit flow traverses including a good definition of the annulus wall boundary layers, surface flow visualization, and the measurements of blade static pressures. He also measured detailed flow inside cascades of camber angle of 10° and 45° (see Table II). His major conclusions are as follows:

1. The passage vortex primarily controls the spanwise distribution of the outlet flow angle. Cascade inviscid secondary flow theories may be used to determine the distribution of the exit flow angle in cascades.

2. The mass averaged total pressure loss is independent of the inlet annulus wall boundary layer thickness. This loss coefficient is predicted well by Stewart et al [104], who relates the total loss to the profile loss via the ratio of the total wetted passage area to the wetted blade surface area.

3. The conditions that are presently termed as "low aspect ratio" effects (severe disturbance of mid-span flow by secondary flows) are shown to be dependent on the ratio of inlet boundary layer thickness to the blade height and on the turning of the cascade, rather than the aspect ratio of the blade. He proposed the following criterion for the appearance of low aspect ratio effects:

$$\frac{\delta_1}{h} \geq 0.5(1 - \theta C/h) \quad , \quad \theta \text{ is turning angle in radians}$$

The passage vortex is the mechanism which creates effectively a low aspect ratio condition by redistributing low energy boundary layer fluid.

Salvage's work is followed by other investigations of blade passage flow in compressor and turbine cascades (see Table II). These experimental investigations help to understand the secondary flows in cascades and to model these flows. A few experimental investigations conducted with a skewed inlet flow in linear and annular cascades, to simulate the actual flow in a turbomachine rotor, shows that the secondary flow is enhanced with skewness of the inlet flow.

In recent years, various investigators have undertaken studies to improve secondary flows in turbine cascades. Their investigations consist of exit flow traverses in cascades with endwall cooling and endwall contouring. The details of these investigations are given in the next section.

Noise generated due to secondary flow is of considerable importance and is studied by Moiseev et al. [135] and Trunzo [136] who varied the inlet boundary layer thickness. These investigations indicate increasing noise with increasing boundary layer thickness and amplification of noise when these boundary layers are turned by the blades.

Modern turbomachinery operate in a distorted inlet flow. The distortions may be circumferential or radial. The pressure, temperature, or velocity of the inlet flow may be distorted. A study of effects of the non-uniform flow on stationary annular cascade is investigated by Huard [137]. The major conclusion from this study is that the secondary flows are strongly amplified by the initial distortions. Further investigations are necessary in this area.

Rotation and coriolis forces modify the secondary flow structure in a rotor considerably from that of a cascade. Hence, secondary flow measurement in rotor is necessary. Fujie [138] is probably the first investigator to make such an attempt. He measured losses at the rotor exit with a rotor mounted Kiel probe at three flow coefficients. Based on these measurements he proposed the drag coefficient for various phenomena, blade boundary layers, secondary flows, annulus wall boundary layers, and tip clearance. These correlations depend on very few flow parameters and can not be applied to other rotors.

The other investigations of rotor exit flow are carried out by DeRuyck et al. [21, 22], Dring et al. [62], Thompkins and Kerrebrock [139] in a transonic compressor rotor, Davino and Lakshminarayana [60, 61] and Adachi et al. [120]. These investigations are tabulated in Table III. These investigations show the differences between the secondary flows in cascades and rotors.

The experimental data in a complete stage (Gallus and Kummel [140] in a subsonic compressor, and Barry [141] in a turbine) indicate that the secondary flow in a compressor is found to be reduced substantially, whereas in a turbine, the effects are amplified through the blade row.

Loss Correlations and Methods of Loss Reduction

All the loss correlations, available so far, give the overall loss coefficient, rather than the spanwise distribution of the secondary flow losses. Dunham [131], from a review of previous correlations, presented the following correlation for turbine cascades.

$$Y_S = \frac{C}{h}\left(\frac{\cos\beta_2}{\cos\beta_1^*}\right)\left(\frac{C_\ell}{s/C}\right)^2 \frac{\cos^2\beta_2}{\cos^3\beta_m}\,(0.0055 + 0.078\,\sqrt{\delta_1/C}) \qquad (9)$$

TABLE III. List of Experimental Investigations of Endwall Flows at the Exit and Inside of Blade Passage of Rotors

S No.	Author & Reference	Profile	C_{ms} (m)	r_t (m)	h/C_{ms}	ϕ_{ms} Degrees	λ_{ms} Degrees	τ/C_{ms}	$V_{x_1}{}_{ms}$ (m/sec)	$\delta^*_{x_{h_1}}/C_{ms}$	$\delta^*_{x_{t_1}}/C_{ms}$	Remarks
I.	Rotor Exit Only											
1	Fujii [138]	(No data is available)										
2	DeRuyck et al. [21]	NACA 65(A_{10})06	0.080				35°					
3a	Dring et al. [62]	NACA 65 Series	0.1524	0.762	1.0	48°	54.5°	0.01	23.8	0.088	0.0145	P_o, P_s, and three components of velocity are measured
3b	Dring et al. [62]	NACA 65 Series	0.1524	0.762	1.0	48°	54.5°	varies along	27.5	0.088	0.0145	
3c	Dring et al. [62]	NACA 65 Series	0.1524	0.762	1.0	48°	54.5°	chord (0.023	31.1	0.088	0.0145	
3d	Dring et al. [62]	NACA 65 Series	0.1524	0.762	1.0	48°	54.5°	to 0.038)	34.8	0.088	0.0145	
4	Thompkins & Kerrebrock [139]		0.030	0.350	2	90°	45°					Transonic compressor
5	Davino & Lakshminarayana [60, 61]	NACA 65 Series	0.135	0.464	1.72	C_{l_o}=1.5	32°	∿0.018	29.3		0.045	Velocity & turbulence are measured
6a	Adachi et al. [120]	NACA 65 Series	0.120	0.500	0.833					0.017	0.017	
6b	Adachi et al. [120]	NACA 65 Series	0.120	0.500	0.521					0.017	0.017	
6c	Adachi et al. [120]	NACA 65 Series	0.120	0.500	0.208					0.017	0.017	
II.	Rotor Blade Passage											
7a	Ufer [173]	Ventilator Fan	0.080	0.206	0.925	51°	75°	0	20.8			
7b	Ufer [173]	Ventilator Fan	0.080	0.206	0.925	51°	75°	and	16.7			
7c	Ufer [173]	Ventilator Fan	0.080	0.206	0.925	51°	75°	0.0125	12.2			
8	Sitaram et al. [63]	NACA 65 Series	0.135	0.464	1.72	C_{l_o}=1.5	32°	∿0.018	29.3		0.045	Pressure & velocity
9	Davino [64]	NACA 65 Series	0.135	0.464	1.73	C_{l_o}=1.5	32°	∿0.018	29.3		0.045	Velocity & turbulence

Came [142] has revised Dunham's correlation as a result of further measurements on the effect of the inlet boundary layer thickness. His correlation, which includes inlet and exit boundary layer losses, is

$$Y_{SG} = \left(\frac{C_\ell}{s/C}\right)^2 \frac{\cos^2\beta_2}{\cos^3\beta_m} \left(\frac{\cos\beta_2}{\cos\beta_1^*}\right) \left(0.25\, Y_1^* + 0.009\, \frac{C}{h}\right) \qquad (10)$$

where Y_1^* = mass averaged inlet boundary layer loss coefficient relative to the inlet dynamic pressure.

Hence, $Y_S = Y_{SG} - Y_1$ = loss coefficient based on dynamic pressure

where Y_1 = inlet boundary layer loss coefficient relative to the exit dynamic pressure

Came's correlation is further improved by Morris and Hoare [143], whose correlation is

$$Y_{SG} = \frac{C}{h} \left(\frac{C_\ell}{s/C}\right)^2 \frac{\cos^2\beta_2}{\cos^3\beta_m} \frac{\cos\beta_2}{\cos\beta_1^*} \left[0.294(\delta_1^*/C) + 0.011\right] \qquad (11)$$

Salvage [134] reviews similar correlations for compressor cascades. Papailiou [106] correlated the momentum thickness of the annulus wall boundary layers in cascades, compressors and turbines and provided the following correlation,

$$\left(\frac{\theta_2^*}{\theta_1^*}\right) = \left(\frac{V_1}{V_2}\right)^3 [1 + B]^{5/6} \frac{V_{x_1}}{V_{x_2}} \qquad (12)$$

where

$$B = \left(\frac{C_f}{2\theta_1^*/C}\right)^{6/5} \frac{(V_1/V_2)^{4.4} - 1}{4.4(V_1/V_2)^{3.4}[(V_1/V_2)-1]}$$

Lakshminarayana and Horlock [144] measured the spanwise distribution of the secondary flow losses in a compressor cascade with and without clearance. They observed that the secondary flows decrease in the presence of a clearance.

The correlations mentioned above are based on the measurement in plane cascades and caution is necessary in applying them to rotors since many aspects of flow have not been completely simulated.

Since the endwall secondary flows are a direct result of the annulus wall boundary layers, methods of reducing the annulus wall boundary layers, through suction, fences and grooves on the blade suction surface near the walls have been partially successful. Recent experimental investigations by Gustafson [145] in low speed compressor cascade and

Meauze [146] in subsonic, transonic and supersonic compressor cascades indicate the advantages of applying suction at the corner formed by the blade suction surface and the walls.

In addition to applying boundary layer suction, fences and grooves and various other methods of loss reduction have been tried. Horlock et al. [147] proposed decreasing camber in the endwall region and letting the cross-flow complete the turning. They observed that total pressure loss changed little but the wall stall was delayed in a compressor cascade. Schlegel et al. [148] have tested a small low-aspect-ratio transonic turbine, using decreased flow turning near the endwalls of both the stator and rotor blade rows, and showed improvements in stage efficiency of 1 percent at most pressure ratios over the results obtained from the corresponding conventional baseline turbine. Measurements of outlet angle from the stator row showed reduced cross flows. Taylor et al. [149] and Senoo et al. [150] increased the blade chord near the endwalls and obtained smaller losses in such blades in cascades and rotors.

Other methods that have been tried are endwall contouring and endwall cooling. These methods are very successful in case of turbines. Endwall contouring investigations are reported by Deich and Zaryankin [151], Morris and Hoare [143], Kopper et al. [152], in plane turbine cascades, by Due et al. [153] in transonic turbine nozzles, and Ewen et al. [154] in transonic turbine rotors. Morris and Hoare's [143] reports on overall reduction of secondary losses of 25 percent at a low aspect ratio of 0.5. Their conclusion, that the reduction in losses occurs almost exclusively near unprofiled endwall is surprising and may be attributed to changes in the blade pressure distributions due to profiling. Both Due et al. [153] and Ewen et al. [154] reports an average increase of 2.0 percent in overall efficiency in turbines. Endwall cooling investigations, reported by Goldman and McLallin [155] in a turbine stator cascade and Sieverding and Wilputte [156] in a high subsonic plane turbine nozzle cascade, show considerable decrease in losses.

Careful control of endwall contour parameters (i.e., the ratio of change in blade height to the blade axial chord and the location of contours) and endwall cooling parameters (i.e., the coolant to mainstream total pressure ratio, the coolant to mainstream mass flow ratio, angles between coolant flow, main flow and endwall boundary layer and location) improve the performance of small aspect ratio turbines by reducing the secondary flows.

Tip Clearance Flows

Clearances between the rotating and stationary parts in turbomachinery are necessary to avoid mechanical contact and failure. In this section, we are concerned only with the rotor tip clearance, the losses associated with which are quite substantial and are unavoidable. In addition to complicating the flow near the endwall, tip clearance has two major effects:

1. Direct flow through the clearance space which is undeflected and is therefore not available for doing work. Its magnitude depends directly on the thickness and profile of the annulus wall boundary layer and the clearance height.

2. Indirect flow due to the pressure difference between the suction and pressure surfaces.

A recent survey report by Peacock [157] and earlier papers by Lakshminarayana and Horlock [40] and Reeder [158] provide a review of various analytical techniques, experimental data, and the correlations available.

Theoretical Investigations

Earlier investigations were mainly concerned with direct losses only. These are summarized by Jefferson [159]. Recent theoretical investigations can be classified into the following groups:

1. Jet theory, i.e., the leakage flow results from the pressure difference over the rotor and occurs in an annulus of height equal to the clearance height.

2. Theories based on lifting line and lifting surface approaches.

3. Other theories, for example, Wu and Wu's [160] three-dimensional boundary layer approach to determine pressure and velocity distribution in the clearance height. This enables the determination of the direct leakage mass flow.

Rains [161] assumed that the flow in the clearance consists of a jet with uniform velocity across its height with variation in velocity along the chord. Using this assumption, he calculated losses for various values of tip clearances and found satisfactory comparison with the results of actual efficiency measurements on a pump. His model ignores the viscous effects of a real fluid, which are important in the small clearances encountered in actual machines, and the relative motion between the moving blade and the stationary wall. In spite of these limitations, his model is employed by later investigators, especially to predict efficiency loss due to tip clearance.

Realistic models of tip clearance flow can be made using the lifting line or surface theories. Betz [162] first made such an attempt to evaluate the losses from the shed vortices due to the gradient in circulation distribution by applying lifting line theory to a simplified two-dimensional rectilinear cascade. Later investigators modified his theory. Lewis and Yeung [163] classified tip vortex models into the following categories:

1. Vortex Lattice Method (VLM) (Betz [162], Lakshminarayana [40]): In this method the aerofoil is replaced by means of horse shoe vortices at discretized sections. No special consideration is given to the tip vortex development. The tip horse shoe vortex is assumed to lie along the chord.

2. Tip Vortex Method (TVM) (Lakshminarayana and Horlock [144]): To model the rolling up of tip vortices is a very complex procedure involving the adoption of a time marching approach. So TVM improves VLM by adding a simplifying assumption for tip vortex. In addition to the horse shoe vortices from the airfoil, an additional vortex is assumed to be shed from tip. This tip vortex is at an angle to the plane containing horse shoe vortices.

3. Concentrated Tip Vortex Method (CTVM) (Lakshminarayana [121]): In this method, the vortex sheet shed from the tip is assumed to roll up fairly rapidly into a concentrated tip vortex, whose strength develops cumulatively due to the feeding process. The feeding vortices leave the trailing edge of the tip at an angle to airfoil plane but it is now possible to model the rolling up process.

Lewis and Yeung compared VLM and TVM with experimental results of airfoils and established the TVM as the superior model for airfoils of widely varying aspect ratios and for predicting the overall lift coefficient, with good promise for prediction of the spanwise variation. For application to turbomachinery rotors, this theory has to be modified for the effects of neighboring blades, rotation, spanwise variation of circulation, etc.

Lakshminarayana and Horlock [144] modified the VLM method to predict losses in a rectilinear cascade. They assumed only a part of the bound vortex is shed off at the tip. The fraction of retained lift, K is a function of various factors such as tip clearance/chord ratio, solidity, etc. Experimentally determined values of K are used to determine the induced velocity and the drag due to tip clearance (by placing two rows of infinite vortices of strength (1 - K) at twice the clearance height). Lakshminarayana [121] used this model to derive a correlation for loss in efficiency due to clearance. His correlation, which allows for spanwise velocity inside the blade boundary layer at the tip, agrees well with the measured values. He also developed the CTVM by allowing for the viscous core in a tip vortex surrounded by a potential or "free vortex". This model accurately predicts the spanwise variation of losses including the peak losses away from the blade tip. He also combined contributions due to other endwall phenomena and obtained good comparisons with experimental velocities of Croner and Yeh [164].

Bollay [165] and later Sugiyama [166] used VLM to obtain good agreement for induced velocity and drag in low aspect ratio wings with clearance.

In recent years, annulus wall boundary layer calculation methods are extended to include tip clearance effects. One such attempt by Lindsay [1] consists of including the additional defect forces in the annulus wall boundary layer integral equations. His method does not include the indirect effects. This method as well as that developed by Comte et al. [24] may not be valid for rotors.

Experimental Investigations

In order to understand the flow in the tip clearance region and its interaction with other endwall phenomena, actual measurements inside and around the tip clearance in an actual rotor are necessary. In addition, these measurements help to model tip clearance and endwall flows. The complexity of the geometry in this region precluded any but recent investigators to undertake such measurements. Previous investigators measured tip clearance flows in airfoils, linear and annular cascades. Their measurements consist of measuring flow properties inside and around tip clearance, blade static pressures, and visualization of flow inside the clearance. The few investigations on rotors consist of measuring flow properties outside the rotors.

Perhaps the most exhaustive experimental work on linear cascade is due to Lakshminarayana and Horlock [144]. They varied the tip clearance with and without the presence of secondary flows. In compressor cascades, leakage flow is opposite to secondary flow and this helps to prevent the wall stall. Gregory-Smith [30] did not observe such phenomena in an isolated rotor. Lewis and Yeung [163] used all the available data on wings and cascades to obtain a correlation for the retained circulation due to tip clearance.

$$K = e^{-14\tau/C} \tag{13}$$

where K is the ratio of circulation at the tip/circulation of a two-dimensional airfoil of the same section as the tip. Annulus wall boundary layer thickness seems to have had minimal effect upon this correlation. The validity of this correlation for τ/C greater than 0.05 make it useful only for fan rotors, where the clearances are usually large and rotors with very small chords. The rotation effects may invalidate this correlation. The experimental data of Dean [167], who examined the effect of a moving wall on the tip clearance flow in a linear compressor cascade, did not compare well with this correlation. Additional factors such as the annulus wall boundary layer thickness and the speed of rotor are to be included in the above correlation for application to the rotors.

The effect of clearance shape on the tip clearance flows is examined by many investigators (example: Gearhart [168], Hubert [169], Novoderezhkin et al. [170], on compressor cascades and Hurlimann [171] on airfoils). A convergent clearance shape is most effective in reducing clearance cavitation, while a divergent clearance shape is most effective in reducing tip vortex cavitation. A rounded inlet corner reduces the separation and the resulting clearance cavitation. Such tests in actual rotors are lacking.

Experimental investigations of varying tip clearances were conducted by Williams [172] on a low speed axial flow compressor, by Ufer [173], Ryan and Ohashi [174], Croner and Yeh [164], and Thinh [175] on low speed axial fans, Fabri and Reboux [176] on a low aspect ratio supersonic axial

flow rotor, Jefferson and Turner [177] on a multistage axial compressor, Traupel [178] on a multistage turbine, Stobbe [179] on a single and multistage turbine, Rogo [180] on low and high aspect ratio transonic axial turbines, Ewen et al. [154] on low aspect ratio subsonic and transonic axial turbines, and Haas and Kofskey [181] on a low aspect ratio transonic axial turbine. These investigations conclude decisively the adverse effects of large clearances. Also the flow is affected well beyond the clearance region.

Measurements inside blade passage are necessary for better understanding and modelling of tip clearance flows. Such measurements are few (examples: Flot [182] on a linear compressor cascade, Ufer [173] on a low speed axial fan, Sitaram et al. [63] and Davino [64] on a low speed axial flow compressor). Ufer varied the tip clearance from zero to 1 mm. His measurements conclude the necessity of clearance to avoid separation at the tip. The only measurement available in the gap region of a rotor is due to Pandya and Lakshminarayana [183].

A certain amount of clearance is beneficial in compressors. At small clearances, the leakage flow is strong enough to "wash away" the separation zone in the corner between the wall and the blade suction surface and reduce the opposing radial outward flows inside the blade suction surface boundary layers. Such optimum clearance is experimentally observed by Lakshminarayana and Horlock [144], Dean [167], and Hubert [169] in linear compressor cascades, Ufer [173] in a single stage fan and Jefferson and Turner [177] in a multistage axial compressor. Such clearance is not observed in turbines where the annulus wall boundary layers are usually thin. Ewen et al. [154] and Traupel [178] measured increasing efficiency with decreasing tip clearances, up to very small values in both a single stage and a multistage turbine.

Loss Correlations and Methods of Loss Reduction

The various loss correlations available are only for the overall losses, rather than spanwise variation of losses. The earlier correlations are very simple and consider only a few of the major parameters affecting the tip clearance flow.

Hesselgreaves [184] improved Rains [161] and Vavra's [185] correlations. His correlation for tip leakage energy loss in an axial fan is

$$\Delta E = \frac{2\sqrt{2}}{5} \tau \, C \, N_B \, \rho \, W^3 \, C_\ell^{3/2} \qquad (14)$$

Lewis and Yeung [163] improved this method to a suitable form for application to fan performance prediction. Their correlation is

$$\Delta\bar{E} = \frac{8}{5}\,\pi\,\frac{C}{r_t}\,\frac{\tau}{C}\,\frac{C}{s}\,\frac{\psi^{3/2}}{\phi^3}\left\{\phi^2 + \left(1 - \frac{\psi}{2}\right)^2\right\}^{3/4} \qquad (15)$$

where ψ and ϕ correspond to the values at the tip.

Smith [186] observed 4.6 percent drop in the peak pressure rise for each 1 percent increase in τ/C_t. McNair [187] developed various correlations for the drop in stalling pressure rise coefficient due to the clearance with respect to aspect ratio, flow coefficient, and other parameters.

The most recent and widely used correlation is due to Lakshminarayana [121], who provided a semi-empirical relationship for the decrease in efficiency, given by

$$\Delta\eta = \frac{0.7\,\tau\psi}{h\cos\beta_m}\left[1 + 10\sqrt{\frac{\phi}{\psi}\,\frac{\tau}{h}\,A\cos\beta_m}\right] \qquad (16)$$

Many of the industrial firms have reported good agreement between this expression and the data from the turbine and compressor stages.

Various methods have been tried to reduce tip clearance losses. The earlier methods consist of eliminating the clearance entirely. This is achieved by means of shrouding of the blades. This method is not effective, since the radial (tip) clearance is replaced by axial clearance, which generates losses. In addition, a small clearance is necessary for compressors to prevent corner stall and to reduce the secondary flow. In turbines, such effects are not observed, hence minimum practical clearance should be maintained.

Beitler et al. [188] maintained very small clearances in a modern high speed jet engine. These small clearances are controlled by cooling the casing of the engine. The amount of cooling varies with the operating conditions and actively controlled by a computer. They estimate substantial improvements in the efficiency of the high pressure compressor and low and high pressure turbines (the casing over these components is cooled) and consequent yearly savings of 88,000 gallons of fuel per aircraft. Recent investigations by Booth et al. [189] on a turbine and a cascade and Patel [190] on a high work turbine indicate improved efficiency with partially shrouded blades.

Scraping Vortex

The "scraping" of the annulus wall boundary layer by the rotating blade and the presence of "scraping vortices" is observed by many investigators. Flow visualization tests of Hansen et al. [43] in compressor and turbine cascades with wall motion at various operating conditions, Kofskey and Allen [191] in a low speed turbine, and Watanabe et al. [192] in a stationary annular cascade in a transparent rotating casing indicate the nature of these scraping vortices. Apart from this observation of the scraping vortex, very little information is available on the nature and analysis of this phenomena.

Concluding Remarks and Suggestions for Future Research

An exhaustive review of endwall flows in the axial turbomachinery is presented. Various endwall flow phenomena are identified. The review concentrates on the endwall flow investigations on axial compressor cascades and rotors, with relevant information drawn from the investigations of simple geometries and other types of turbomachinery. The following conclusions are drawn and the course of action for further research suggested.

1. Cascade model has proved to be very useful for the endwall flow investigations, but its usefulness is limited due to the fact that the flow in an actual rotor is much different from the flow in a cascade. Hence, there is a need for investigations in an actual rotor. In the case of experimental investigations, the future research may take two directions: Three-dimensional rotor exit flow traverses in the endwall region with the major flow and geometric parameters (such as the inlet boundary layer thickness, tip clearance, etc.) varied systematically. The traverses may be in one circumferential position or in multiple positions and averaged. This data would be very useful for the comparison with the existing annulus wall boundary layer calculation schemes. The other direction, the experimental investigations should take is the detailed flow field investigations inside the rotor blade passage and in the rotor exit. Lakshminarayana [193] reviews various methods available for this type of investigation. These investigations help in understanding the endwall flow, the interaction of various phenomena, and modelling of the endwall flow.

2. The existing annulus wall boundary layer calculation methods are of integral type, with the mainstream flow calculations based axisymmetric calculations. The asymmetry of the flow and variation of blade force and static pressure through the boundary layer results in additional terms. For streamwise profiles, Coles' [67] profile (and other profiles used in unbounded boundary layer calculation methods) proved quite suitable. For the cross-flow velocity profiles, the usual profiles, used in the unbounded boundary layer calculation methods, are found to be unsuitable for the case of rotating and stationary blade passages. Cross flow profiles, developed from the secondary flow theories are found suitable in the calculation of boundary layers bounded by the blade surfaces. The rotor exit flow traverse data mentioned above may be used to refine the existing calculation methods and elimination of arbitrary values for the independent parameters such as C_f. Correlations from the above mentioned data may be used for these parameters.

3. The annulus wall boundary layer calculation methods are suitable only for lightly loaded compressor cascades and rotors. For heavily loaded compressors and turbines, complete three-dimensional calculation methods are needed. Also, the interaction effects between various endwall flow phenomena need to be accounted for in these calculations.

4. Most of the loss correlations available for the annulus wall boundary layers give only overall loss coefficients or overall loss in efficiency. Only Hanly's [66] correlation gives spanwise variation of the loss coefficient in the endwall region of a plane cascade. The rotor exit flow traverses mentioned in conclusion 1 may be used to develop a similar correlation for use in the simple analysis and design calculation method of flow in the turbomachinery. This correlation improves the preliminary design of turbomachinery.

5. Various methods are tried to improve the endwall in the turbomachinery. The two most successful methods are: the slots (without and with suction) in the casing over the rotor and grooves and fences on the blade suction surface near the endwalls. Detailed experimental investigations are needed to determine the precise nature of the mechanism in reducing the endwall losses.

6. In turbines, endwall profiling and cooling seems to reduce the secondary flow effects. Whether endwall profiling will reduce the secondary flow effects in compressors is yet to be tested.

7. A small amount of tip clearance is beneficial to compressors. Whereas in turbines, it is not beneficial but efforts to eliminate the tip clearance by means of shrouding introduces losses comparable to the tip clearance losses. Active control of clearance in actual high speed jet engine improve efficiency and reduce fuel consumption. Recent investigations indicate that the partial shrouding of blades improved the rotor performance even at large values of tip clearance.

8. Very few theoretical and experimental investigations are made in transonic and supersonic turbomachinery and with distorted inlet flow. The investigations for modelling and for improving the endwall flows in such situations are necessary since the present day turbomachines, especially jet engines, operate under high Mach number conditions.

SECONDARY FLOW CALCULATION

It has been mentioned in the previous chapter that most of the existing secondary flow theories are inviscid in nature, i.e. the effects of viscosity are not considered in the generation of secondary vorticity, but the endwall secondary flows are a direct result of viscosity. In this chapter, a simple derivation of secondary vorticity including the effect of viscosity and rotation, is derived. The generalized secondary vorticity equations in the rotating streamline coordinates of Lakshminarayana and Horlock [114] are utilized to derive simple equations for the streamwise variation of the secondary and the normal vorticity. Radial variation of the secondary vorticity at the exit of an isolated rotor is obtained and compared with the simple theory of ref. [199]. Details of the analysis follow.

Equation for Normal Vorticity $\omega_{n'}$

The equation for the normal component of the absolute voritcity in relative coordinate system is [114] (see Fig. 2 for the coordinate system)

$$\frac{\partial}{\partial s'}\left(\omega_{n'} W\right) = \frac{W}{\tau}\,\omega_{b'} - \frac{W\omega_{n'}}{a_{b'}}\frac{\partial a_{b'}}{\partial s'} + \frac{1}{\rho^2}\left[\frac{\partial p}{\partial s'}\frac{\partial \rho}{\partial b'} - \frac{\partial p}{\partial b'}\frac{\partial \rho}{\partial s'}\right] + \text{viscous terms} \qquad (17)$$

1 2 3 4 5

The flow is assumed to be incompressible and homogeneous. Therefore, term 4 in the above equation is zero. The only important term among viscous terms (assuming the eddy viscosity for the turbulent flow is constant) is $(\mu/\rho)\partial^2\zeta_{n'}/\partial b'^2$. Hence, equation (17) simplifies to,

$$\frac{\partial}{\partial s'}\left(\omega_{n'} W\right) = \frac{W}{\tau}\,\omega_{b'} - \frac{W\omega_{n'}}{a_{b'}}\frac{\partial a_{b'}}{\partial s'} + \left(\frac{\mu}{\rho}\right)\frac{\partial^2 \zeta_{n'}}{\partial b'^2} \qquad (18)$$

since,

$$\zeta_{n'} = \frac{\partial W}{\partial b'}$$

equation (18) is further simplified to

$$\frac{\partial}{\partial s'}\left(\omega_{n'} W\right) = \frac{W}{\tau}\,\omega_{b'} - \frac{W\omega_{n'}}{a_{b'}}\frac{\partial a_{b'}}{\partial s'} + \left(\frac{\mu}{\rho}\right)\frac{\partial^3 W}{\partial b'^3} \qquad (19)$$

Equation (19) can be further simplified by neglecting terms of small order. Equation (19) is normalized as follows.

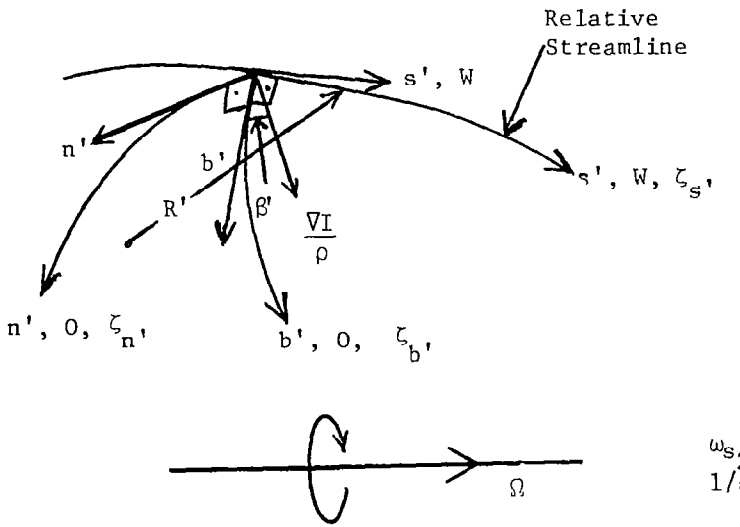

Figure 2. Relative Intrinsic Coordinate System

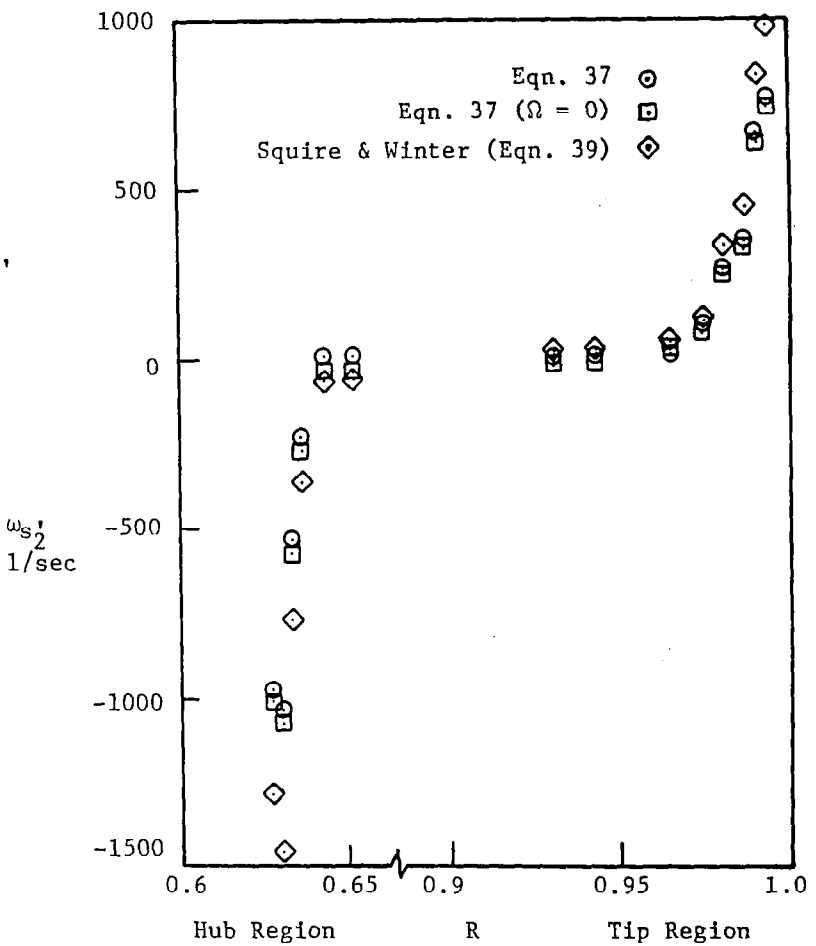

Figure 3. Distribution of Secondary Vorticity at the Exit of an Isolated Rotor

Let

$$\frac{W}{W_1} = \bar{W} \qquad \frac{s'}{C} = \bar{s} \qquad \frac{b'}{\delta_1} = \bar{b}$$

$$\frac{\omega_n'}{W_1/\delta_1} = \bar{\omega}_n \qquad \frac{\tau}{r_t} = \bar{\tau}$$

$$\frac{\omega_b'}{W_1/R_t'} = \bar{\omega}_b \qquad \frac{\Omega_n'}{\Omega} = \bar{\Omega}_n$$

$$\frac{a_b'}{r_t} = \bar{a}_b \qquad \frac{\Omega_b'}{\Omega} = \bar{\Omega}_b$$

where δ_1 = the wall boundary layer thickness at inlet

C = chord length at the tip

r_t = tip radius

R_t' = radius of curvature of relative streamline at the tip

W_1 = inlet relative velocity

Ω = rotational speed

For thin boundary layers, $\delta_1/C = 0(\varepsilon)$, $\delta_1/r_t = 0(\varepsilon_1)$ where $\varepsilon < 1$ and $\varepsilon_1 << 1$. Also, $W_1 = 0(U_t)$. Therefore, equation (19) in non-dimensionalized form is (dropping overbars for nondimensional quantities)

$$\frac{W_1^2}{\delta_1 C}\frac{\partial}{\partial s}\left(\omega_n \quad W\right) = \frac{W_1^2}{R_t' r_t}\left(\frac{W\omega_b}{\tau}\right) - \frac{W_1^2}{\delta_1 C}\left(\frac{W\omega_n}{a_b}\frac{\partial a_b}{\partial s}\right) + \frac{W_1}{\delta_1^3}\left(\frac{\mu}{\rho}\right)\frac{\partial^3 W}{\partial b^3}$$

which simplifies to,

$$\frac{\partial}{\partial s}\left(\omega_n \quad W\right) = \frac{\delta_1 C}{R_t' r_t}\left(\frac{W\omega_b}{\tau}\right) - \left(\frac{W\omega_n}{a_b}\frac{\partial a_b}{\partial s}\right) + \left[\frac{C}{\delta_1}\frac{1}{Re_\delta}\right]\frac{\partial^3 W}{\partial b^3} \qquad (20)$$

All terms in brackets of the equation (20) are of order 1. The coefficient of first term on the right hand side is of order $(\varepsilon_1) << 1$. Hence this term is neglected. The coefficient of last term includes the Reynolds number based on the wall boundary layer thickness. The coefficient is of order 1.

Neglecting terms of small order, the simplified equation for ω_n, is

$$\frac{\partial}{\partial s'}\left(\omega_n', W\right) = -\frac{W\omega_n'}{a_b'}\frac{\partial a_b'}{\partial s'} + \frac{\mu}{\rho}\frac{\partial^3 W}{\partial b'^3} \qquad (21)$$

Equation (21) can be further simplified as follows. The continuity equation in s', n', b' system is

$$\frac{\partial}{\partial s'}(a_{n'}, a_{b'}, W) = 0 \tag{22}$$

or

$$\frac{1}{a_{n'}}\frac{\partial a_{n'}}{\partial s'} + \frac{1}{a_{b'}}\frac{\partial a_{b'}}{\partial s'} + \frac{1}{W}\frac{\partial W}{\partial s'} = 0 \tag{23}$$

Hence equation (21) becomes

$$\omega_{n'}\frac{\partial W}{\partial s'} + W\frac{\partial \omega_{n'}}{\partial s'} = -\frac{W\omega_{n'}}{a_{b'}}\frac{\partial a_{b'}}{\partial s'} + \frac{\mu}{\rho}\frac{\partial^3 W}{\partial b'^3}$$

Hence the equation for the normal vorticity along the relative streamline, including the effects of rotation and viscosity (or turbulence) is given by

$$\frac{\partial \omega_{n'}}{\partial s'} + \omega_n\left(\frac{1}{a_{b'}}\frac{\partial a_{b'}}{\partial s'} + \frac{1}{W}\frac{\partial W}{\partial s'}\right) = \frac{\mu}{\rho}\frac{\partial^3 W}{\partial b'^3} \tag{24}$$

Equation for Secondary Vorticity $\omega_{s'}$

The equation for the streamwise component of the absolute vorticity in the relative streamline coordinate system is given by [114]

$$\frac{\partial}{\partial s'}\left(\frac{\omega_{s'}}{W}\right) = \underset{1}{\frac{2\omega_{n'}}{WR'}} + \underset{2}{\frac{2(\Omega_{b'}\omega_{n'} - \Omega_{n'}\omega_{b'})}{W^2}} - \underset{3}{\frac{1}{\rho^2 W^2}\left[\frac{\partial p}{\partial b'}\frac{\partial \rho}{\partial n'} - \frac{\partial p}{\partial n'}\frac{\partial \rho}{\partial b'}\right]} + \underset{4}{\text{viscous terms}} \tag{25}$$

Assuming incompressible flow and retaining only the most important viscous term, equation (25) is simplified to

$$\frac{\partial}{\partial s'}\left(\frac{\omega_{s'}}{W}\right) = \frac{2\omega_{n'}}{WR'} + \frac{2}{W^2}(\Omega_{b'}\omega_{n'} - \Omega_{n'}\omega_{b'}) + \frac{\mu}{\rho W^2}\left(\frac{\partial^2 \omega_{s'}}{\partial b'^2} - 2\frac{\partial^2 \Omega_{s'}}{\partial}\right) \tag{26}$$

Equation (26) is simplified by nondimensionalizing it. Let

$$\frac{\omega_{s'}}{C/R'_t \quad W_1/\delta} = \bar{\omega}_s \qquad \frac{R'}{R'_t} = \bar{R} \qquad \frac{\Omega_{s'}}{\Omega} = \bar{\Omega}_s \qquad \frac{\Omega_{b'}}{\Omega} = \bar{\Omega}_b \qquad \frac{b'}{\delta} = \bar{b}$$

Hence the nondimensionalized form of equation (26) is

$$\frac{CW_1}{R_t'\delta}\frac{1}{CW_1}\frac{\partial}{\partial s}\left(\frac{\bar{\omega}_s}{\bar{W}}\right) = \frac{W_1}{\delta W_1 R_t'}\left(\frac{2\bar{\omega}_n}{\bar{W}\bar{R}}\right) + \frac{2}{W_1^2\bar{W}^2}\left(\Omega\,\bar{\Omega}_b\,\overline{\omega_n}\,\frac{W_1}{\delta} - \Omega\,\bar{\Omega}_n\,\frac{W_1}{R_t'}\,\bar{\omega}_b\right)$$

$$- \frac{\mu}{\rho}\frac{1}{W_1^2\bar{W}^2}\left(\frac{C}{R_t'}\frac{W_1}{\delta^3}\frac{\partial^2\bar{\omega}_s}{\partial\bar{b}^2} - \frac{2\Omega}{\delta^2}\frac{\partial^2\bar{\Omega}_s}{\partial\bar{b}^2}\right)$$

$$\frac{\partial}{\partial\bar{s}}\left(\frac{\bar{\omega}_s}{\bar{W}}\right) = \left(\frac{2\bar{\omega}_n}{\bar{W}\bar{R}}\right) + \frac{2(\Omega\, r_t)R_t'}{W_1\, r_t}\left(\frac{\bar{\Omega}_b\bar{\omega}_n}{\bar{W}^2}\right) - \frac{2\Omega r_t}{W_1}\frac{\delta}{r_t}\left(\frac{\bar{\Omega}_n\bar{\omega}_b}{\bar{W}^2}\right) + \frac{\mu}{\rho}\frac{1}{W_1}\frac{C}{\delta^2}\left(\frac{1}{\bar{W}^2}\frac{\partial^2\bar{\omega}_s}{\partial\bar{b}^2}\right)$$

(1) $\qquad$ (ε_1) $\qquad$ $(1/R_{e\delta})(1/\varepsilon)$

$$- \frac{2\Omega r_t}{W_1}\frac{R_t'}{r_t}\frac{\mu}{\rho}\frac{1}{W_1\delta}\left(\frac{1}{\bar{W}^2}\frac{\partial^2\bar{\Omega}_s}{\partial\bar{b}^2}\right) \qquad (27)$$

$(1/R_{e\delta})$

In equation (27), all the bracketed terms are of order 1. The order of magnitude of the coefficients of these terms are given below them. Hence, we can neglect the last term. The third and fourth terms may be of the same magnitude, even though they are of one order of magnitude less than terms 1 and 2. Hence, the equation for the secondary vorticity in a rotor blade row is,

$$\frac{\partial}{\partial s'}\left(\frac{\omega_{s'}}{W}\right) = \frac{2\omega_{n'}}{WR'} + \frac{2}{W^2}\left(\Omega_{b'}\,\omega_{n'} - \Omega_{n'}\,\omega_{b'}\right) + \frac{\mu}{\rho W^2}\frac{\partial^2\omega_{s'}}{\partial b'^2} \qquad (28)$$

For stationary blade rows,

$$\frac{\partial}{\partial s}\left(\frac{\omega_s}{V}\right) = \frac{2\omega_n}{VR} + \frac{\mu}{\rho V^2}\frac{\partial^2\omega_s}{\partial b^2} \qquad (29)$$

Method of Solution for an Axial Flow Compressor Rotor

The following assumptions are made in the integration of vorticity equations:

1. W varies linearly with s', i.e., $\partial W/\partial s'$ = constant. Hence, $W = W_1 + (W_2 - W_1)s/C$.

2. Since b' direction is nearly coincident with the r direction, $\Omega_{b'} \simeq 0$. Also $\Omega_{n'} \simeq \Omega \sin\lambda$.

3. Experimental or assumed value for ν_t is used.

4. The blades are assumed to be of circular arc type. Hence, R' is assumed constant.

5. Linear variation of a_b' is assumed along s' direction. Hence $\partial a_b'/\partial s' =$ constant, or $a_b' = a_{b_1}' + (a_{b_2}' - a_{b_1}')s/C$.

6. W profile in b' direction is assumed for use in the viscous terms.

7. $\zeta_n' = \partial W/\partial b'$, this relation is used in viscous terms.

8. $\omega_b' = W/R' - \partial W/\partial n'$ (exact relation).

9. $\omega_s' = 2\varepsilon_R(\partial W/\partial b')$ for use in viscous terms.

10. The gradients $\partial W/\partial b'$ and $\partial W/\partial b'$ are assumed to be linear in s' (obtained from assumption 1).

Solution of Normal Vorticity Equation

Equation for normal vorticity along s' is

$$\frac{\partial \omega_n'}{\partial s'} + \omega_n' \left[\frac{1}{W}\frac{\partial W}{\partial s'} + \frac{1}{a_b'}\frac{\partial a_b'}{\partial s'}\right] = \frac{\nu_t}{W}\frac{\partial^2 \omega_n'}{\partial b'^2} \tag{30}$$

Equation (30) is of the following form, where the viscous term is approximated by a source term of the form $\gamma(s',b')$.

$$\frac{\partial \omega_n'}{\partial s'} + f(s',b')\omega_n' = \gamma(s',b')$$

Multiply both sides with $e^{\int f ds'}$

$$\left[\frac{\partial \omega_n'}{\partial s'} + f\,\omega_n'\right] e^{\int f ds'} = \gamma e^{\int f ds'}$$

$$\frac{\partial}{\partial s'}\left[\omega_n' e^{\int f ds'}\right] = \gamma e^{\int f ds'}$$

Integrating above equation along a streamline from 0 to s,

$$\omega_{n'}\, e^{\int f ds'}\Big|_o^s = \int \gamma e^{\int f ds'}\, ds'\Big|_o^s$$

where

$$e^{\int f ds'} = \exp\left[\int \frac{d}{ds}\left(\ell n(Wa_{b'})\right) ds\right] = Wa_{b'}$$

Therefore,

$$\omega_{n'}\, Wa_{b'} - \omega_{n_1'}\, W_1 a_{b_1'} = \int_o^s a_{b'}\left[\nu_t \frac{\partial^2 \omega_{n'}}{\partial b'^2}\right] ds' \tag{31}$$

Using the assumptions made for the variation of W and other quantities,

$$\omega_{n'} = \frac{\omega_{n_1'}\, W_1 a_{b_1'}}{W\, a_{b'}} + \frac{\nu_t}{c^2 W a_{b'}}\left[a_{b_1'}\, sC^2 \frac{\partial^3 W_1}{\partial b'^3} + \frac{a_3}{3}\frac{\partial^3 W_3}{\partial b'^3} + \left(a_3\, C \frac{\partial^3 W_1}{\partial b'^3} + a_{b_1'} C \frac{\partial^3 W_3}{\partial b'^3}\right)\frac{s^2}{2}\right] \tag{32}$$

where

$$W_3 = (W_2 - W_1) \quad \text{and} \quad a_3 = a_{b_2'} - a_{b_1'}$$

Solution of Secondary Vorticity Equation

The equation for the secondary vorticity along s' is

$$\frac{\partial}{\partial s'}\left(\frac{\omega_{s'}}{W}\right) = \frac{2}{R'}\frac{\omega_{n'}}{W} - \frac{2\Omega_{n'}\omega_{b'}}{W^2} + \nu_t \frac{1}{W^2}\frac{\partial^2 \omega_{s'}}{\partial b'^2} \tag{33}$$

Integrating equation (33) w.r.t. s' from 0 to s,

$$\frac{\omega_{s'}}{W} = \frac{2}{R'}\int_o^s \frac{\omega_{n'}}{W}\, ds' - 2\Omega_{n'}\int_o^s \frac{\omega_{b'}}{W^2}\, ds' + \nu_t \int_o^s \frac{1}{W}\frac{\partial^2 \omega_{s'}, ds'}{\partial b'^2} + \frac{\omega_{s_1'}}{W_1}$$

Assuming linear variation of W along s' and exact expression for $\omega_{b'}$, the following equation for $\omega_{s'}$ at a distance s (along s') from the blade leading edge is derived.

$$\frac{\omega_{s'}}{W} = \frac{\omega_{s_1'}}{W_1} - \frac{2\Omega_{n'}C}{W_1X}\left\{\ell n(1+Y)\left[\frac{1}{W_1X}\frac{\partial}{\partial n'}(W_1X)\right] + \frac{X}{(1+Y)}\frac{\partial(W_1X)}{\partial n'} - \frac{Z}{W_1}\frac{\partial W_1}{\partial n'}\right\}$$

$$+ \frac{\nu_t C}{W_1^2 X}\varepsilon\left\{\frac{[\ell n(1+Y)+Z]}{X}\frac{\partial^3(W_1X)}{\partial b'^3} - Z\frac{\partial^3 W_1}{\partial b'^3}\right\} + \frac{2C^2}{R'(W_1a_3 - W_3a_{b_1'})}\left\{\omega_{n_1'}W_1a_{b_1'}\right.$$

$$\left\{-\frac{W_3 s}{(W_1C + W_3 s)W_1 C} + \frac{a_3}{(W_1a_3 - a_{b_1'}W_3)C}\ell n\left[\frac{(a_{b_1'}C + a_3 s)}{(W_1C + W_3 s)}\frac{W_1}{a_{b_1'}}\right]\right\}$$

$$+ \frac{1}{W_3}\left(\nu_t\, a_{b_1'}\frac{\partial^3 W_1}{\partial b'^3} - \frac{2\Omega_{n'}W_3 a_{b_1'}}{C}\right)\left\{-\frac{W_1 a_3^2 s}{W_3 a_{b_1'}(a_{b_1'}C + a_3 s)}\right.$$

$$\left.+ \frac{a_{b_1'}W_3}{(W_1a_3 - W_3a_{b_1'})a_3}\ell n\left[\frac{(W_1C + a_3 s)}{(a_{b_1'}C + a_3 s)}\frac{a_{b_1'}}{W_1}\right]\right\} + \left[\frac{\nu_t}{2}\left(\frac{a_3\partial^3 W_1}{\partial b'^3} + a_{b_1'}\frac{\partial^3 W_3}{\partial b'^3}\right)\right.$$

$$\left.- \frac{\Omega_{n'}W_3 a_3}{C}\right]\left\{-\frac{W_1 s}{W_3(W_1C + W_3 s)} + \frac{1}{(W_1a_3 - W_3a_{b_1'})}\left[\frac{a^2 b_1'}{a_3}\ell n\left(1 + \frac{a_3 s}{a_{b_1'}C}\right)\right.\right.$$

$$\left.\left.+ \frac{W_1^2 a_3}{W_3^2}\ell n\left(\frac{W_1C + W_3 s}{W_1 C}\right)\right]\right\} + \frac{a_3}{C}\nu_t\frac{\partial^3 W_3}{\partial b'^3}\left\{-s\left[\frac{W_1 s}{W_3(W_1C + W_3 s)}\right.\right.$$

$$\left.- \frac{1}{(W_1a_3 - W_3a_{b_1'})}\left(\frac{a_{b_1'}^2}{a_3} + \frac{W_1^2 a_3}{W_3^2}\right)\right] + \frac{\ell n[1 + W_3 s/W_1 C]}{(W_1a_3 - W_3a_{b_1'})}\left[\frac{sW_1^2 a_3}{W_3^2}\right.$$

$$\left.- \frac{W_1^2 C}{W_3^3}(W_1a_3 - W_3a_{b_1'}) - \frac{W_1^3 a_3 C}{W_3^3}\right] + \frac{\ell n(1 + a_3 s/a_{b_1'}C)}{(W_1a_3 - W_3a_{b_1'})}\left(\frac{a_{b_1'}^2 s}{a_3} - \frac{a_{b_1'}^3 C}{a_3^2}\right)$$

$$\left.\left.- \frac{s\,C}{(W_1a_3 - W_3a_{b_1'})}\left[\frac{a_{b_1'}^3}{a_3^2}\ell n(a_{b_1'}C + a_3 s) + \frac{W_1^3 a_3}{W_3^3}\ell n(W_1C + W_3 s)\right]\right\}\right\} \tag{34}$$

where $X = W_2/W_1 - 1$, $Y = Xs/C$ and $Z = Y/(1+Y)$. Equation (34) is used to determine the secondary vorticity at the rotor exit at various streamlines.

Calculation of the Secondary Vorticity for an Isolated Rotor

Detailed flow measurements at the inlet and exit of an isolated rotor at various flow coefficients are reported by Thinh [175]. Equation (34) is used to calculate the secondary vorticity developed along various streamlines. The method of calculation is outlined below.

1. The primary flow is calculated from the Douglass Neumann cascade program of Eskay [200]. Since the above computer program is essentially two-dimensional, the exit relative flow angle is corrected for the change in the inlet and exit axial velocity according to ref. [201]. The change in the deviation angle due to the axial velocity change is given by,

$$\Delta\delta^* = \frac{(AVR - 1)}{AVR}\cos^2\beta_2\left\{\tan\beta_2 + \frac{\left(\frac{\pi K\sigma[G/C + \alpha/4]\cos\beta_m[(AVR+1)^2 - 4]}{AVR - 1} - \frac{2\pi K\sigma\tan\beta_1}{AVR\cos\beta_m\sec^2\beta_1}\right)}{8 + \pi K\sigma[G/C + \alpha/4]\cos\beta_m[(AVR+1)\tan\beta_2 + 2\tan\beta_1]}\right\} \quad (35)$$

where AVR = ratio of exit to inlet velocity

β_1 = inlet relative flow angle obtained from the experiment

β_2 = exit relative flow angle obtained from the Douglass Neumann program

β_m = mean relative flow angle = $\tan^{-1}[(\tan\beta_1 + \tan\beta_2)/2]$

G = maximum camber

$\alpha = \beta_1 - \lambda$

σ = solidity

C = chord

λ = stagger angle

K = cascade influence coefficient

The measured axial velocity at a station far downstream of the rotor, where the flow is mostly free of end wall flow effects, is used for the calculation of AVR.

2. The change in the deviation angle is subtracted from the exit relative flow angle obtained from the Douglass Neumann program and the exit relative velocity is calculated as follows:

$$W_2 = W_1 \text{ AVR} \frac{\cos\beta_1}{\cos(\beta_2 - \Delta\delta^*)} \tag{36}$$

3. The terms ζ_{n_1} $(=\partial W_1/\partial b)$, $\partial^3 W_1/\partial b'^3$ and $\partial^3 W_2/\partial b'^3$ are approximated by the finite differences. For example, at j^{th} streamline

$$\zeta_{n_{1,j}} = \frac{(W_{1,j+1} - W_{1,j})}{(b_{j+1} - b_j)}$$

The terms $\partial W_1/\partial n'$ and $\partial W_2/\partial n'$ are assumed to be zero at the blade trailing edge.

4. With the above input, equation (34) is used to calculate the secondary vorticity at the rotor trailing edge (i.e., s = c). Equation (34) is simplified for this case, since $a_{b_1'} \simeq a_{b_2'}$ for all streamlines. The simplified equation is

$$\frac{\omega_{s'}}{W} = \frac{\omega_{s_1'}}{W_1} + \frac{2\omega_{n_1'}s}{W_1 R'(1+Y)} + \frac{\nu_t C}{W_3^2}\left\{\left(\frac{2C}{R'}\frac{\partial^3 W_1}{\partial b'^3} + \varepsilon_R \frac{\partial^3 W_3}{\partial b'^3}\right)[\ell n(1+Y) - Z]\right.$$

$$+ \frac{W_1}{W_3}\frac{C}{R'}\frac{\partial^3 W_3}{\partial b'^3}[Z - 2\ell n(1+Y)] + \left.\frac{\varepsilon_R s\, W_3^2}{W_1(W_1 C + W_3 s)}\frac{\partial^3 W_1}{\partial b'^3}\right\}$$

$$- 2\Omega_{n'}C\left\{\frac{1}{W_3 R'}[2\ell n(1+Y) - 2Z] - \left[\frac{\partial W_1}{\partial n'}\frac{s}{W_1(W_1 C + W_3 s)}\right.\right.$$

$$\left.\left. + \frac{\partial W_3}{\partial n'}\frac{[\ell n(1+Y) - Z]}{W_3^2}\right]\right\} \tag{37}$$

In equation (37) let $\nu_t = 0$, $\Omega = 0$, $s = C$ and $W_1 = W_2$. Then the equation simplifies to

$$\omega_{s_2'} - \omega_{s_1'} = 2\,\omega_{n_1'}\frac{C}{R'} \tag{38}$$

For small turning angles, $R' = C/\varepsilon_R$. Hence, equation (37) reduces to

$$\omega_{s_2'} - \omega_{s_1'} = 2\,\omega_{n_1'}\,\varepsilon_R \tag{39}$$

This is the Squire and Winters [199] expression for a cascade. ε_R is the relative flow turning angle.

The results obtained from equation (37) for Nguyen's rotor are shown in Figure 3. The secondary vorticity is calculated for $\Omega = 0$ and $\Omega = 183$ rad/sec. The case with $\Omega = 0$ corresponds to the equation by Loos [202]. His expression for secondary vorticity for a rotating cascade without inlet secondary vorticity is

$$\omega_{s_2'} = \frac{\omega_{n_1'} \varepsilon_R}{\ell n(W_1/W_2)} \left(\frac{W_1}{W_2} - \frac{W_2}{W_1}\right) \tag{40}$$

The results obtained from this expression agree very well with those of the equation (37) (with $\omega_{s_1'} = \nu_t = \Omega = 0$)

$$\omega_{s_2'} = 2\, \omega_{n_1'} \frac{s}{R'} \frac{W_2/W_1}{(1+Y)} \tag{41}$$

Secondary vorticity obtained from Squire and Winter's expression is also shown in Figure 3 and compared with those obtained from equation (37) In general, the agreement is poor. This is to be expected as Squire and Winter's expression does not take the flow acceleration effects in generation of secondary vorticity. Also the effect of rotation on secondary vorticity is found to be small for this rotor.

Concluding Remarks

Secondary vorticity at the exit of a fan rotor is calculated, taking the effects of rotation and viscosity into account. The effect of rotation on secondary vorticity generation for Thinh's rotor is found to be small.

The primary flow field necessary for the calculation of secondary vorticity is obtained from the Douglass Neumann cascade program. This program is essentially two-dimensional. Considerable improvement in the primary flow field calculation (hence secondary flow calculation) can be obtained, if the streamline curvature method (which solves axisymmetric equations of flow in turbomachinery) is employed. The streamline curvature program [203] has to be modified for the following effects.

1. Correlations for the deviation angles and profile losses at the blade row exit.

2. Variable streamline spacings: very small streamline spacings are necessary in the annulus wall boundary layers.

The streamline curvature method has an added advantage of calculating the flow through a complete axial flow compressor stage (consisting of inlet guide vanes, rotor and stator). The secondary velocity field can be calculated using the method similar to that of reference [118].

DESCRIPTION OF EXPERIMENTAL FACILITY AND METHODS

The primary objective of the present investigation is to obtain an understanding of the endwall flows in axial flow compressors and model the same. Since very little data in the endwall region of a real machine is available, an experimental investigation is undertaken to measure the flow-field (pressure, velocity, and turbulence fields) in the endwall region of a low speed, moderately loaded axial flow compressor. The facility used for this investigation is located in the Turbomachinery Laboratory of the Department of Aerospace Engineering at The Pennsylvania State University. This chapter gives the description of the facility, data acquisition systems, and data reduction methods.

The Axial Flow Compressor Facility

A schematic diagram of the axial-flow compressor facility is shown in Figure 4. The facility consists of an inlet guide vane row (IGV), a rotor blade row, and a stator blade row. The compressor stage was designed by Smith [204] for secondary flow investigations. The stage is modified for measurement of relative flow inside and exit of the rotor blade row. This is achieved by mounting a rotating probe traverse mechanism, downstream of the rotor. The major features of the facility are given in Table IV and in ref. 205. The mass flow through the compressor is controlled by an aerodynamically designed throttle, placed downstream of an auxiliary fan. The blade pitch of the rotor blade of the auxiliary fan can be changed to control the mass flow through the research compressor. Also, the speed of the research rotor can be varied to control the mass flow.

All the endwall flow measurements are performed at the flow coefficient of 0.555. The rotor speed is held constant at 1066 rpm. The speed is measured by a photo cell arrangement in the data transmission system.

The overall performance measurements are made at various flow coefficients, by varying the throttle opening. The speed is held constant, thus keeping the Reynolds number constant at 5.3×10^5 based on the tip speed and chord. For the rotor blade static pressure measurements, the throttle opening is kept constant and the speed is varied. The effect of Reynolds number is assumed negligible, since it is varied from 4.63×10^5 to 5.6×10^5.

More details on the facility, including aerodynamic and mechanical details, are given by Lakshminarayana [205].

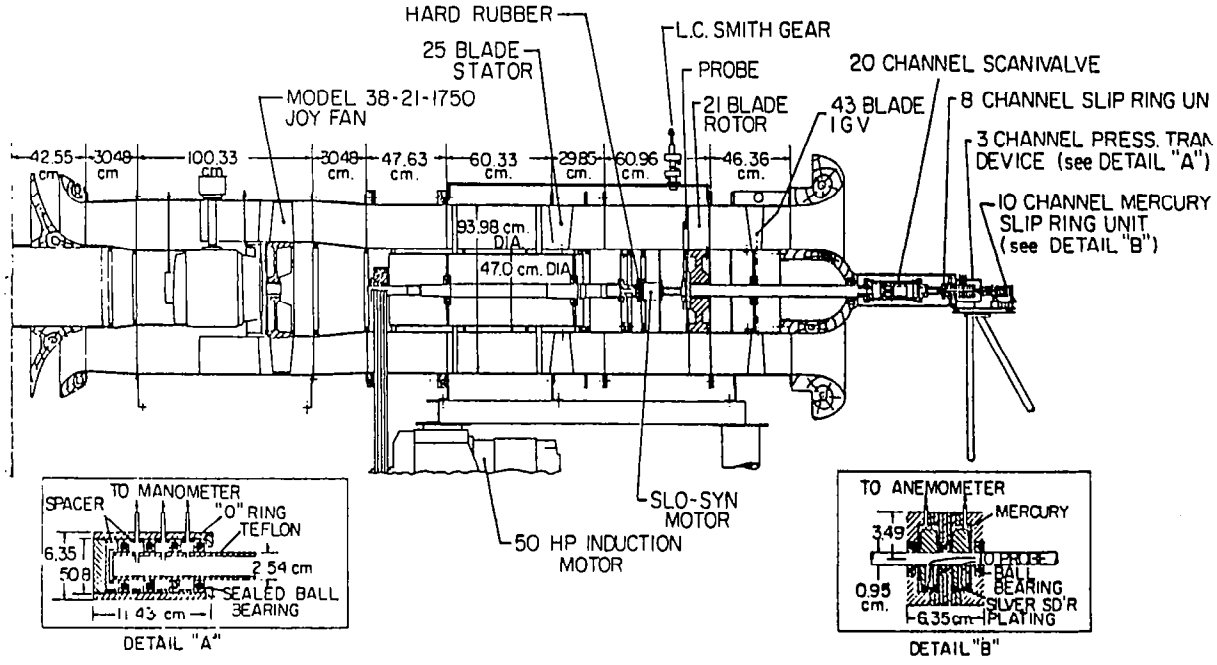

Figure 4. PSU Axial Flow Compressor Facility

Table IV. Axial-Flow Compressor Facility Specifications

Particulars	IGV	Rotor	Stator
1. Number of Blades	43	21	25
2. Rotor Speed (Operating)	--	1066 (rpm)	--
3. Tip Diameter of Rotor		0.9322 m (36.7 inch)	
4. Hub/Tip Ratio		0.5	
5. Blade Element	NACA 65-010	Modified NACA 65 Series (see Table V)	
6. Tip Clearance		2.26 mm at L.E. (0.089 in.) 2.31 mm at T.E. (0.091 in.)	
7. Electric Power		37.29 KW (50 HP)	
8. Solidity at Tip	1.585	1.091	1.197
9. Inlet-Static-Pressure (Wall) Inlet Velocity Flow Coefficient		5.08 cm (2") of H_2O 28.9 m/sec (94.7 ft/sec) 0.555	
10. Auxiliary Fan		Series 1000 Joy Axivane Fan #0 to #16 Blade Setting Fan Dia. 0.9652 m (38 in.)	
11. Fan Drive Power		37.29 KW (50 HP)	

Research Rotor

The research rotor has 21 cambered and twisted blades and has a tip diameter of 0.9322 m (36.7 in.). The hub-tip ratio is 0.5. The blade elements are of modified NACA 65-010 basic profile. The blades have increasing stagger angles and blade chords and decreasing thicknesses along the span. The relevant details of the rotor blades along with those of the IGV and stator blade rows are given in Table V. The rotor blades are made out of cast aluminum with T-shaped roots and inserted in the slots of the hub.

The rotor has one fully instrumented blade passage at various axial and radial locations on the suction surface and pressure surfaces to measure blade static pressures. The axial and radial locations are:

Z = 0.083, 0.125, 0.167, 0.25, 0.417, 0.583, 0.75, 0.833

R = 0.507, 0.587, 0.67, 0.75, 0.832, 0.918, 0.962, 0.988, 0.996, 0.998

The rotor hub is also provided with blade static taps between the blade passage and downstream of the blade passage. The static pressure taps in the tip region of the blade provide a quick understanding of endwall flows in terms of lift coefficient. The pressure signals from these taps are transmitted through the rotating scanivalve and the rotating pressure transfer of the data transmission system.

Probes and Instruments

The probes and instruments used in this program are described in individual sections.

Some of the data and measurement techniques on rotor end wall flow have already been published and, therefore, will not be repeated here. The data on rotor end wall flow was presented and interpreted in ref. 63. A five hole probe was employed in this investigation.

Table V. Blade Element Details

Particulars	Radius Ratio																	
	Inlet-Guide-Vane						Rotor						Stator					
Radius Ratio	0.5	0.6	0.7	0.8	0.9	1.0	0.5	0.6	0.7	0.8	0.9	1.0	0.5	0.6	0.7	0.8	0.9	1.0
Chord, cm (in)	5.45 (2.15)	6.54 (2.58)	7.64 (3.01)	8.72 (3.43)	9.80 (3.86)	10.90 (4.29)	12.39 (4.88)	12.68 (4.99)	13.25 (5.22)	13.68 (5.39)	14.41 (5.67)	15.41 (6.07)	8.83 (3.48)	9.80 (3.86)	10.37 (4.08)	10.95 (4.31)	12.39 (4.88)	13.97 (5.50)
Spacing, cm (in)	3.46 (1.34)	4.69 (1.61)	4.77 (1.88)	5.45 (2.15)	6.03 (2.41)	6.91 (2.72)	6.91 (2.72)	8.35 (3.29)	9.80 (3.86)	11.24 (4.42)	12.68 (4.99)	14.12 (5.56)	5.76 (2.27)	6.91 (2.72)	8.35 (3.29)	9.51 (3.74)	10.66 (4.20)	11.67 (4.59)
Camber (C_{ℓ_o} for Rotor & Stator)	-5.0 (deg)	6.0 (deg)	16.0 (deg)	24.0 (deg)	32.0 (deg)	45.0 (deg)	1.35	1.45	1.5	1.5	1.48	1.32	1.7	1.4	1.05	0.8	0.5	0.4
Thickness (t/C x 100)	13.0	12.0	10.5	9.5	8.5	8.0	9.50	9.1	7.6	6.5	5.9	5.1	-	-	-	-	-	-
Chord Angle,° (Stagger)	-1.0	3.0	7.5	12.0	16.0	22.0	22.5	26.0	28.5	34.0	39.0	45.0	16.5	24.0	31.0	37.0	42.0	50.0
Blade Outlet Angle, °							9.5	13.5	16.0	19.5	26.0	33.5						

RADIAL DISTRIBUTION OF FLOW PROPERTIES AND BLADE ELEMENT PERFORMANCE AT DESIGN AND OFF DESIGN CONDITIONS

The overall performance of the Axial Flow Compressor is discussed in this chapter. The overall performance consists of determining pressure rise coefficient across the rotor, $\bar{\psi}$, and across the stage, $\bar{\psi}_s$, at various flow coefficients, $\bar{\phi}$. These quantities are determined from the radial survey of flow properties at various axial locations of the facility. These radial distribution of flow properties are also used in the discussion of the annulus wall boundary layer characteristics. Other preliminary work consists of

1. Unsteady and axisymmetry test at the compressor inlet at $\bar{\phi} = 0.54$.
2. IGV wake pressure and hot-wire probe measurements at $\bar{\phi} = 0.556$.
3. Rotor inlet flow measurements in the end wall region at $\bar{\phi} = 0.556$.
4. Static pressure distribution on the rotor blades and the rotor hub at $\bar{\phi} = 0.54$, 0.55, 0.57, and 0.60.

Compressor Inlet Measurements

In order to determine the uniformity and unsteadiness of the incoming flow, the hot-wire probe is used to measure the radial distribution of the mean velocities and turbulence intensities at three tangential locations (120 degrees apart) at the inlet.

A dual sensor TSI hot-wire probe is used to measure the mean and turbulence velocities. The radial distribution of mean velocities at the inlet are shown in Figure 5. These tests were carried out at slightly different entry velocities. The mean velocities normalized with the velocities obtained from the casing wall static pressures are also shown. The agreement between the velocities at all the tangential stations is good, thus confirming the axisymmetric nature of the inlet flow.

The radial distribution of turbulence intensities at the three tangential stations is also shown in Figure 5. The intensities at stations 1 and 2 are nearly constant at 0.5 percent, except in the hub and casing regions. The values near the hub are not shown since they are very high. At station 3, the turbulence intensities are higher than those at station 1 and 2. To reduce the turbulence intensities at station 3, a grid was attached to the bellmouth near the station 3. Turbulence intensities increased with the grid. Therefore, it was discarded and all future experiments were carried out without any modification to the inlet. The higher turbulence intensities at station 3 are attributed to the proximity of this station to the ground. Attempts to detect the ground vortex by means of smoke visualization failed, indicating that the vortex is weak.

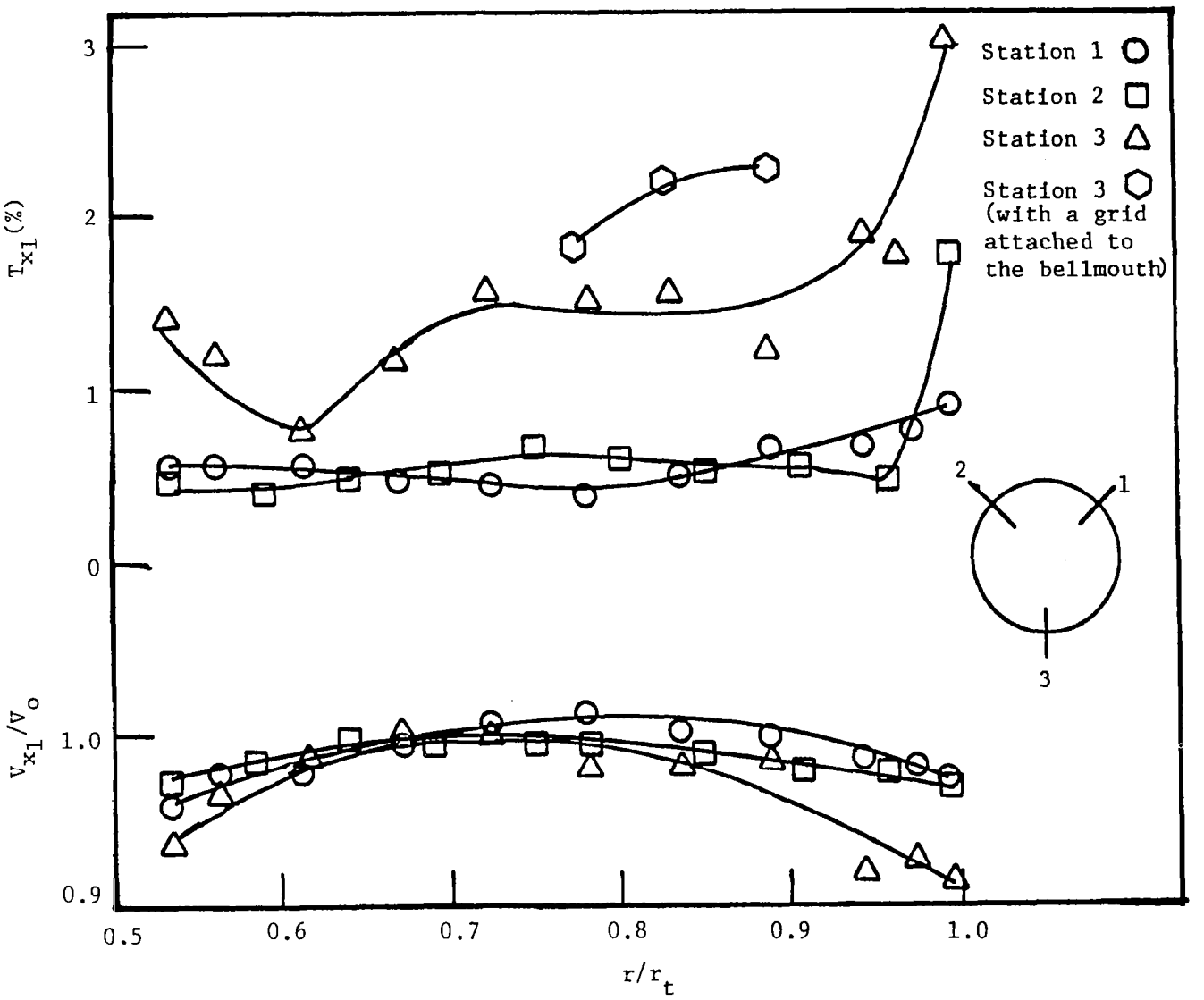

Figure 5. Radial Distribution of Mean Velocities and Turbulence Intensities at IGV Inlet ($\bar{\phi}$ = 0.54)

Overall Performance, Radial Distribution of Flow Properties and Blade Element Performance

Experimental Technique

In order to determine the overall performance of the compressor, radial survey of flow properties were measured at the IGV inlet and the exits of IGV, rotor and stator. A three-hole wedge probe manufactured by the United Sensor Corporation was traversed from hub to tip at each of these axial stations at five different throttle settings. The flow angle was determined by nulling the pressures from the side holes of the wedge probe. The side holes were also calibrated for the static pressure. The stagnation pressure was measured by the central hole of the probe. A traverse mechanism was used to traverse the probe in the radial direction and also to rotate the probe along its axis. The accuracy of the wedge probe measurements were checked by comparing the mass averaged axial velocity measured at the axial stations with that obtained from the stagnation pressure and the wall static pressure at the IGV inlet. The agreement has always been within 3 percent.

The radial survey of the flow properties were carried out at five throttle openings. For each throttle opening, radial surveys were carried out at four axial stations, at compressor (or IGV) inlet, exits of IGV, rotor and stator blade rows. The wall static pressures were also measured at the hub and casing to check the validity of static pressure traverses. All these measurements were taken at a constant speed of 1100 rpm.

The flow properties obtained from these measurements were used to determine the overall performance of the compressor and the blade element performance of the blade rows.

Overall Performance

The overall performance of the research rotor, in terms of mass averaged flow coefficient, $\bar{\phi}$, versus mass averaged stagnation pressure coefficient, $\bar{\psi}$, is shown in Figure 6. Also shown in this figure is the mass averaged Euler's efficiency. The maximum pressure rise and efficiency occur at the flow coefficient of 0.54. This flow coefficient is taken as the design flow coefficient. Below this flow coefficient, the pressure rise coefficient and the efficiency falls rapidly.

Figure 7a shows the overall performance of the stage in terms of mass averaged stagnation pressure rise coefficient across the stage, $\bar{\psi}_s$, versus the mass averaged flow coefficient, $\bar{\phi}$. The maximum $\bar{\psi}_s$ occurs at a flow coefficient of 0.57, which is higher than the flow coefficient where maximum stagnation pressure rise across the rotor. This indicates that the rotor and stator are not properly matched at the design flow coefficient. This may be due to the unusually large spacing between the rotor and the stator.

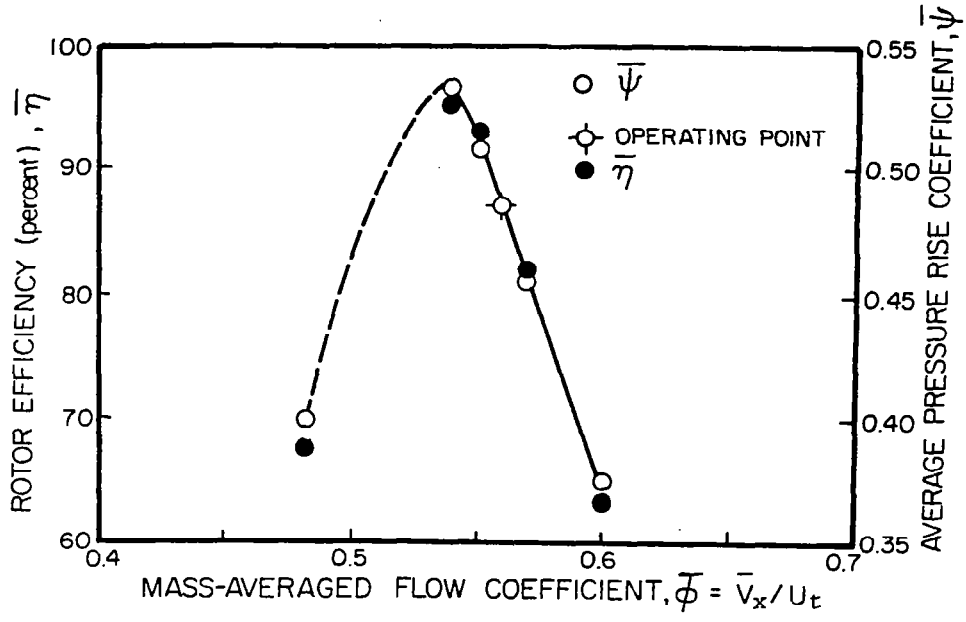

Figure 6. Overall Performance of the Rotor

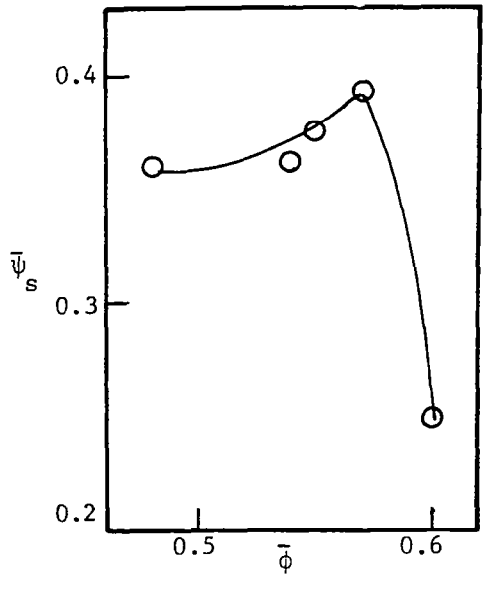

Figure 7a. Overall Performance of the Stage

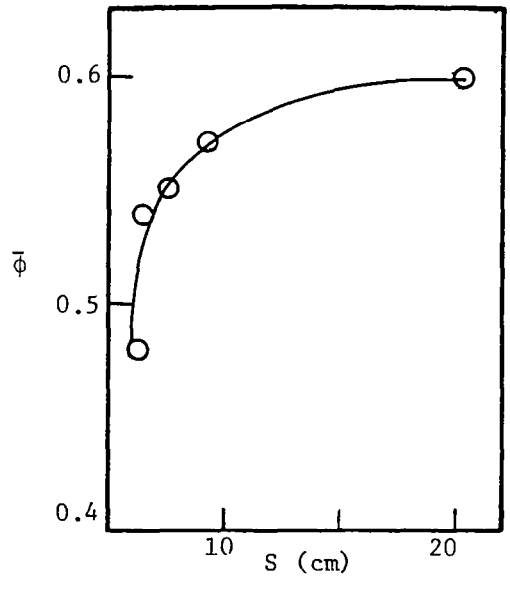

Figure 7b. Throttling Characteristics

A plot of flow coefficient versus the throttle opening, S, is shown in Figure 7b. As the throttle opening becomes smaller, the flow coefficient drops rapidly. This is especially true near the design flow coefficient, indicating the small amount of stall margin available for this compressor.

Radial Distribution of Flow Properties

From the radial survey of the flow angle and the pressures, the radial distribution of the axial, tangential, and the total velocities were determined at the exit of each of the blade rows. For the rotor exit, radial distribution of relative tangential and total velocities, relative flow angles, Euler's pressure rise coefficient and efficiency were also determined.

The radial distribution of flow properties are compared with these obtained from the Streamline Curvature Method [203]. In general, the agreement is good except near the hub and tip. In the following sections, radial distributions of the flow properties at several flow coefficients ($\bar{\phi}$ = 0.48, 0.54, 0.55, 0.57, 0.60) are discussed.

In Figures 8-12, the radial distribution of flow properties at various flow coefficients are shown. They are compared with those obtained from the Streamline Curvature Method (SCM). In general the agreement is good near design condition, except near the hub and tip, where the flow is dominated by the endwall effects. For IGV exit, the agreement is good even at the hub and tip, indicating the extent of endwall flows is confined to very small distances from the annuli. In the Streamline Curvature Method, the experimental tangential velocity is one of the input. Therefore, no comparison is made for the absolute tangential velocity. The agreement between the experimental and the predicted distribution is fair even for the rotor exit (near design condition) except near the hub and tip. The Streamline Curvature Method used for the comparison with the present data does not consider the blade-to-blade variations and predicts axisymmetric flow only. Therefore, this may be the reason for the discrepancies between the observed and predicted differences in the velocities at some locations.

The radial distribution of the stagnation pressure rise coefficient, the Euler's pressure rise coefficient, the Euler's efficiency and the loss coefficient across the rotor is also shown in Figures 8-12. The observed low efficiencies and large losses in the hub and tip regions clearly show need for the investigation and improvement of the endwall flows in turbomachinery.

The large discrepancies between experimental and predicted flow properties in the endwall regions and the larger extent of the endwall regions at the stator exit indicates the presence of the thicker annulus wall boundary layers due to the large spacing between the rotor and the stator.

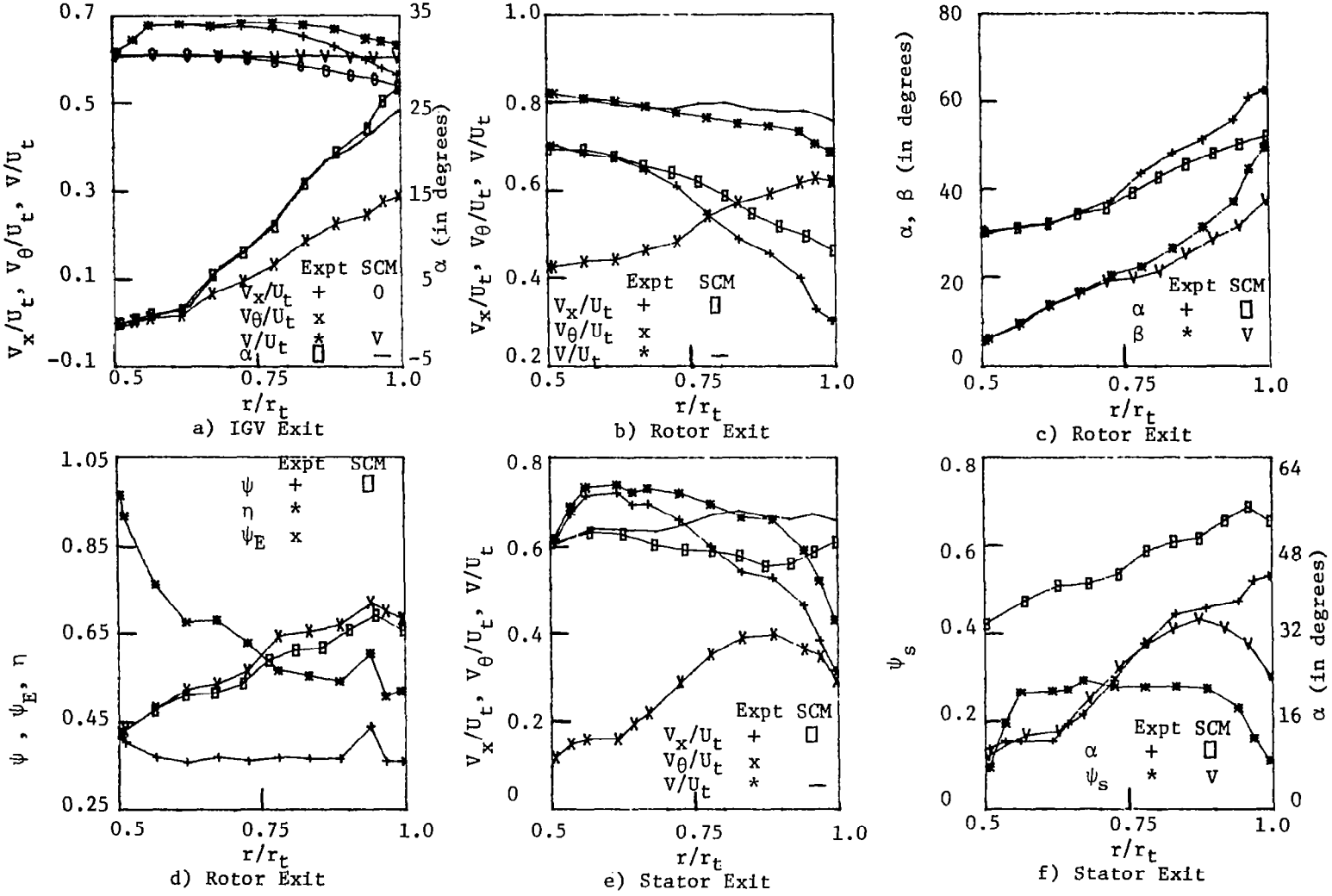

Figure 8. Radial Distribution of Flow Properties at $\bar{\phi}$ = 0.60

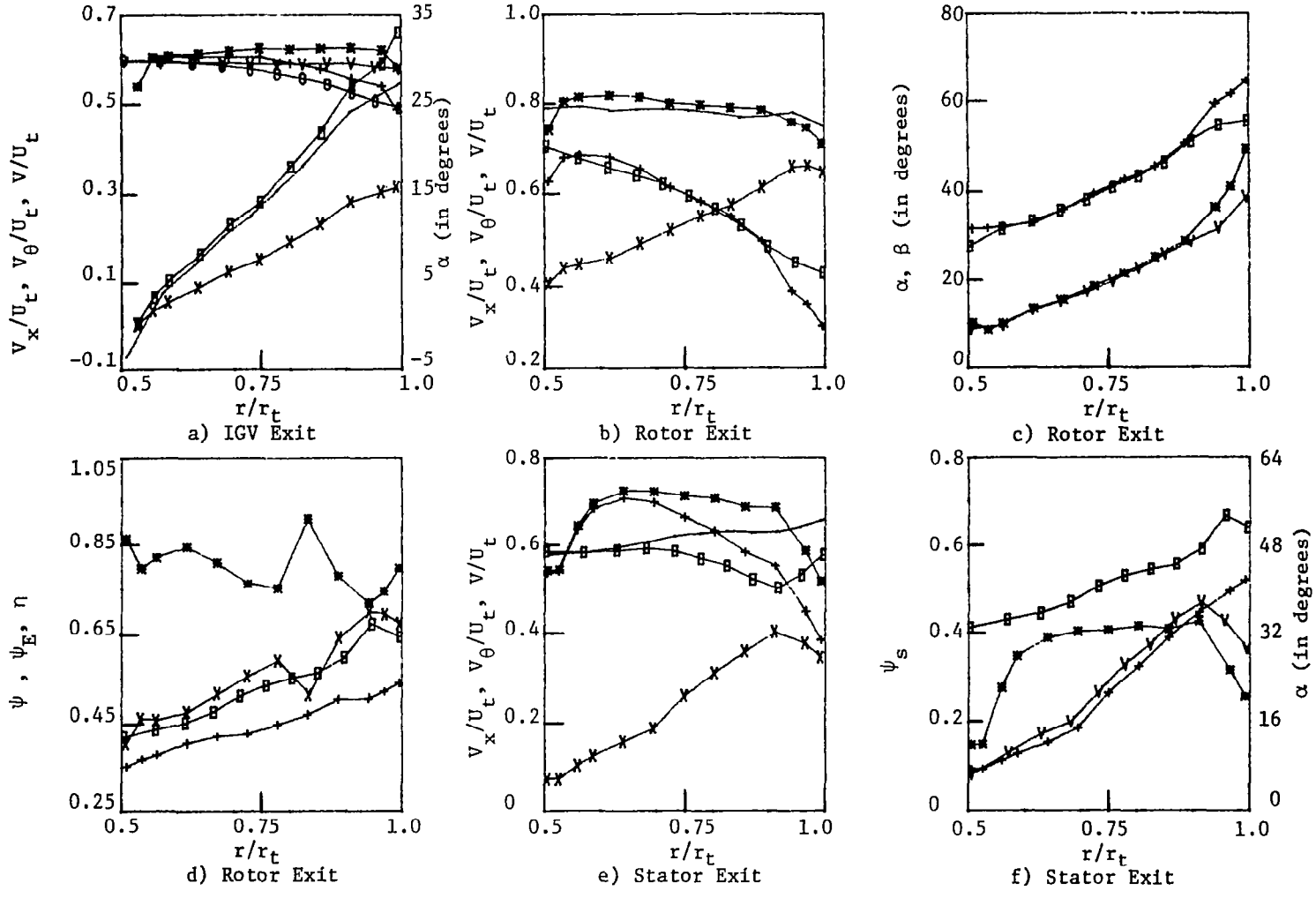

Figure 9. Radial Distribution of Flow Properties at $\bar{\phi}$ = 0.57
(For legend see Figure 8.)

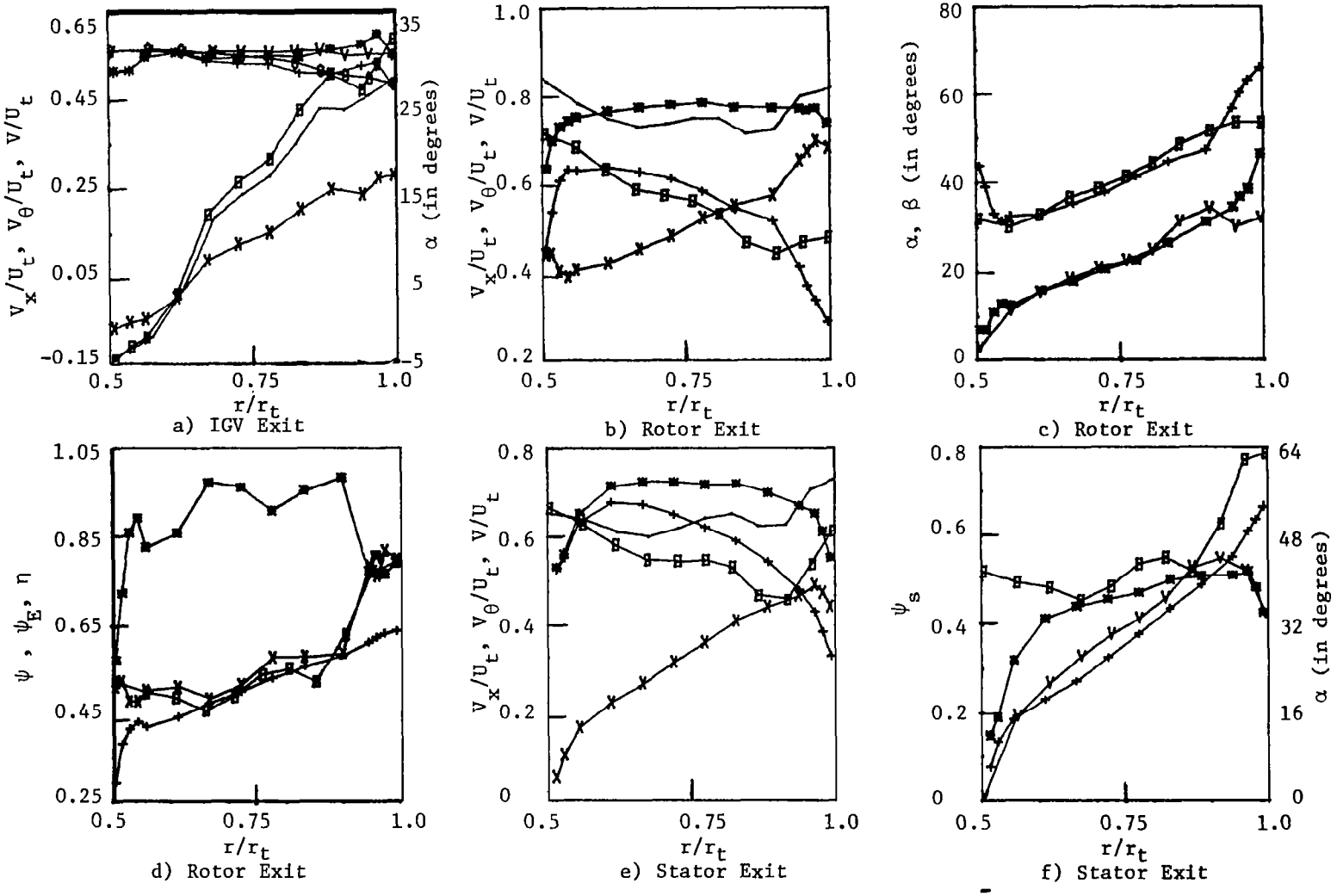

Figure 10. Radial Distribution of Flow Properties at $\bar{\Phi}$ = 0.55
(For legend see Figure 8.)

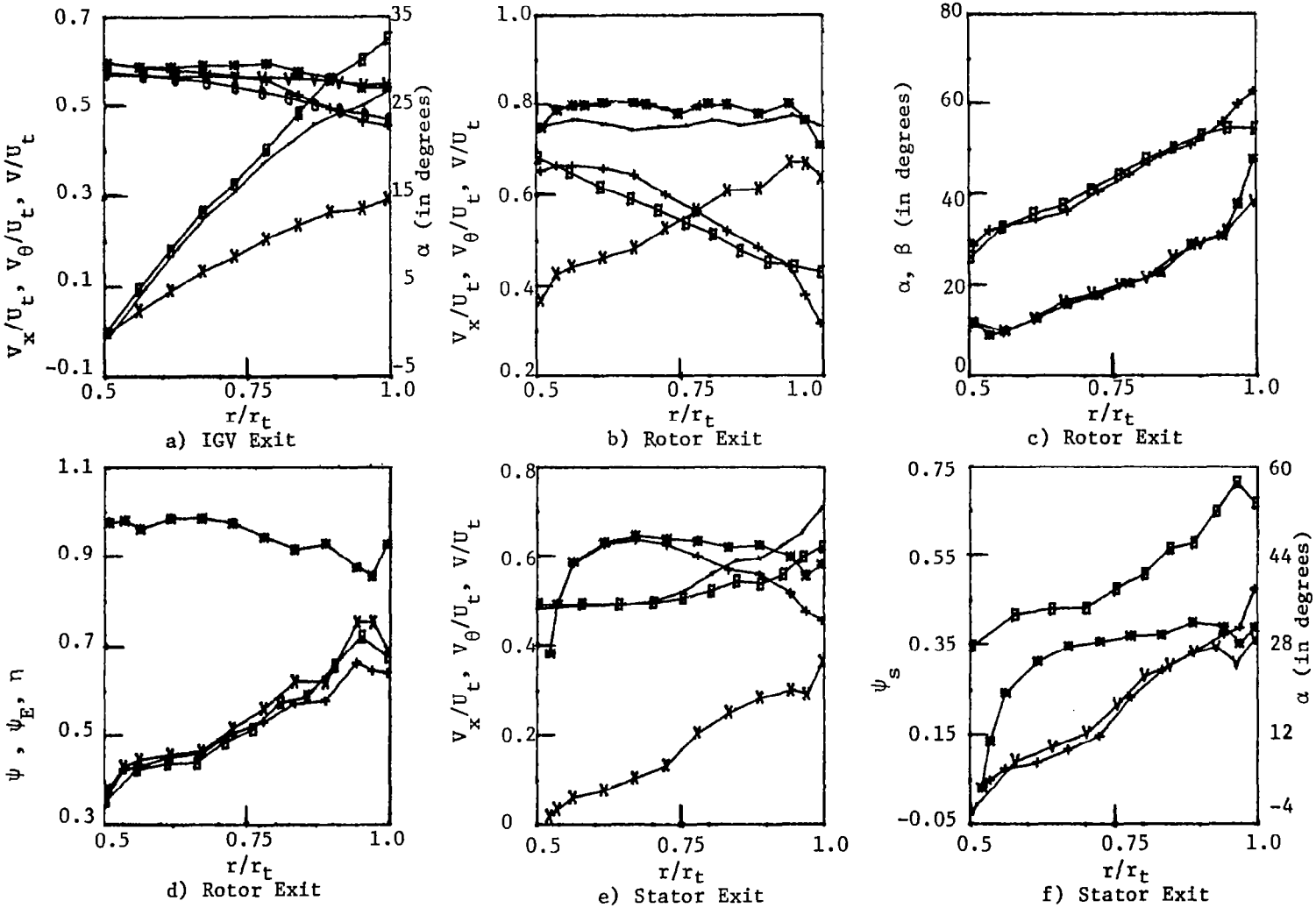

Figure 11. Radial Distribution of Flow Properties at $\bar{\Phi}$ = 0.54
(For legend see Figure 8.)

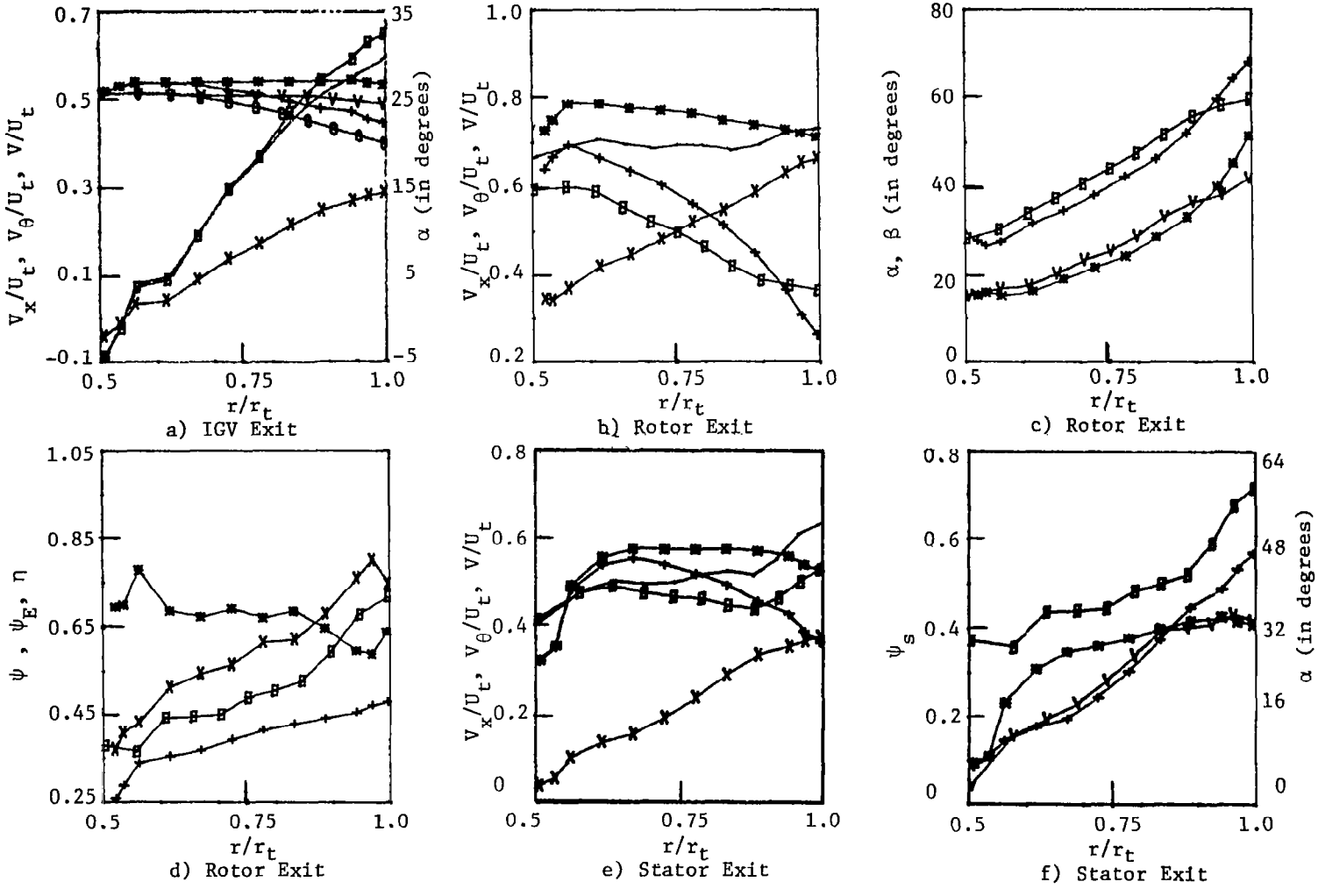

Figure 12. Radial Distribution of Flow Properties at $\bar{\phi}$ = 0.48
(For legend see Figure 8.)

Blade Element Performance

Axial flow compressor blade rows performance can be described by means of blade element parameters, such as equivalent diffusion factor, incidence and deviation angles. These parameters are very useful for comparing the performance of various compressors with different inlet conditions and blade geometry. The blade element performance can be compared with the cascade correlation to discern the three dimensional effects.

The equivalent diffusion factor for the IGV blade at the design flow coefficient of 0.54 is shown in Figure 13. The agreement between all the four cases (present configuration, Smith's configuration, Design and Streamline Curvature Method) is good except near the hub and tip. Similarly, the equivalent diffusion factor for the rotor blade row (Figure 13b) is observed to be in good agreement for all the four cases. The equivalent diffusion factor near the tip is more than 2.0, indicating that the rotor is near stall in this region.

The incidence angle at the design flow coefficient for the rotor and the stator are shown in Figure 14. The incidence angle for the rotor varies from negative values at the hub to positive values at the tip. The incidence angles for the design, present configuration, and Smith's configuration, shown plotted in Figure 14, are in agreement for the rotor and the stator. The values of the incidence angles are within the low-loss incidence range of the corresponding cascade of blade.

Deviation angles for the rotor and the stator at the design flow coefficient are also shown in Figure 14. The agreement between the deviation angles for the design, Smith's configuration, and present configuration is very good. Deviation angles obtained from Carter and Hughes' rule [206] are considerably higher.

Discussion of the Annulus Wall Boundary Layer Characteristics

A brief description of the annulus wall boundary layer characteristics (in terms of axial velocity normalized with the inlet axial velocity) at the exit of all the blade rows at five flow coefficients is discussed here. The data are not sufficient to get a good description of the boundary layer and no attempt is made to derive the boundary layer parameters such as momentum thickness and the displacement thickness.

Radial distribution of axial velocity at the rotor exit is shown in Figure 15. The thickness of the boundary layer is minimum at the design flow coefficient and increases at other flow coefficients. For the stall flow coefficient 0.48, the boundary layer thickness is maximum. Radial distribution of the axial velocities for the IGV and stator is shown in Figure 16. The hub wall boundary layer at the exit of the stator is considerably thick, due to large spacing between rotor and stator blade.

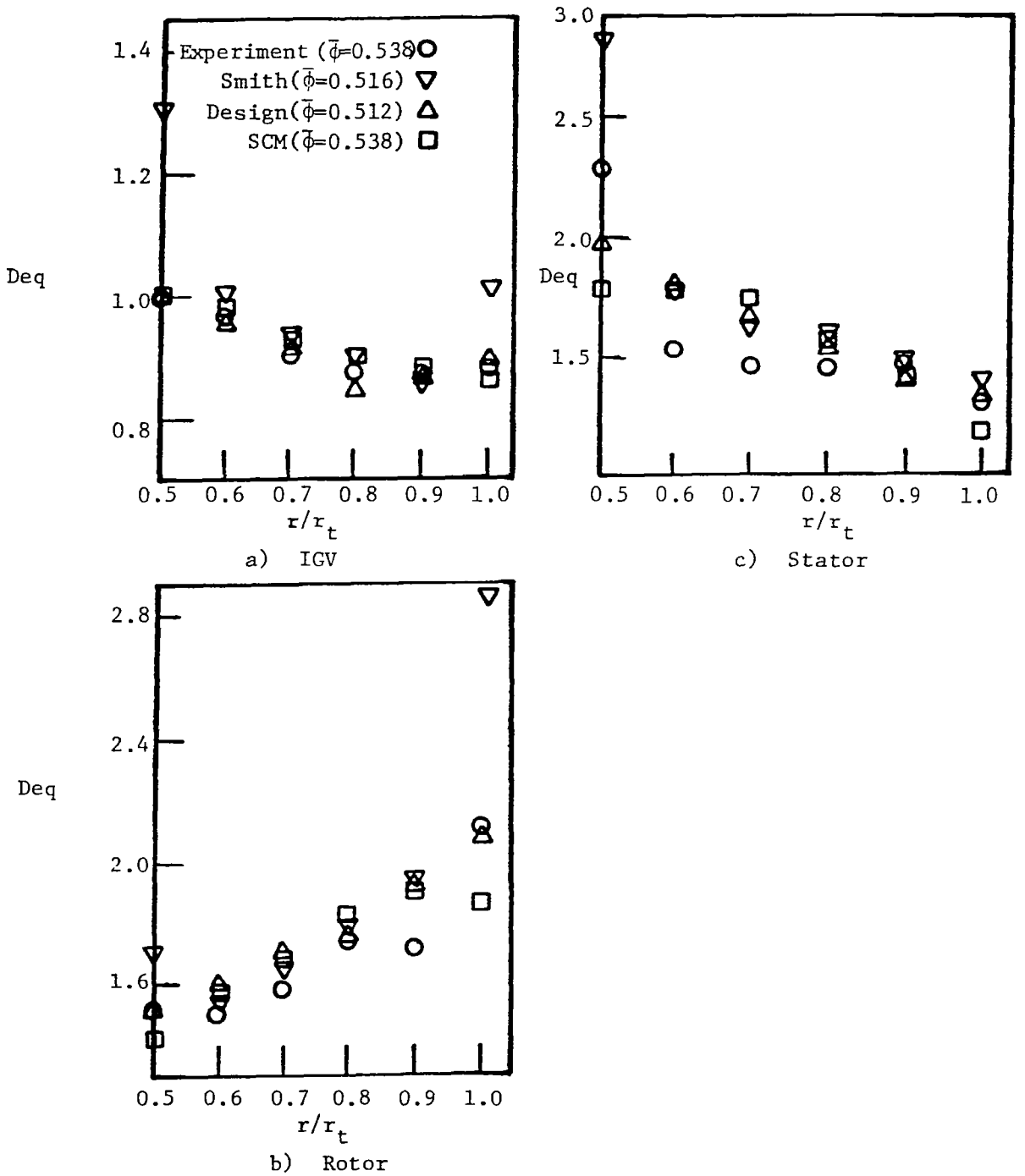

Figure 13. Blade Element Performance: Equivalent Diffusion Factor

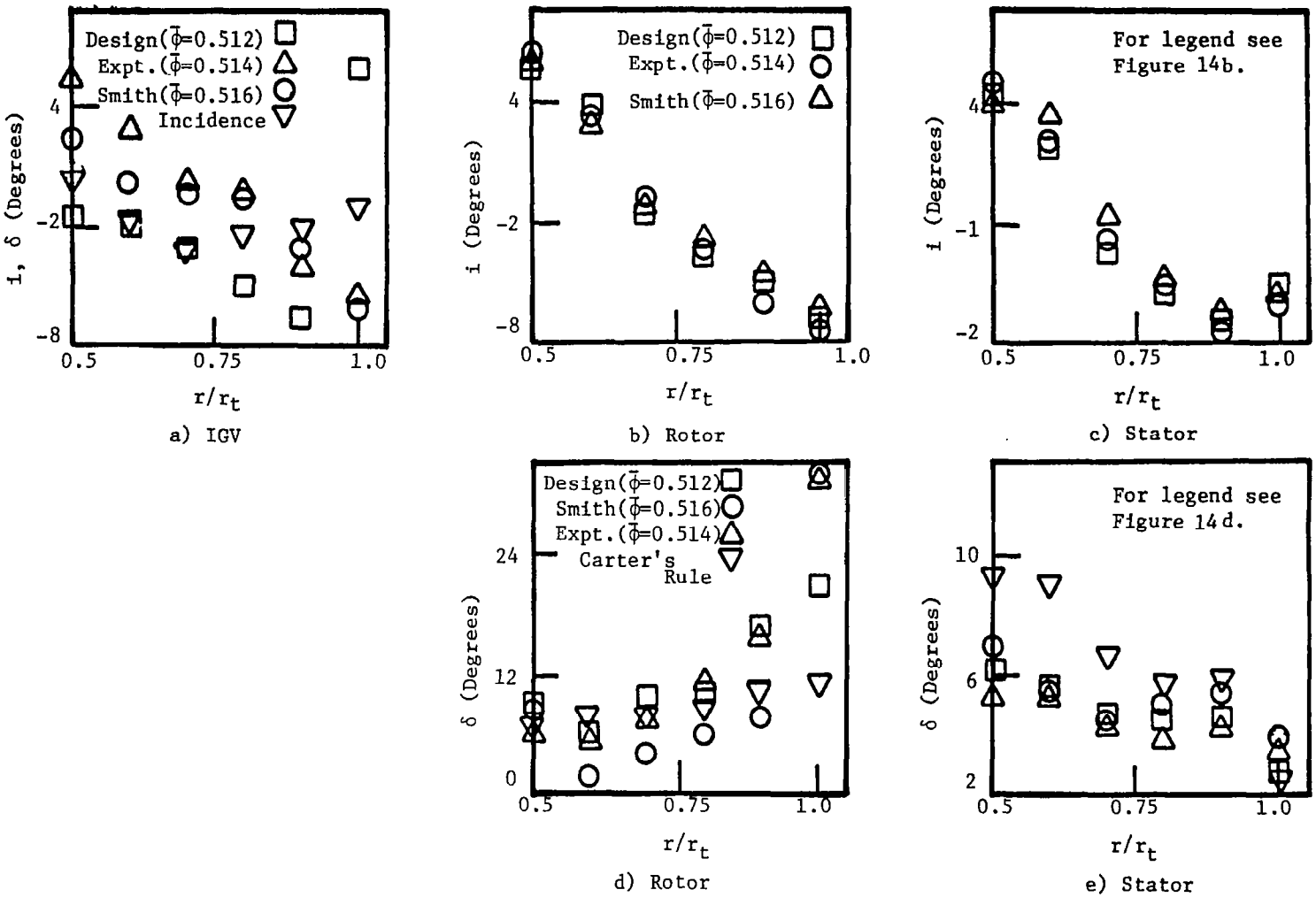

Figure 14. Blade Element Performance: Incidence and Deviation Angles ($\bar{\phi}$ = 0.54)

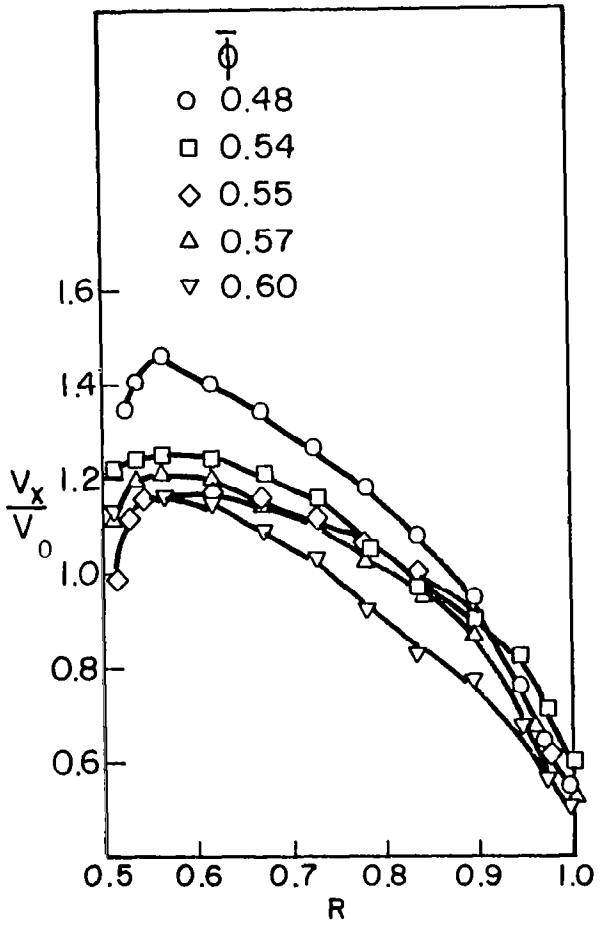

Figure 15. Radial Distribution of Axial Velocity at Rotor Exit

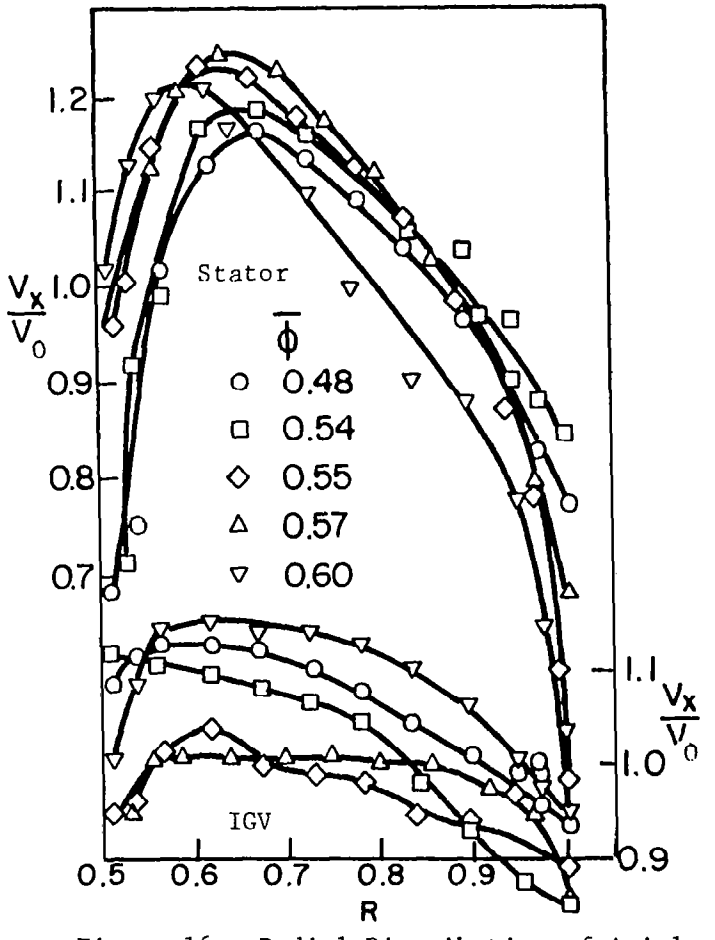

Figure 16. Radial Distribution of Axial Velocity at IGV and Stator Exit

Another interesting parameter in the study of the annulus wall boundary layer is the tangential force defect. Smith in a discussion of Mellor and Wood's paper [9] shows that the tangential force falls off through the end-wall boundary layer. The normalized tangential force defect F_{θ_n} is plotted in Figure 17 for five flow coefficients. F_{θ_n} is defined as

$$F_{\theta_n} = \frac{r}{r_t}\left(\frac{V_{x_2} V_{\theta_2} - V_{x_1} V_{\theta_1}}{U_t^2}\right)$$

Smith [8] in an earlier paper correlated the tangential force defect thickness with the annulus wall boundary layer displacement thickness. For the present tests, no comparison with this correlation is possible because of inadequate data in the annulus wall region.

A dual-sensor TSI hot wire probe was used to measure incoming flow to the rotor in the endwall region. Measurements were taken in very small intervals to determine the annulus wall boundary layer thickness. These measurements were taken at 0.35 chords distance upstream of the rotor leading edge and therefore, should be fairly uniform over the circumference.

The velocity and turbulence intensity profiles in the rotor inlet casing boundary layer are plotted in Figure 18. All these quantities are normalized by the total velocity at the boundary layer edge (U_δ = 30.5 m/sec). The boundary layer edge is characterized by uniform total velocity and sudden decrease in turbulence intensity. The boundary layer edge is at r/r_t = 0.925, giving a fairly thick (35 mm) boundary layer. The unconventional profile is caused by the three dimensionality, probably induced by the secondary flow generated at the IGV exit. The turbulence intensities are quite high near the wall.

Rotor Blade Static Pressure Distribution

The compressor rotor has one fully instrumented passage with static pressure at the following chordwise and radial locations on the suction and pressure surfaces.

Z = 0.083, 0.125, 0.167, 0.25, 0.417, 0.583, 0.75, and 0.833

R = 0.507, 0.587, 0.670, 0.750, 0.832, 0.918, 0.962, 0.988, 0.996, and 0.998.

The static pressure holes are closely spaced near the tip, since the blade static pressure distribution changes rapidly in this region due to the complexity of the endwall flow. The pressure signals from the blade static holes are transmitted through the scanivalve to the rotating pressure transducer of the data transmission system. The rotating pressure transducer electrical signals are transmitted to the stationary instruments (carrier demodulator and voltmeter) through a low noise-to-signal ratio mercury slip ring unit. The scanivalve is controlled by means of a slow-syn preset indexer and the pressures at all the chordwise positions are measured while the compressor is running. While pressure

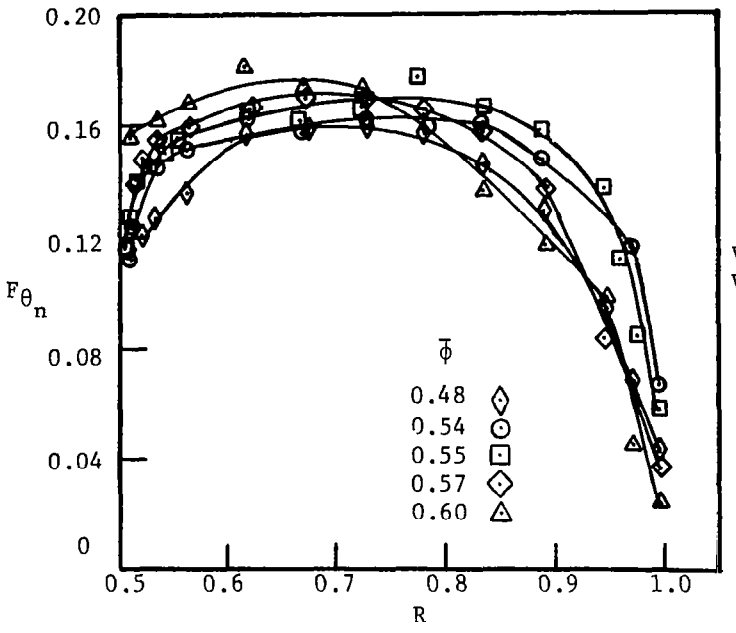

Figure 17. Radial Distribution of Normalized Tangential Force Defect

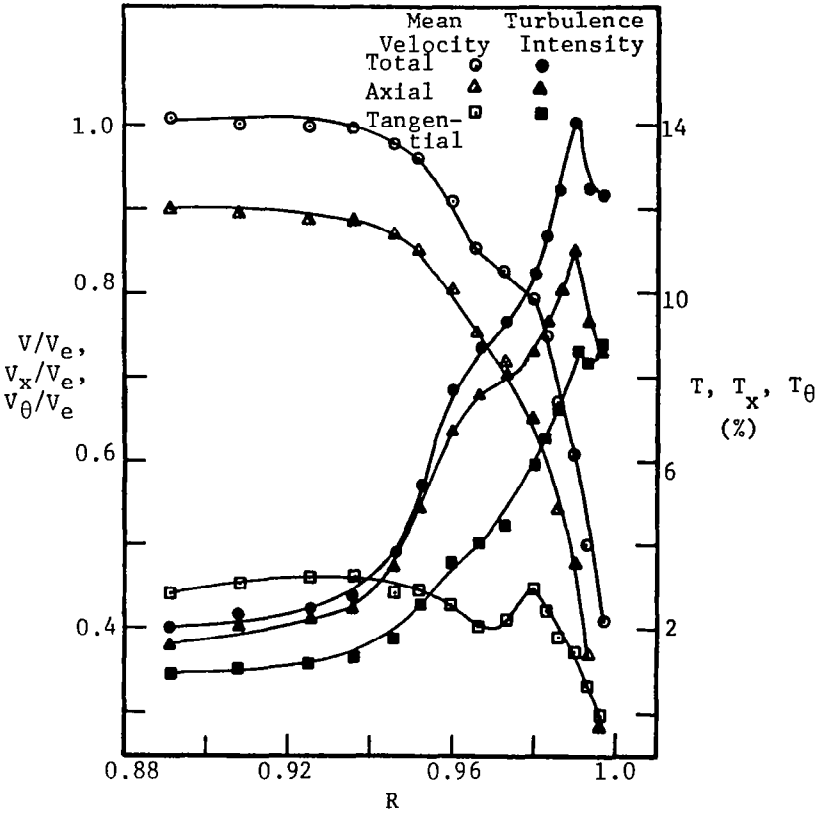

Figure 18. Velocity and Turbulence Profiles at the Rotor Inlet ($\bar{\phi}$ = 0.556)

measurements are being taken at a particular radius the pressure holes at other radii are covered with masking tape. Smoke is blown through the pressure holes to ascertain that there is no leakage between various holes.

Figure 19 shows the chordwise static pressure distribution on the rotor blade at various radial stations (up to $r/r_t = 0.918$) and at various flow coefficients, $\bar{\phi} = 0.54$, 0.55, 0.57, and 0.60 (the flow coefficients are varied by changing the rotor speed). These distributions are compared with those obtained from the Douglas Neumann cascade computer program [199], at flow coefficient of 0.54. The agreement between the theoretical and experimental pressure distribution is good near the mid-radius (R = 0.75). This is to be expected, since at mid-radius the flow is nearly two-dimensional. At other radial stations, the discrepancy between 2-D theory and experiment become more pronounced, deteriorating towards the hub and the tip. At the radial stations very near the hub ($r/r_t = 0.507$, Figure 19), the experimental static pressure distribution is very poor. The pressure holes at this radial station are located very near the hub and are in the hub wall boundary layer. Hence, the flow is affected by the hub wall boundary layer and secondary flow. The blade static pressure distribution at other flow coefficients closely follows the same trends at corresponding radii.

The blade static pressure distribution at various radii near the tip are plotted in Figure 20. No comparison with 2-D theory is made, since the flow here is highly three-dimensional. Decrease in loading as the tip is approached is evident from the figures and this trend is similar to the one observed for a cascade [144]. The suction peak very near the tip occurs beyond the mid-chord, compared to about a quarter chord at other radii.

The lift coefficient (normalized by the inlet dynamic head of relative velocity) derived from these blade static pressure distributions are plotted in Figure 21. These are compared with lift coefficients obtained by Douglas-Neumann cascade inviscid program as well as those derived from the inlet and exit angles using the following equation based on one-dimensional analysis.

$$C_\ell = \frac{2}{\sigma(1 - \delta/2)} \left[\tan\beta_1 - \text{AVR} \quad \tan\beta_2\right] \cos\beta_m - C_D \tan\beta_m$$

where

$$C_D = \frac{\zeta}{\sigma}(1 - \delta/2)\frac{\cos^3\beta_m}{\cos^2\beta_2} - \frac{2}{\sigma}\delta\cos^2\beta_m\left\{[\text{AVR} - \tan\beta_1 + (\text{AVR})\tan\beta_2]\frac{\tan\beta_m}{2} + \left[1 - \frac{1 + \delta/2}{\cos\beta_1}\right]\cos\beta_m\right\}$$

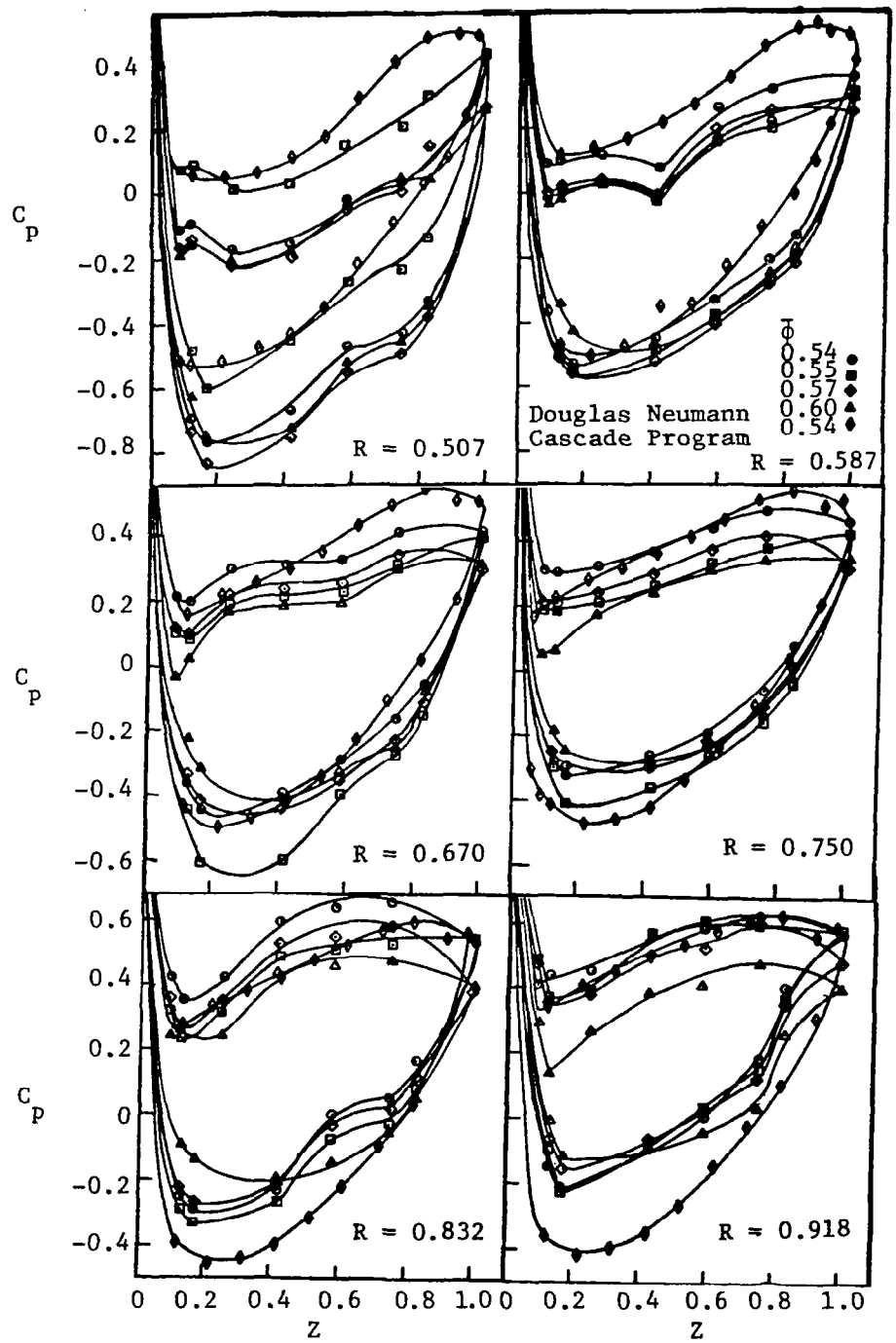

Figure 19. Blade Static Pressure Distribution

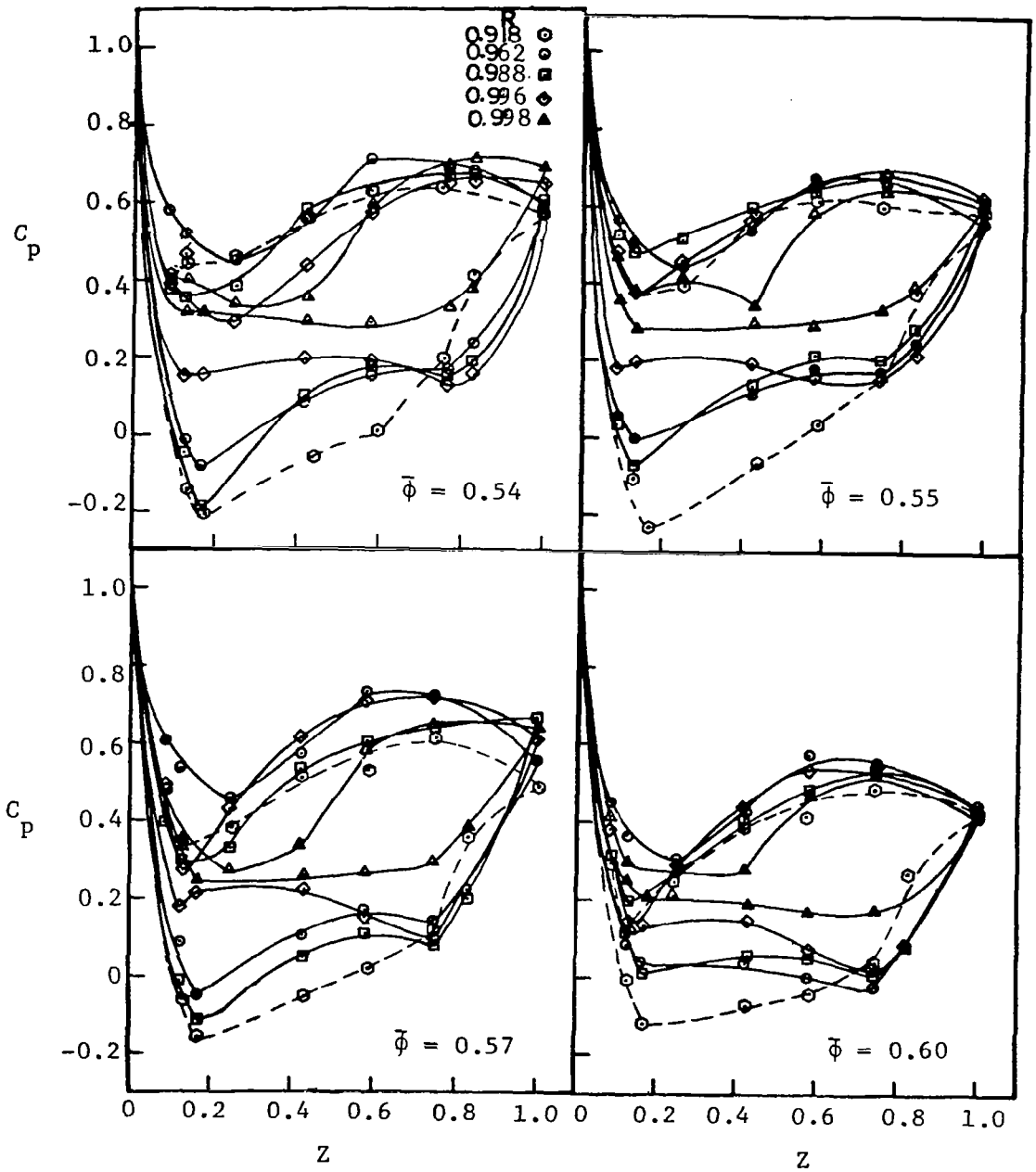

Figure 20. Blade Static Pressure Distribution in the Rotor Blade Tip Region

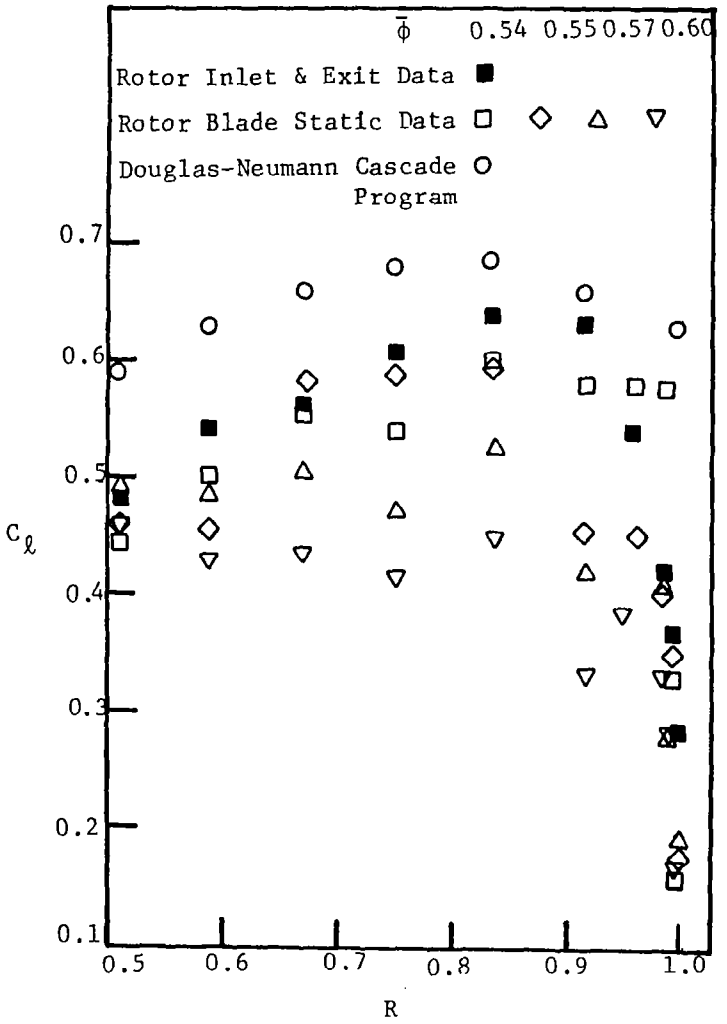

Figure 21. Radial Distribution of Lift Coefficient

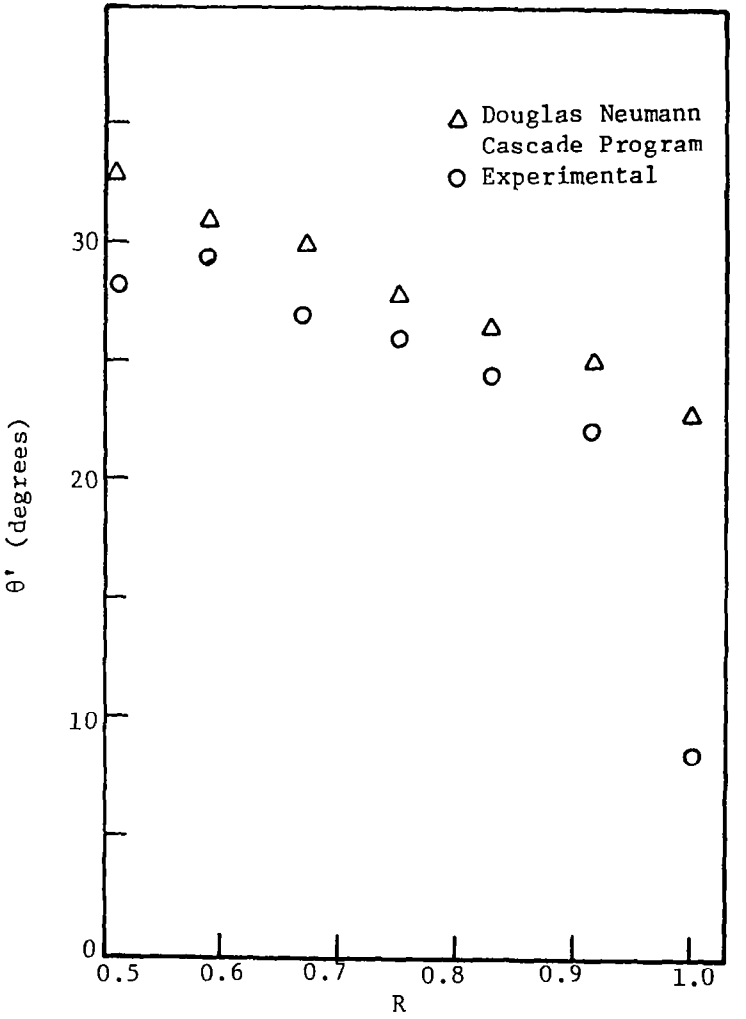

Figure 22. Radial Distribution of Relative Flow Turning Angle ($\bar{\phi}$ = 0.54)

where

σ = average solidity

β_1, β_2, β_m = relative air inlet, exit, and mean angles

δ = 1 - AVR

C_D, C_ℓ = drag and lift coefficients

ζ = loss coefficient based inlet dynamic head of the relative velocity

It is evident from Figure 21 that the lift coefficient decreases drastically towards the tip with large decrease beyond R = 0.918 or outer 20 percent of the span. The gradient of C_ℓ is large for the design (where pressure rise is maximum), even though the C_ℓ value at the tip is almost the same for all the flow coefficients. This indicates the presence of larger leakage flow velocities at the design flow coefficient.

Figure 22 shows the radial distribution of relative flow turning angle obtained experimentally and from the Douglas Neumann cascade program at a flow coefficient of 0.54. The agreement between the two distributions is good except near the hub and tip where the flow can no longer be considered as two-dimensional and inviscid.

Rotor Hub Wall Static Pressures

The rotor hub section, between the blades having the static pressure taps has three metal tubes embedded in it. Static pressure taps are drilled in these tubes at 11 equi-distant axial stations, from leading edge to trailing edge. The tangential locations of these taps are shown in the Figure 23. These taps are used to determine the hub wall static pressures. The measurement technique is very similar to that used for the rotor blade static pressures.

The C_p distribution for the four flow coefficients (ϕ = 0.54, 0.55, 0.57, and 0.60) are shown in Figure 24. Please note that the starting position of Y is from the camber line at that particular axial station. The static pressure at the first axial station (Z = 0) is affected by the relative motion between the stationary hub upstream and rotor. The C_p distribution increases towards the trailing edge, except at Z = 0.1, 0.2, and 0.3. At these axial stations, the C_p distribution coincides or slightly decreases at downstream stations. This indicates that the velocity profile is almost flat between Z = 0.1 to 0.3 and decreases towards the blade trailing edge. The same pattern is observed at all the flow coefficients. The C_p distribution consistently decreases with increasing flow coefficient. This is in accordance with the performance curve of the rotor.

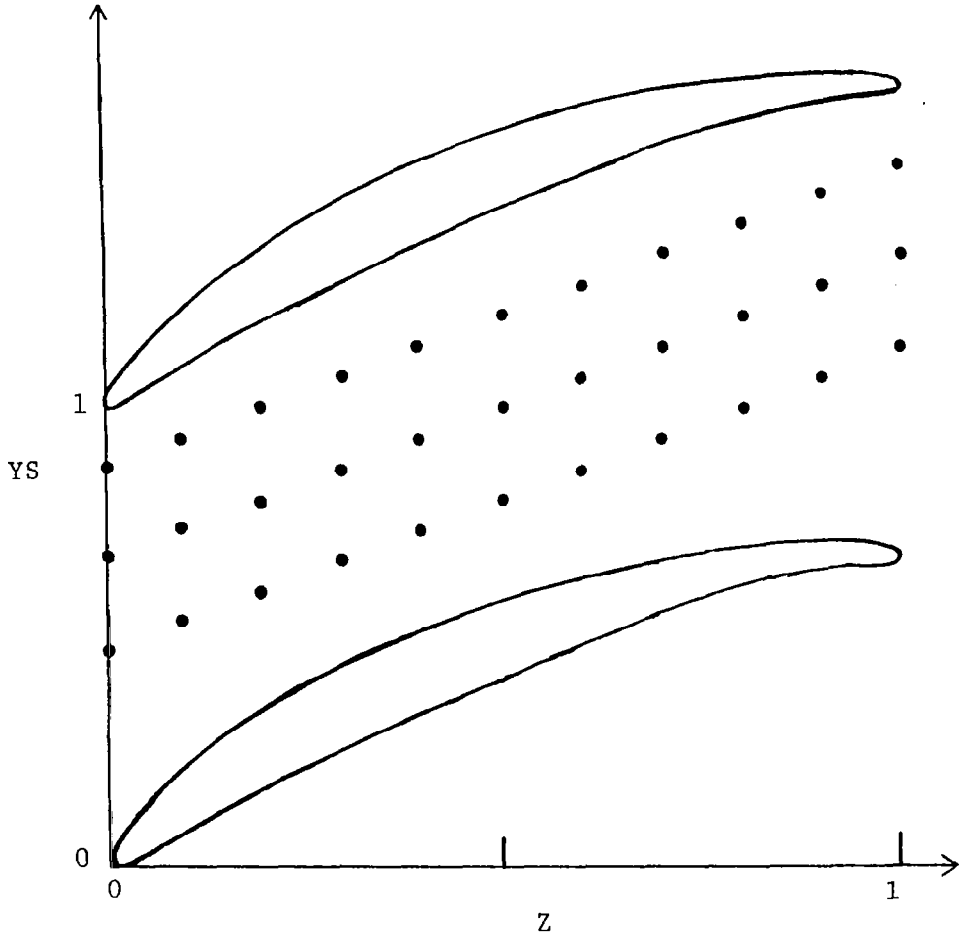

Figure 23. Location of Static Pressure Taps on the Rotor Hub

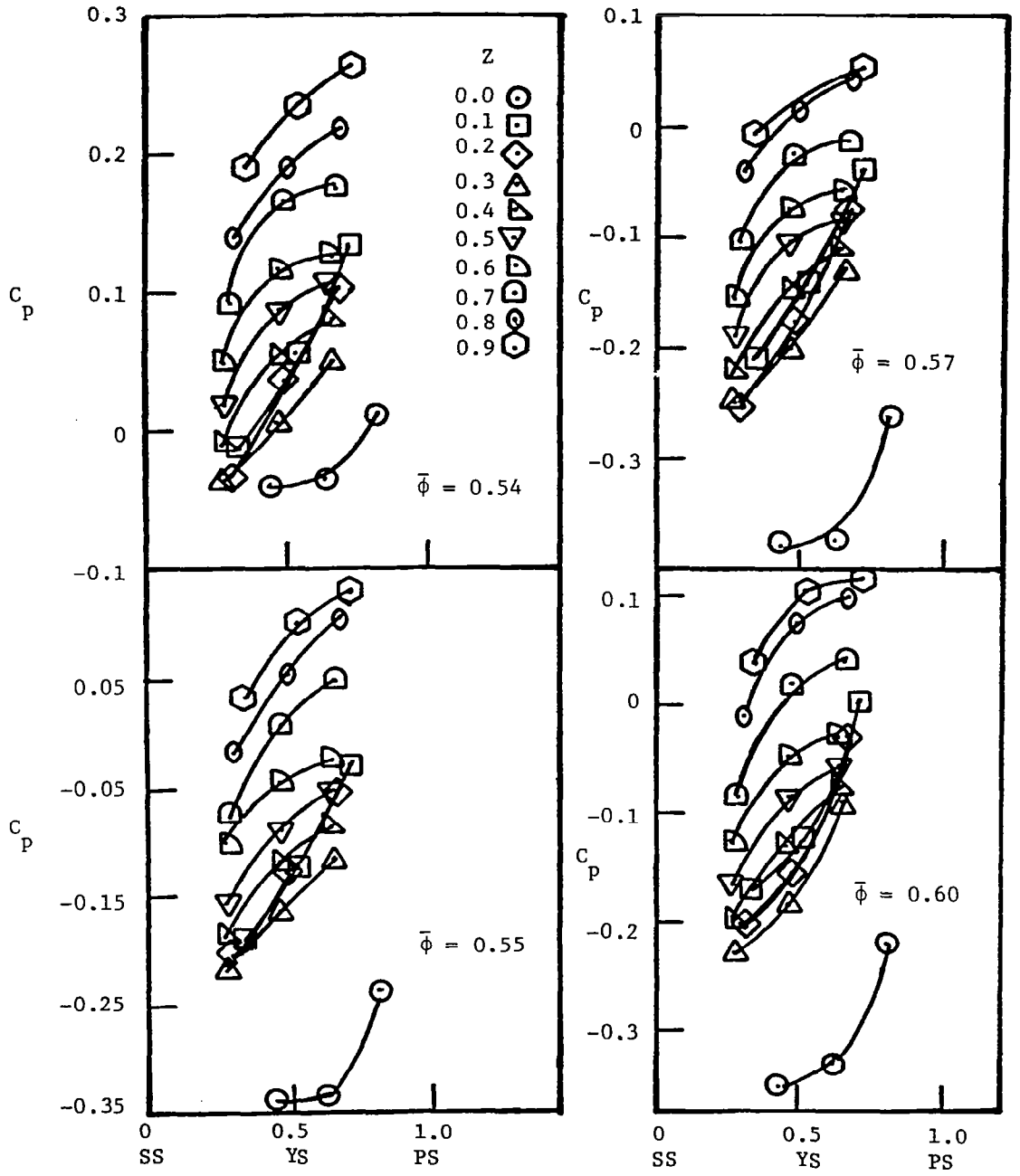

Figure 24. Static Pressure Distribution on the Rotor Hub Wall

IGV ENDWALL FLOW MEASUREMENT

Inlet guide vanes (IGV) are essential for the improvement in the stage efficiency and the operating range of axial flow compressors. A recent study [207] has shown that an appreciable increase of 35 percent in the useful operating range of an axial flow rotor is obtained with freely rotating IGV compared to the rotor without IGV. Very little information is available on the flow field inside the IGV passages. Most of the experimental data available consists of radial survey at the IGV exit with no blade to blade measurement. An exception to this is the investigation by Kolesnikov [208] who made a blade-to-blade survey of the velocity and the pressure fields at an IGV exit. Although detailed flow traverses have been made within linear cascades (both turbines and compressors), this data can not be used in understanding the flow inside the turbomachines blade rows, because of the lack of curvature effects.

The flow enters axially into IGV and is accelerated through the passage. The flow in the endwall region is highly three-dimensional and can not be estimated from the two-dimensional cascade data or theories. The losses in this region are also large, and the flow turning is much more than the design values. These complexities arise due to the development of secondary flows generated due to the turning of the incoming wall boundary layers. Moreover, the incoming flow to the succeeding row (i.e., rotor) would be much more different than the design. Hence, the present investigation is undertaken to understand the endwall flow in an IGV in a real environment. This investigation is a part of the comprehensive investigation being carried out on the blade endwall flows in axial flow compressors in the Turbomachinery Laboratory of the Department of Aerospace Engineering at The Pennsylvania State University.

Facility, Instrumentation, and Technique

The single-stage axial-flow compressor facility at the Turbomachinery Laboratory of the Department of Aerospace Engineering at The Pennsylvania State University is used in the present experimental investigation. A detailed description of the facility is given in an earlier section. The degails of IGV are given in Table V and blade profiles at six radial stations are given in Figure 25. The geometric properties (such as the chord length, stagger angle, thickness/chord ratio) vary along the blade span and the blade profile is NACA 65-010 modified to have a 1 percent chord trailing edge radius.

A five hole probe of 1.65 mm (0.066 in.) diameter is used to measure the IGV endwall flow at various axial and tangential stations shown in Figure 26 and Table VI. The probe is constructed and calibrated at the Garfield Thomas Water Tunnel of The Pennsylvania State University. The calibration and interpolation techniques of Treaster [209] are used.

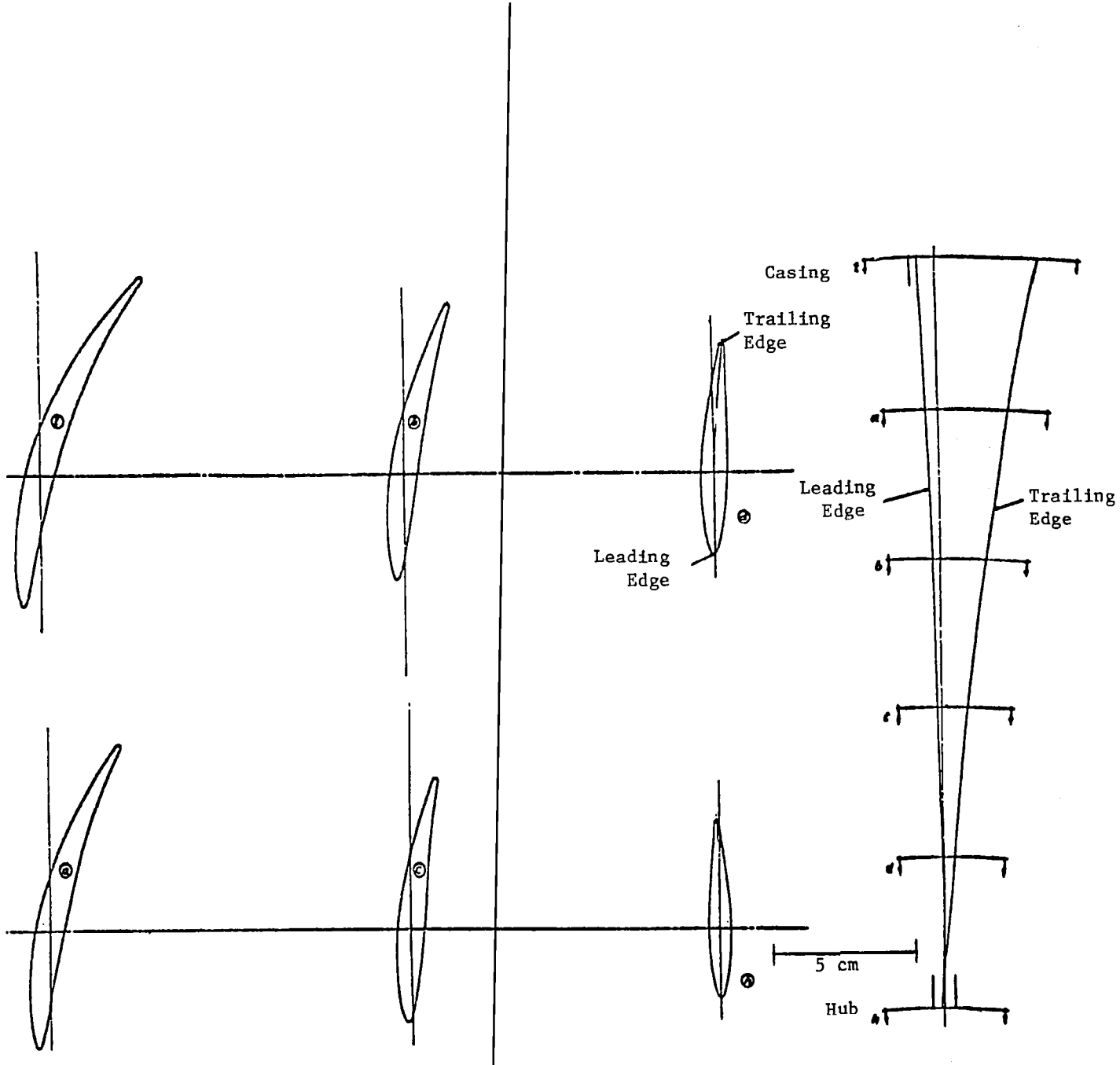

Figure 25. IGV Profiles

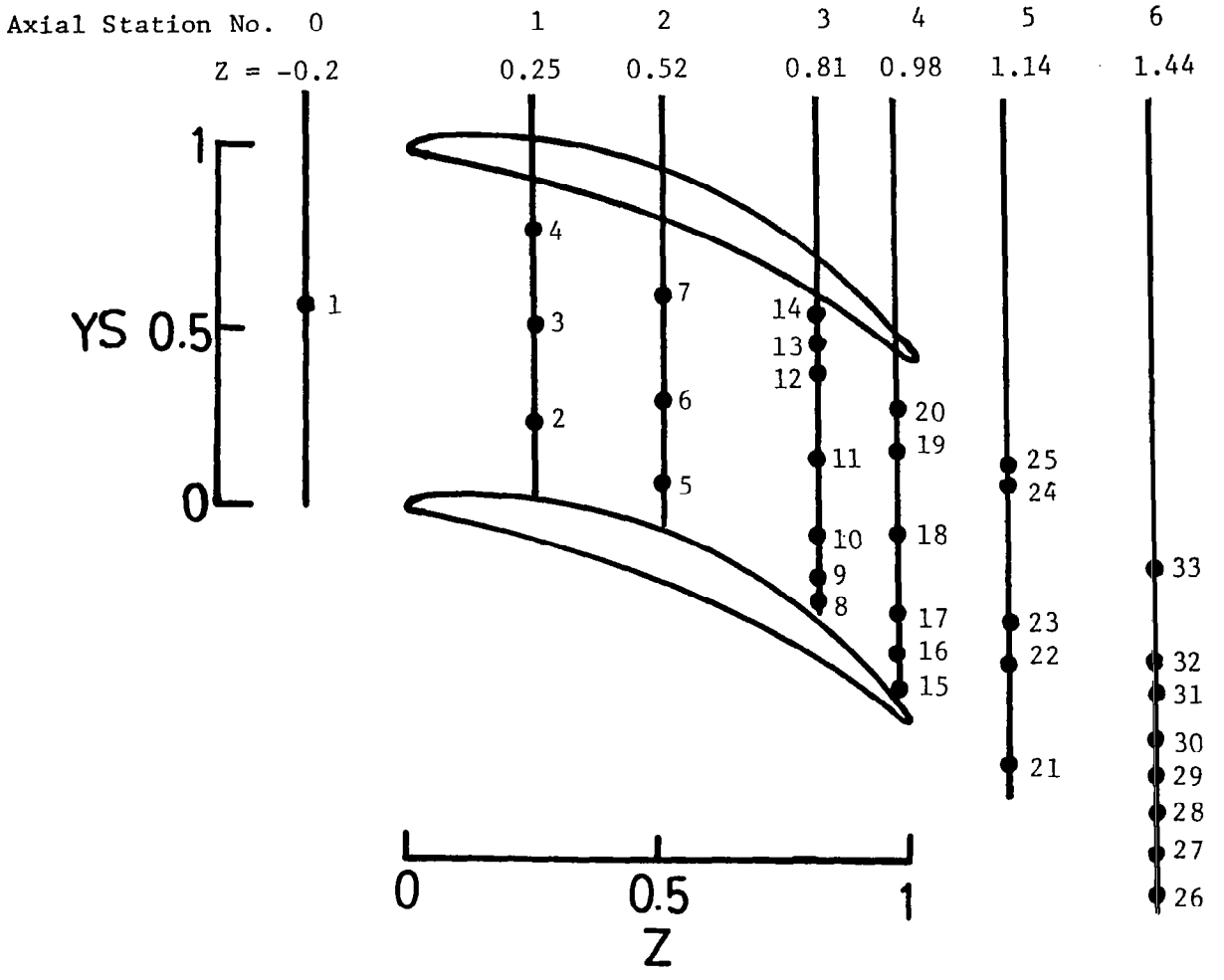

Figure 26. IGV Endwall Flow Measuring Positions

Table VI. IGV Endwall Flow Measurement Stations

Axial Station	Measurement Position No.	X (in)	Z X/C_{t_x}	y (in)	YS y/s_t	Symbol Used in Figure 39
0	1	-0.8	-0.20	3.125	0.53	
1	2	1.015	0.25	2.37	0.287	
1	3	1.015	0.25	3.09	0.543	
1	4	1.015	0.25	3.87	0.821	
2	5	2.111	0.52	1.90	0.231	
2	6	2.111	0.52	2.57	0.469	
2	7	2.111	0.52	3.35	0.747	
3	8	3.289	0.81	1.0	0.133	
3	9	3.289	0.81	1.16	0.190	
3	10	3.289	0.81	1.48	0.304	
3	11	3.289	0.81	2.12	0.532	
3	12	3.289	0.81	2.85	0.791	
3	13	3.289	0.81	3.01	0.848	
3	14	3.289	0.81	3.25	0.930	
4	15	3.938	0.97	0.3	0.062	
4	16	3.938	0.97	0.58	0.162	
4	17	3.938	0.97	0.90	0.276	
4	18	3.938	0.97	1.53	0.500	
4	19	3.938	0.97	2.17	0.727	
4	20	3.938	0.97	2.49	0.841	
5	21	4.872	1.14	-0.27	0.10	
5	22	4.872	1.14	0.53	0.392	
5	23	4.872	1.14	0.85	0.500	
5	24	4.872	1.14	1.92	0.878	
5	25	4.872	1.14	2.08	0.936	
6	26	6.09	1.44	-1.25	0.09	
6	27	6.09	1.44	-0.93	0.208	
6	28	6.09	1.44	-0.61	0.300	
6	29	6.09	1.44	-0.30	0.427	
6	30	6.09	1.44	-0.03	0.523	
6	31	6.09	1.44	0.34	0.654	
6	32	6.09	1.44	0.58	0.74	
6	33	6.09	1.44	1.30	0.95	

A schematic of the probe and its calibration is shown in Figures 27 and 28, respectively. This probe is selected because of its small dimensions, which will enable accurate measurement of the thin wall boundary layers at the inlet and inside the IGV passages. The five tubes of the probe are connected to a scanivalve. The output of the scanivalve is measured by ±0.2 psi range Validyne DP-15 pressure transducer. The transducer is connected to the Validyne carrier demodulator CD-15, whose output is measured by a voltmeter. The scanivalve is powered and controlled by a control circuit. The speed of the compressor is measured by a photo cell arrangement and can be controlled to an accuracy of ±1 rpm (approximately 0.1 percent). Day-to-day variation of atmospheric pressure and temperature are noted and are used to correct the measured pressures of the five-hole probe.

The axial and tangential movement of the probe is achieved by a simple tangential traverse mechanism. Axial traverse slots enabled small axial movements of the traverse mechanism. The tangential movement is achieved by means of rollers moving in a slotted arc in the traverse mechanism. The traverse mechanism is capable of 0.05 degree movement in the tangential direction. The probe is mounted in a radial traverse mechanism which is capable moving the probe in 0.025 mm (0.001 in.) steps. The probe orientation with the axial direction is measured by means of a protractor mounted on the radial traverse mechanism and is capable of measuring to an accuracy of 0.5 degrees.

The probe is passed through the holes drilled in the casing. The gap between the 6.35 mm diameter holes and 3.43 mm diameter probe stem is filled with a steel tube of proper dimension. The steel tube is almost flush with inner casing. This arrangement made the positioning of the probe from one measurement hole to another possible without stopping the compressor. To measure the probe orientation, the probe is nulled in the freestream region of IGV inlet and its orientation is marked from the protractor. At every measurement position, the probe is aligned in the free-stream region at that passage location and its orientation is noted on the protractor. The difference between these two readings give the free-stream yaw angle. The flow angles inside wall boundary layers are determined likewise. The pitch angle derived from the probe measurements is the radial angle, since the probe is in the radial direction. At axial stations, 3 to 6 (Figure 26), a window with tangential slots is used for probe traversing to enable flexibility in tangential traverses. The gap between the probe and slot is filled up with a dense foam, which is contoured to the window (hence casing) inner curvature. This arrangement is quite satisfactory and there is no leakage or flow disturbance due to the foam. The small gap between the blade and the window are filled with epoxy.

The estimated experimental accuracies are as follows:

Axial and tangential positions of the probe:	0.8 mm (1/32 in.)
Radial position of the probe:	0.025 mm (0.001 in.)
Radial and tangential angles:	±0.5°
RPM of the compressor:	±1 rpm
Static and stagnation pressures:	2% of dynamic head based on tip speed
Limiting streamline angles:	1°

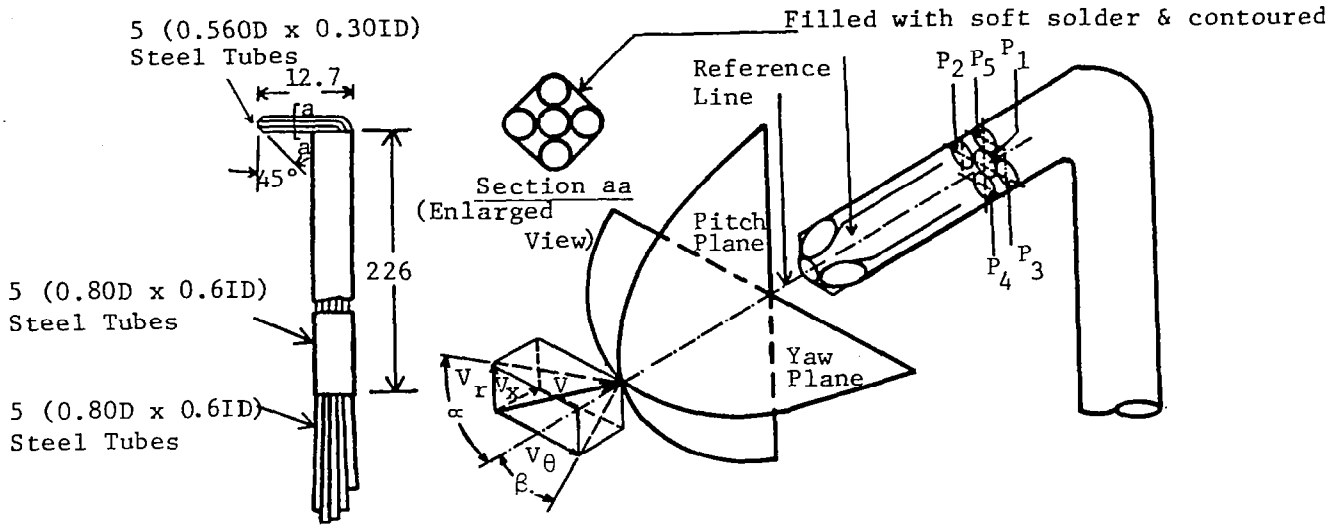

(All dimensions are in millimeters)

Figure 27. IGV Endwall Flow Five-Hole Probe and Its Method of Velocity Vector Resolution

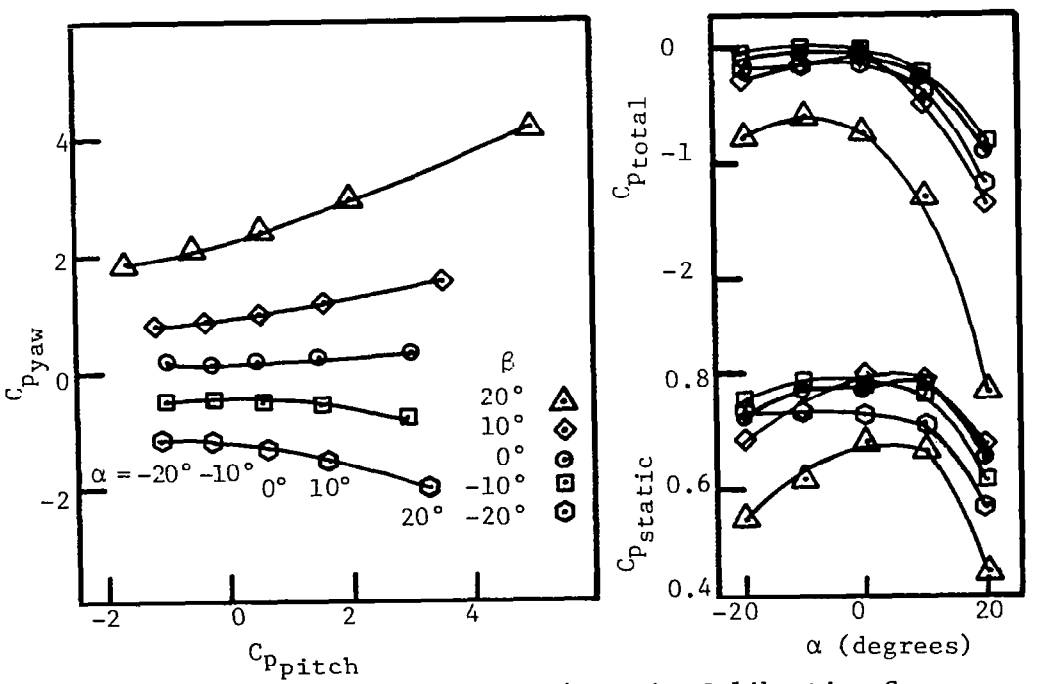

Figure 28. IGV Endwall Flow Five Hole Probe Calibration Curves

The above mentioned accuracy for the radial (meridional) and tangential (yaw) angles and pressures are valid only in the region two probe diameters (3.3 mm) away from the casing wall. In the region very close to the wall, the wall vicinity affects the probe readings drastically and accuracy is poor.

Experimental Results

Limiting Streamline Angles and Wall Static Pressures

The traces of the limiting streamlines are obtained by passing ammonia gas at a controlled rate on to an ozalid paper fixed to the casing blade passage and at the exit. Large number of 1.5 mm diameter holes were drilled on the casing and these are used to pass ammonia. The limiting streamline angle distribution derived from these traces are shown in Figure 29. Even though the inlet wall boundary layer is thin and the flow turning is small, the flow deviates considerably from the blade surface. It is seen from Figure 29 that the flow enters axially. The deviation from the blade surface is small near the leading edge. Beyond an axial position of 0.25 chord downstream the leading edge, the flow deviations are strong, with the flow turning more towards the suction surface. This is to be expected as the cross wise pressure gradients are large starting at Z = 0.25 and up to the trailing edge (see Figure 30). Flow separation near the suction surface is observed to start at Z = 0.81. This separated region continues up to Z = 1.09. Flow reorganizes beyond Z = 1.09 and is almost uniform near Z = 1.5.

The holes that were used for the limiting streamline angles measurements were utilized to measure the static pressures on the casing in the IGV blade passage and at the exit region. The C_p distribution thus obtained is shown in Figure 30. C_p is defined as follows:

$$C_p = 2(p_\ell - p_1)/\rho V_{x_{1_e}}^2$$

The inlet C_p is uniform and zero. Large cross-wise pressure gradients exist inside the IGV blade passage. Suction peak is observed near Z = 0.25. The static pressure gradients in the tangential direction are smaller near the trailing edge. The cross-wise pressure gradients are negligibly small beyond the trailing edge. The streamwise pressure gradient increases towards the trailing edge. On the whole, the C_p distribution seems very similar to that in an inviscid flow.

Boundary Layer Profiles

The annulus wall boundary layer profiles at all the 33 measurement positions are given in Figure 31. The velocity components in s and n directions are defined as follows:

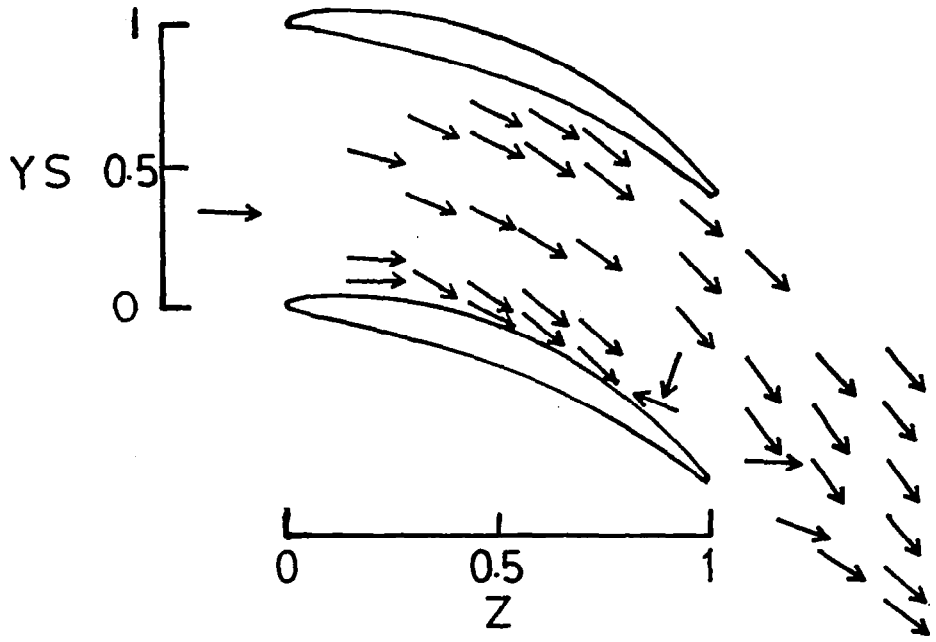

Figure 29. Limiting Streamline Angle Distribution on the IGV Endwall ($\bar{\phi}$ = 0.556)

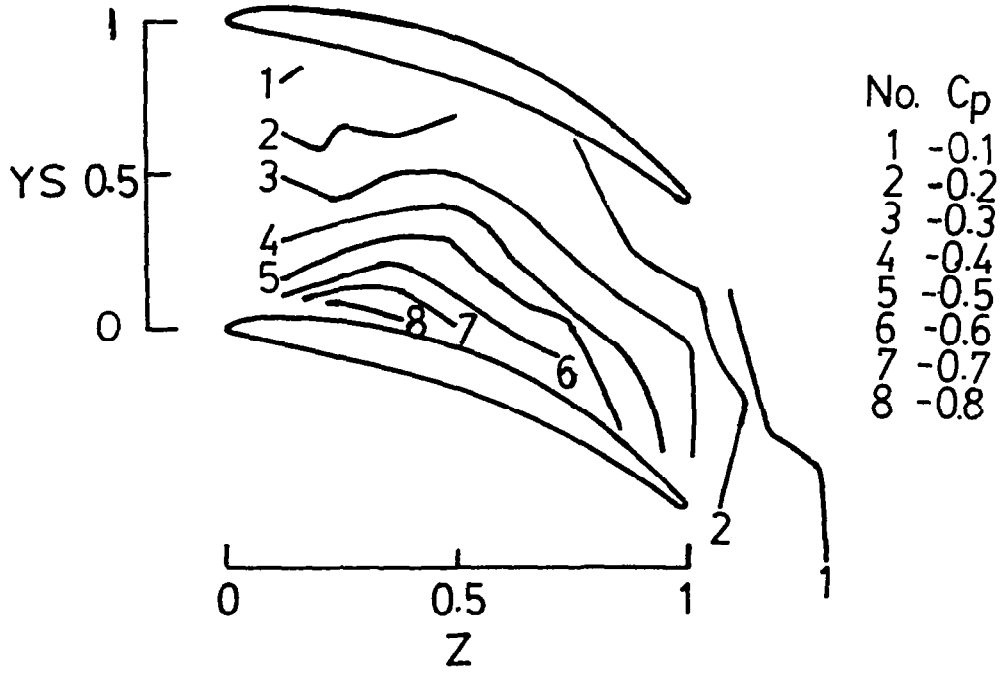

Figure 30. Static Pressure Distribution on the IGV Endwall ($\bar{\phi}$ = 0.556)

$$V_s = V\cos(\alpha - \alpha_e)$$

$$V_n = V\sin(\alpha - \alpha_e)$$

where β_e is the flow angle at the edge of the boundary layer. The edge of the annulus wall is determined from the location where the changes in stagnation pressure, total velocity and flow angle are small. This method proved to be satisfactory and the accuracy is 1.65 mm (i.e., the radial step size towards the boundary layer edge).

It can be observed from Figure 25 that the IGV has considerable twist, sweep and dihedral. Hence, the probe traverses, which are in radial direction, are not along stream surfaces. However, it was felt that the boundary layer development does not vary much from stream surface to stream surface and the radial traverses are used to plot endwall flow boundary layer in the radial direction. This assumption is not valid in measurements close to the blades and in the wakes. However, very few measurements are taken in these regions.

The boundary layer is quite thin, about 6 mm at IGV inlet (Figure 31a) to 12 mm at an axial station 0.44 chords downstream of IGV trailing edge. The inlet boundary layer is collateral. Almost all boundary layers are turbulent. A few separated profiles are observed, near the suction surface towards the blade trailing edge. This is consistent with the endwall limiting streamline angle distribution.

At Z = 0.25 and the tangential locations 2 to 4 (see Figure 26), the boundary layer towards the suction surface (position 2) is collateral (Figure 31b). Towards the pressure surface (station 4), the cross flows increase. The boundary layer thickness is constant across the blade passage. Near mid-chord at Z = 0.52 (Figure 31c), the boundary layer thickness and the cross flows increase towards the pressure surface. The boundary layer is thicker than that at Z = 0.25. The maximum cross flow velocity, as high as 50 percent of the streamwise velocity, occur near the pressure surface. At Z = 0.81 (Figure 31d), the boundary layers are in general thicker than those at Z = 0.52. The boundary layer thickness and cross flows increase towards the mid passage and then decrease towards the pressure surface. This trend, observed for the first time, is due to more extensive measurements (seven tangential locations) at this axial station. The boundary layer is thick near the mid-passage.

Data near the trailing edge at Z = 0.98 (tangential stations 15 through 20), shown in Figure 31e, indicate that the boundary layers are thicker than those at Z = 0.81. The cross flows are considerably larger than those at other axial stations. The trend in the cross flows observed earlier (Z = 0.25 to 0.81), namely smaller cross flows towards suction surface and larger cross flows towards the pressure surface, is reversed at this station. The cross flows are generally higher near suction surface, with maximum values reaching about 100 percent of the local streamwise velocity. The boundary layer thickness is maximum near the suction surface and decreases toward the pressure surface. The boundary layer seem to grow rapidly near the pressure surface as the flow travels from Z = 0.98 to downstream (Z = 1.14), shown in Figure 31f. The boundary layer thickness near the suction surface shows a tendency to decrease.

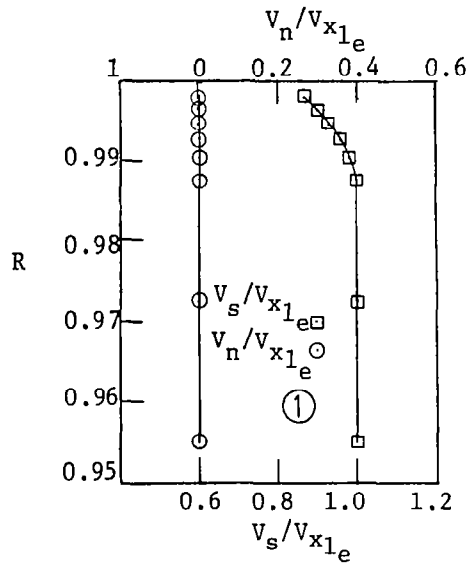

Fig. 31a Z = -0.2

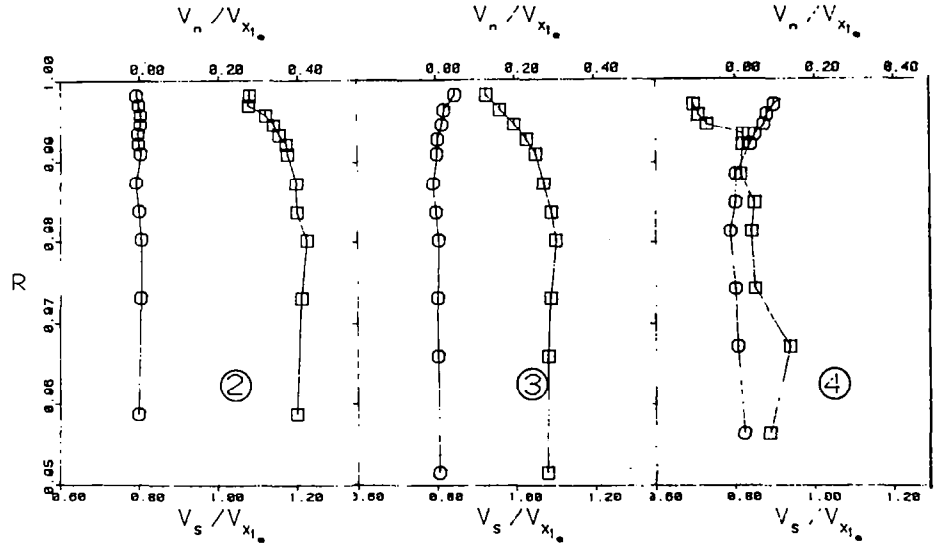

Fig. 31b Z = 0.25

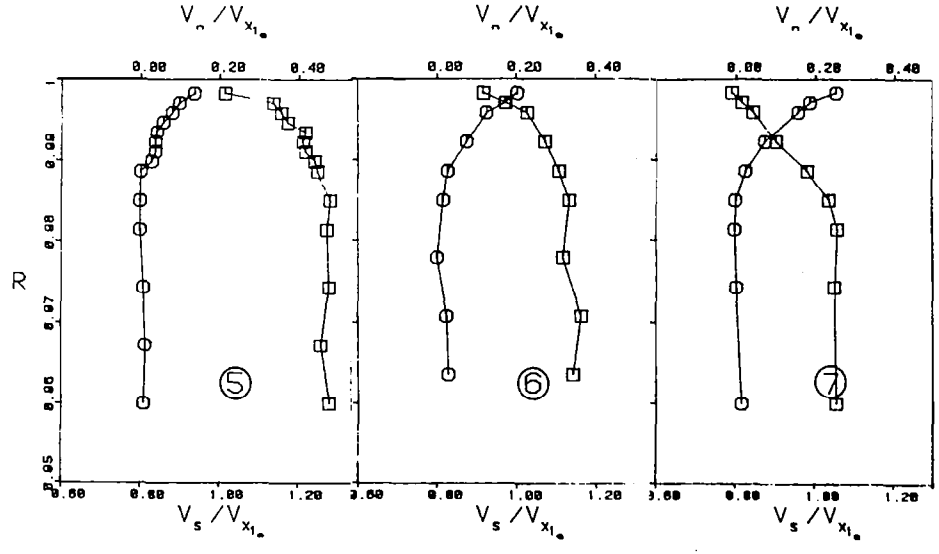

Fig. 31c Z = 0.52

Figure 31. IGV Endwall Flow - Velocity Profiles

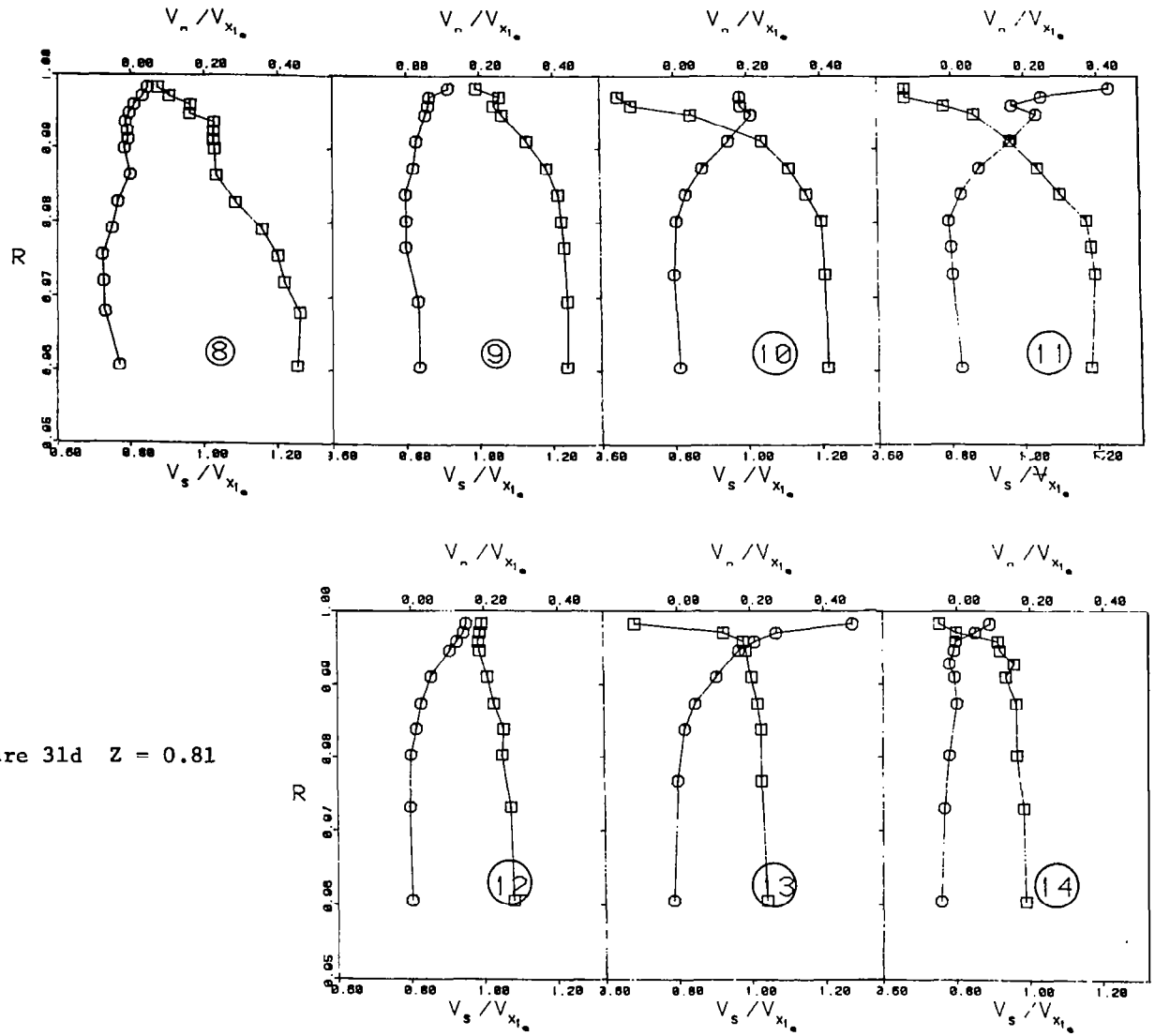

Figure 31d Z = 0.81

Figure 31. (Continued)

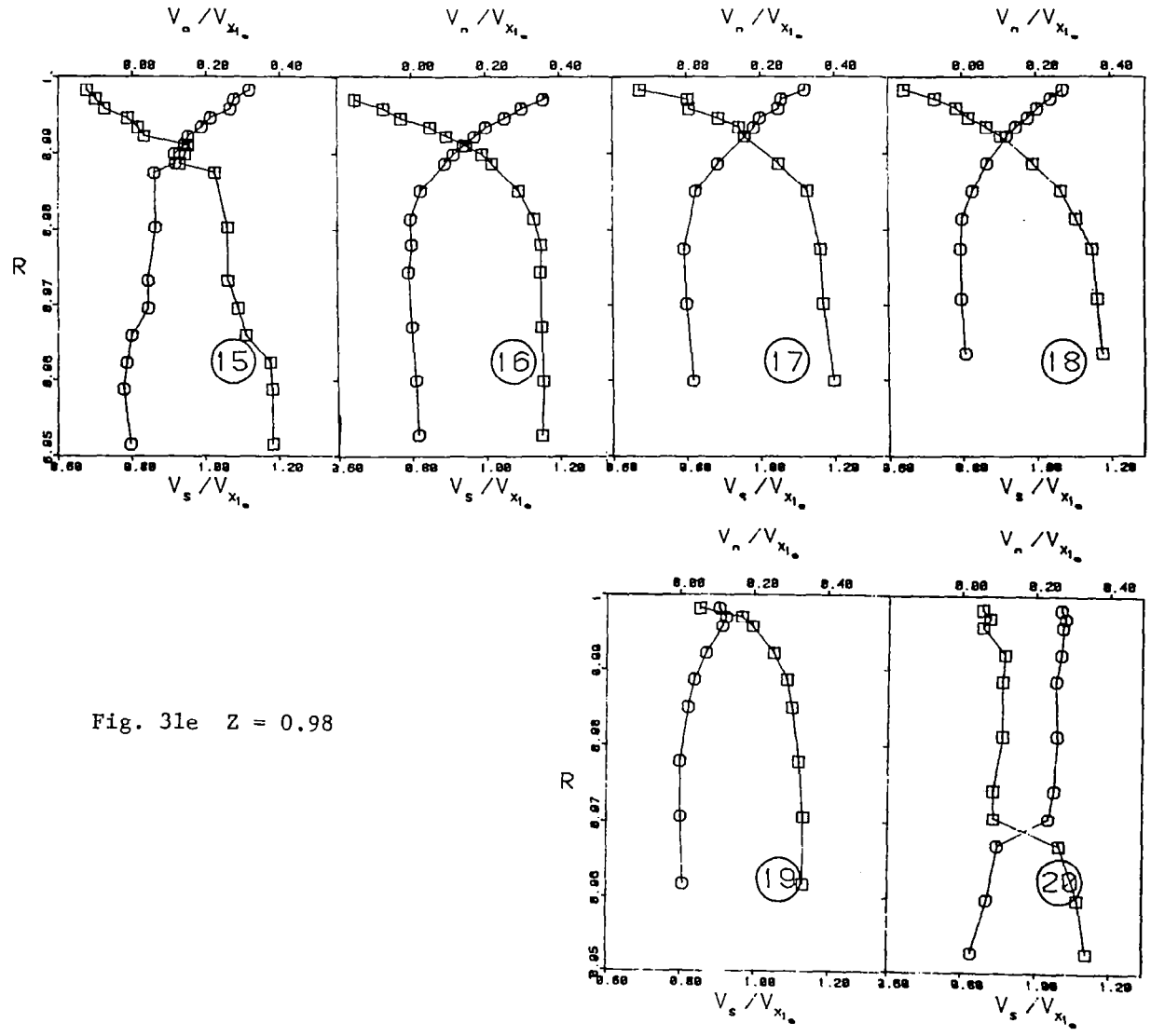

Fig. 31e Z = 0.98

Figure 31. (Continued)

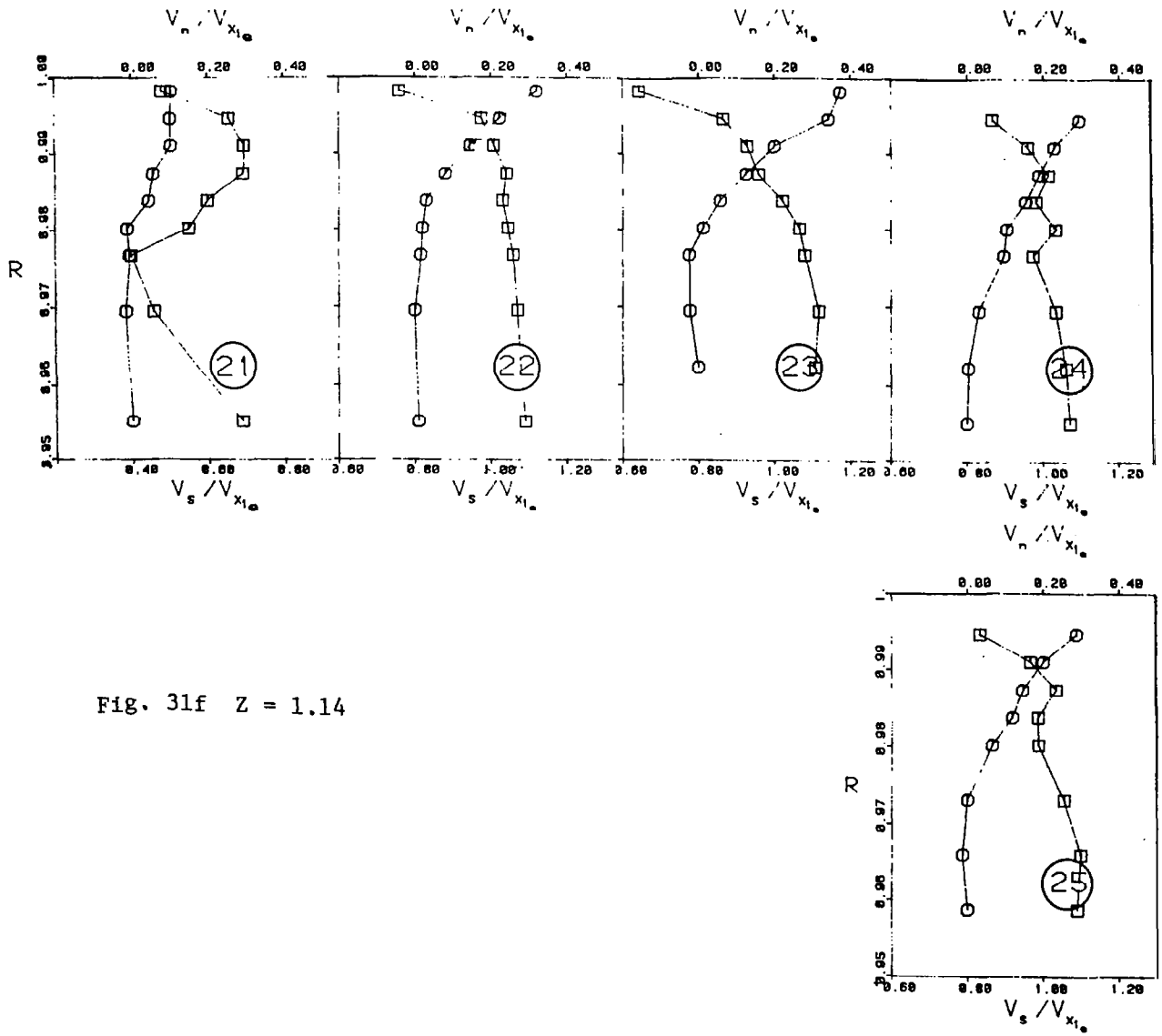

Fig. 31f Z = 1.14

Figure 31. (Continued)

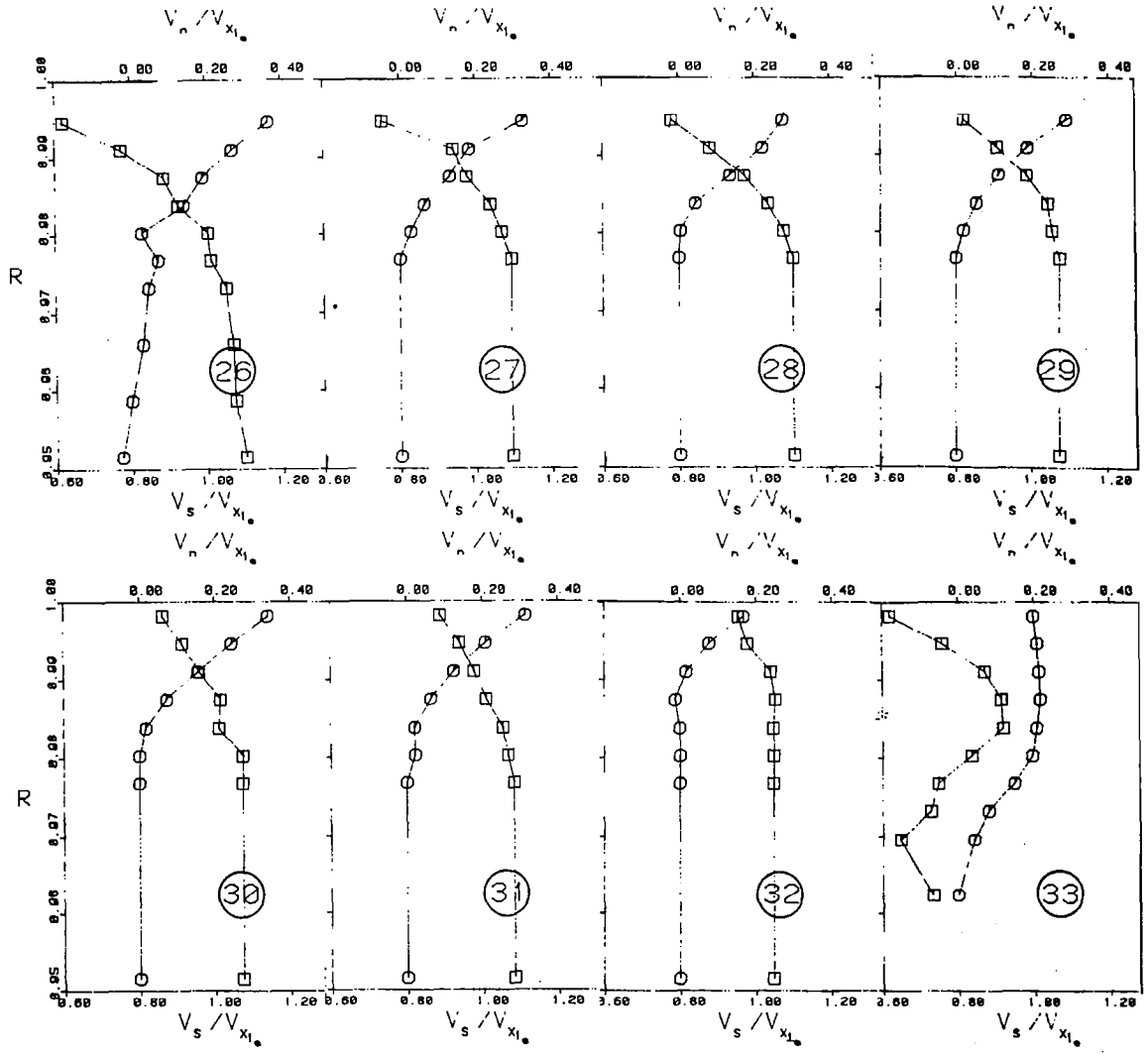

Fig. 31g Z = 1.44

Figure 31. (Concluded)

Far downstream, at Z = 1.44, the boundary layer behavior is very similar to that at earlier axial stations. The unusual shape of the boundary layers at position 33 (Figure 31g) is due to the fact that this radial traverse is in the wake, which is not radial. Also the axial distance between the probe and IGV trailing edge varies with the radial position of the probe. Hence the probe also senses different axial development of the wake. The cross flows are still large even at this location.

The velocity vectors in the x-θ plane at two radii are shown in Figure 32. The velocity vectors in the boundary layer (R = 0.997) are represented by dotted lines and the velocity vectors in the freestream (R = 0.963) are represented by solid lines. At Z = 0.25, the boundary layer velocity vector is smaller in magnitude than the velocity vector in the freestream, but the direction is the same, except near the pressure surface. The freestream velocity seems to deviate considerably from the blade surfaces. Beyond Z = 0.25, the velocity in the boundary layer deviate considerably both in magnitude and direction, from the velocity vector in the free stream. The difference in the directions of velocity vectors in the boundary layer and free stream increases with the axial distance, thus indicating increasing strength of secondary vorticity.

Secondary Flow Velocity Vector Plots

The secondary flow velocity vector plots at axial stations 1 to 5 (Z = 0.25 to Z = 1.44, Figure 26) are shown in Figure 33. Since in the IGV of an actual turbomachine, the primary streamline direction is very difficult to determine (in a linear cascade the primary streamline direction can be determined from the flow measurements in the mid span region, where secondary flow effects do not exist), the following method is adopted. The primary streamline is assumed to follow the camberline at all blade elements. The slopes of the camberlines at the tip section (R = 1.0) and at section R = 0.95 were averaged at each axial station and the secondary velocities are determined based on this primary streamline direction and the measured data. Since the variation of camber from R = 0.95 to 1.0 is small and the boundary layer is thin, the error involved in using these average values is small.

At Z = 0.25 (Figure 33a), the magnitude of cross flows (V_n) are large and radial velocities (V_r) are small. This is in consistance with the limiting streamline angle measurements, which shows large values of limiting streamline angle at this location (Figure 29) and the presence of large crosswire pressure gradients (Figure 30). The secondary flows are comparatively small in the mid passage. At Z = 0.52 (Figure 33b), the magnitude of radially inward velocity is considerably higher, indicating stronger secondary velocities. The boundary layer edge is indicated by the smaller magnitudes of secondary velocities. The cross flow velocities are maximum near the annulus wall.

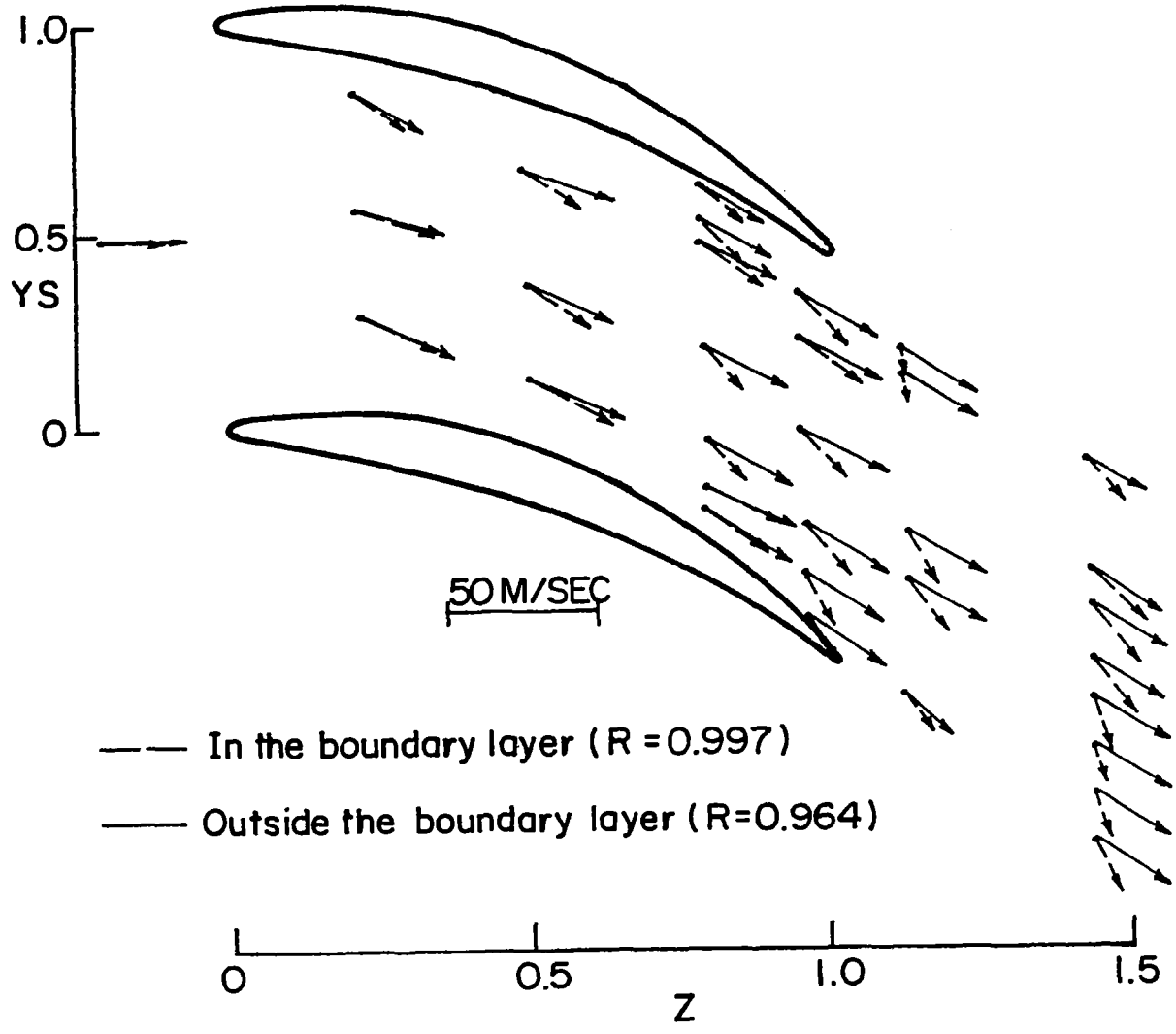

Figure 32. IGV Endwall Flow Velocity Vectors ($\bar{\phi}$ = 0.556)

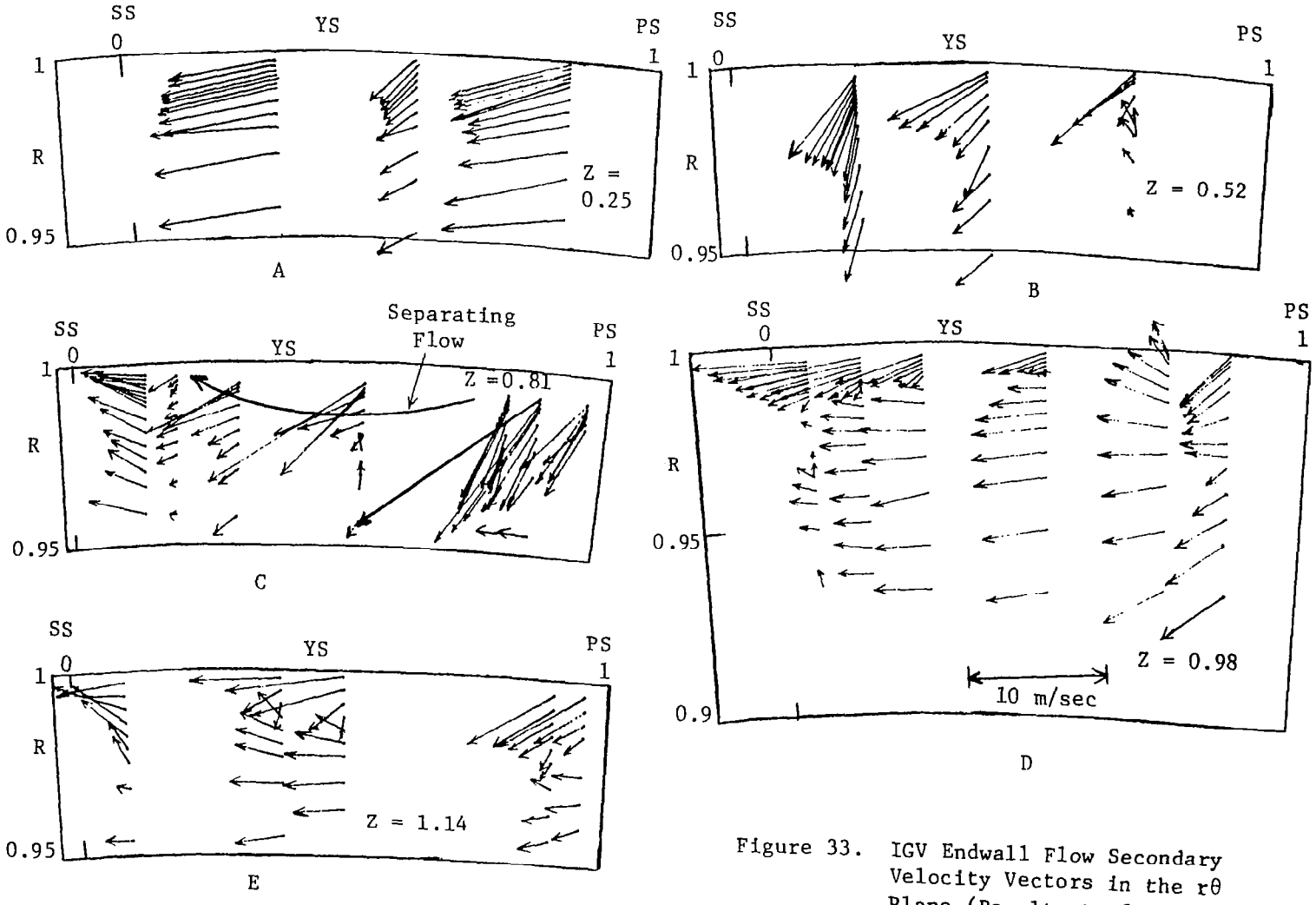

Figure 33. IGV Endwall Flow Secondary Velocity Vectors in the $r\theta$ Plane (Resultant of Cross Flow and Radial Velocities), $\phi = 0.556$

The secondary velocities are the highest at Z = 0.81 (Figure 33c) and this persists even at Z = 0.98. There is a reduction in secondary velocity at Z = 1.14 (Figure 33c). The secondary flow trend seems to be reversed at this axial location.

The blade to blade distribution of the normal velocity (V_n) and the radial velocity (V_r) are shown in Figures 34 and 35, respectively. Discussion of the cross flow velocity is given earlier. The spanwise (or the radial velocity) plots indicate that the spanwise velocities are small at Z = 0.25. Conventional radial outward velocity near the pressure surface and outward velocity near the suction surface is observed at Z = 0.52 (Figure 35b). This trend seems to be reversed at Z = 0.81 (Figure 35c). The plot at Z = 0.98 clearly indicates the radial velocities are well developed at this station. The secondary flow velocities are large even at Z = 1.44 (Figure 35f).

Stagnation Pressure, Static Pressure and Loss Profiles

The stagnation and static pressures and loss profiles at various measurement locations are shown in Figure 36. The pressures are normalized with respect to the dynamic head based on the inlet axial velocity at the mid span. The abscissa is the non-dimensionalized radius.

The stagnation pressure profiles are very similar to that of the streamwise velocity profiles. At stations 21, 25, and 33, the S shape of stagnation pressure and losses are due to the wake of the blade, which is non-radial.

The losses are defined as the difference between the local stagnation pressure and the inlet stagnation pressure at the same radial location. As expected the losses increases toward and beyond the trailing edge. At some locations, slightly negative losses are observed in the freestream region. This is probably due to non-axisymmetric streamsurfaces.

The static pressure is fairly constant, across the boundary layer, at all measuring stations, except those through which the blade wake passes.

The passage averaged and overall stagnation pressure loss coefficients are shown in Figures 37 and 38, respectively. They are defined as follows:

$$\bar{C}_{p_{loss}} = \int_{\theta_s}^{\theta_p} V_x C_{p_{loss}} \, d\theta \Big/ \int_{\theta_s}^{\theta_p} V_x \, d\theta$$

and

$$\bar{\bar{C}}_{p_{loss}} = \int_{r_t - \delta_t}^{r_t} \bar{C}_{p_{loss}} \, dr / \delta_t$$

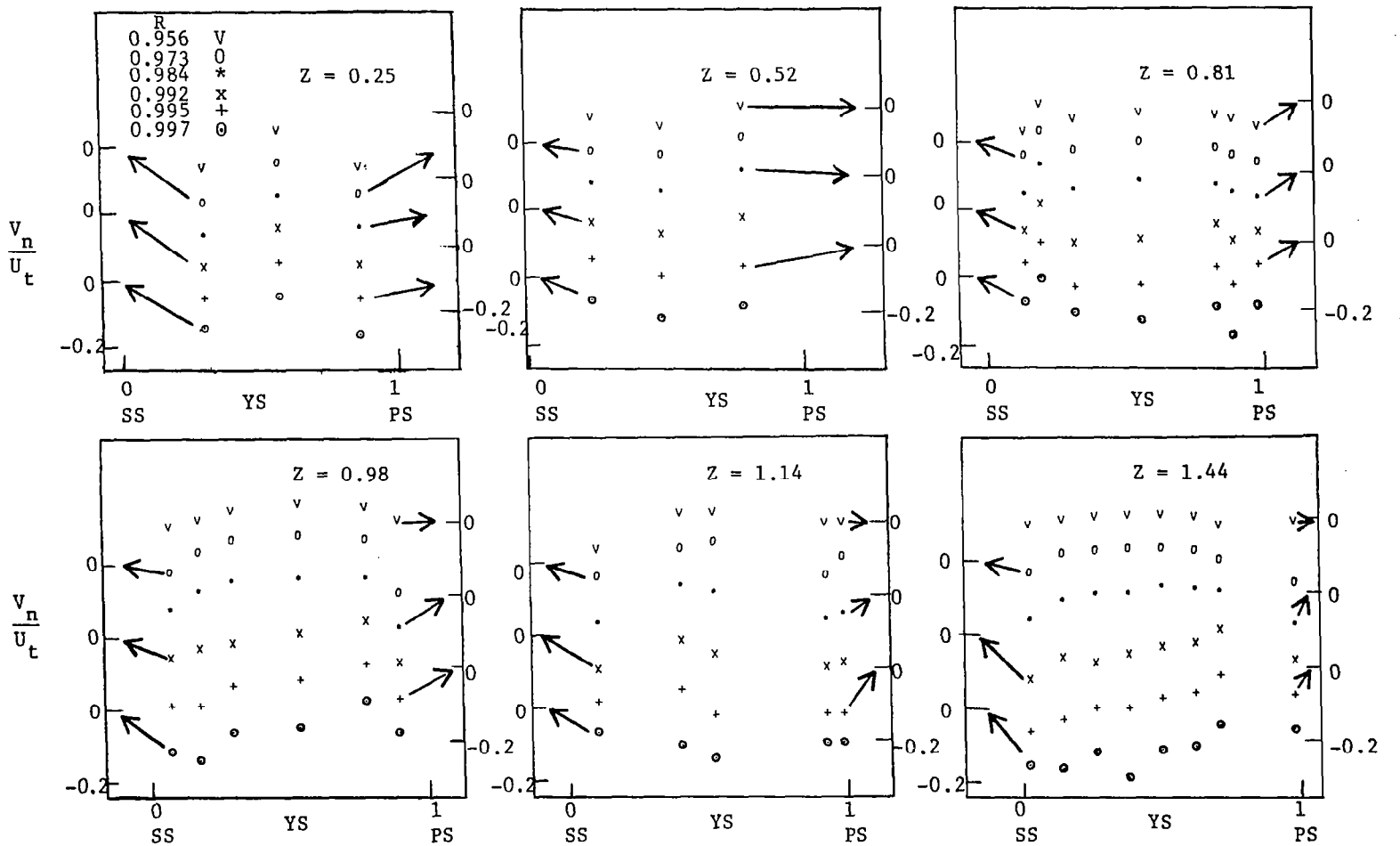

Figure 34. IGV Endwall Flow Blade-to-Blade Distribution of Secondary Velocity ($\bar{\phi}$ = 0.556): V_n/U_t

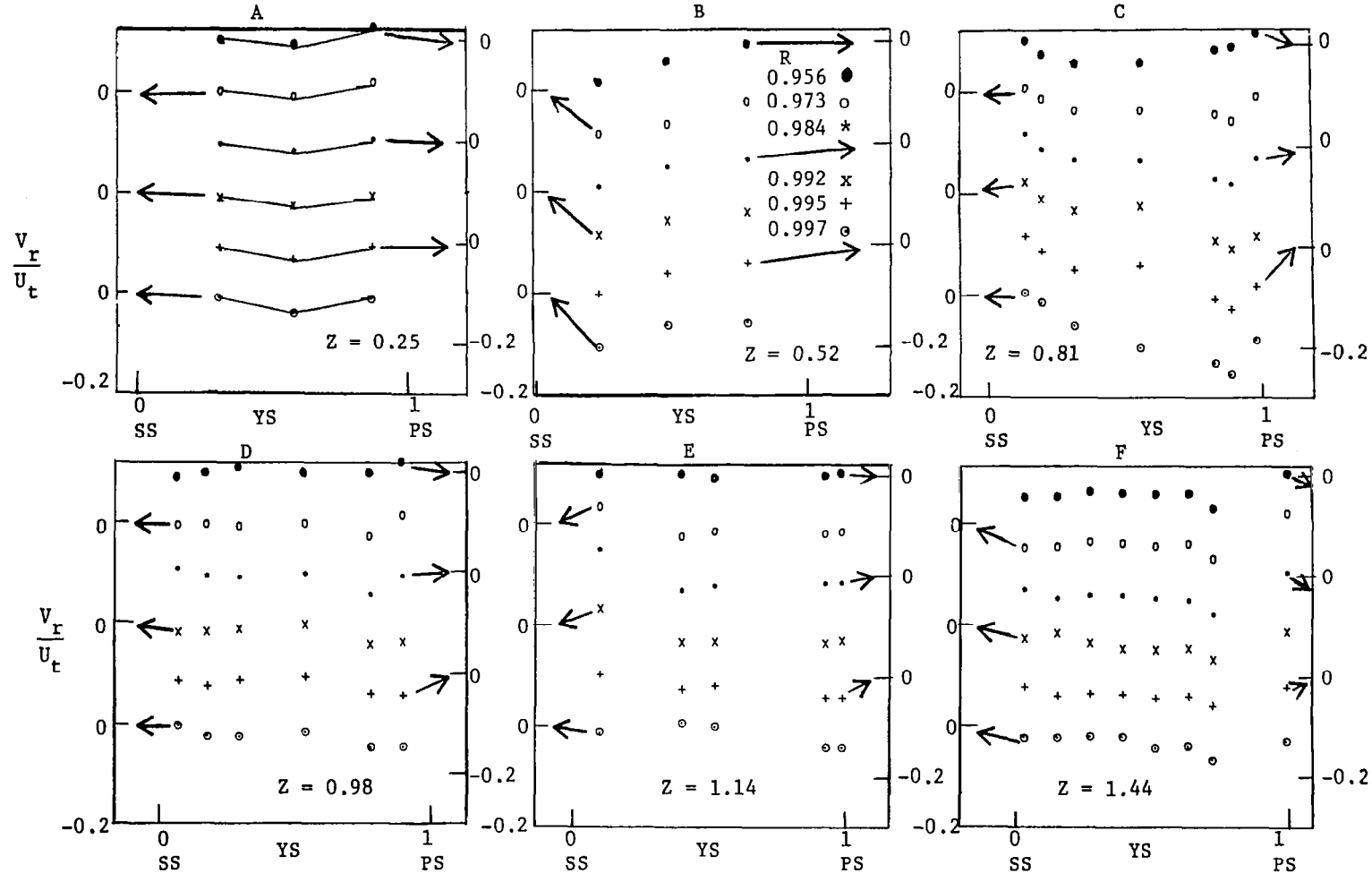

Figure 35. IGV Endwall Flow Blade-to-Blade Distribution of Secondary Velocity ($\bar{\phi}$ = 0.556) V_r/U_t

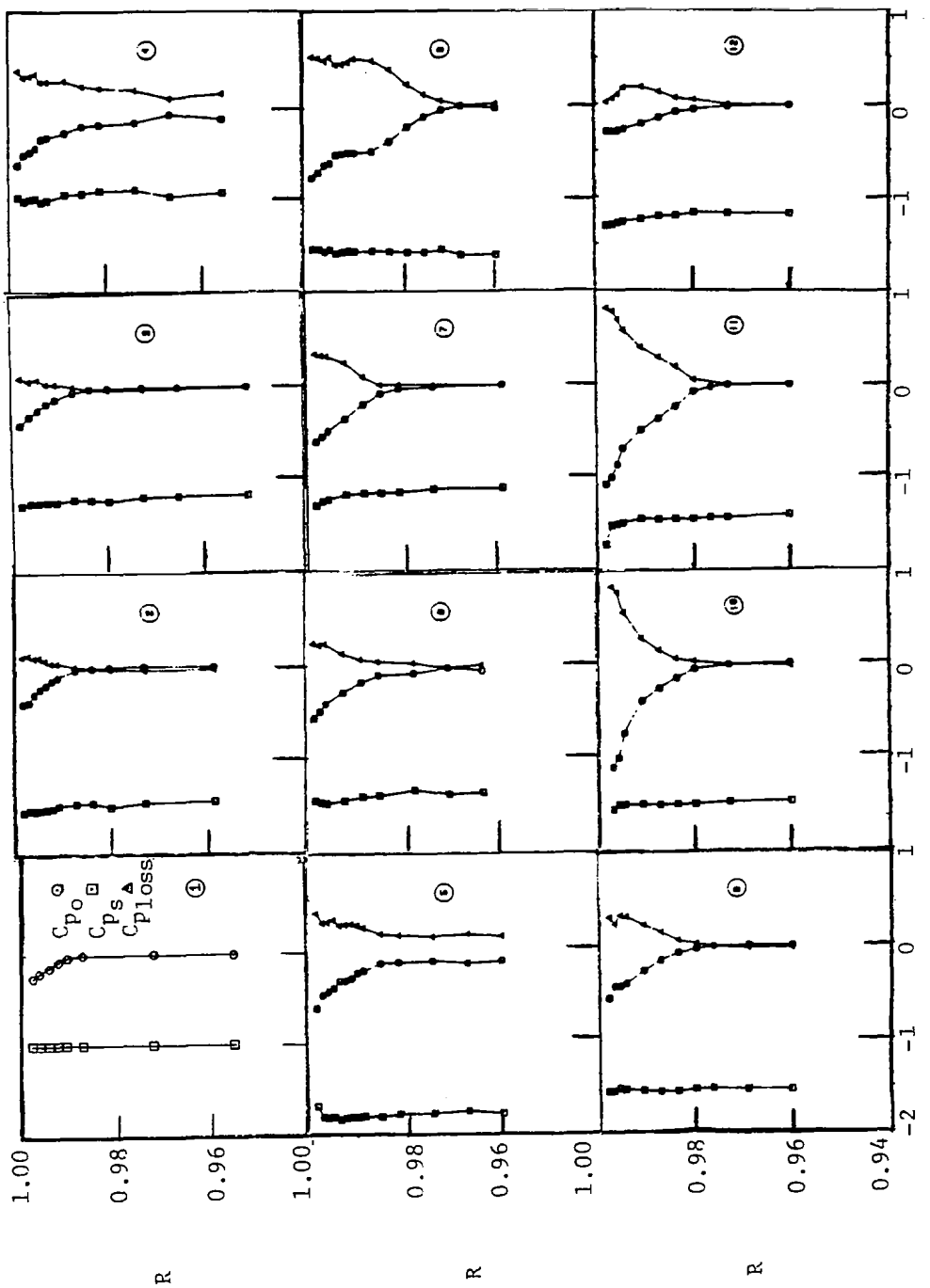

Figure 36. IGV Endwall Flow Distribution ($\bar{\phi}$ = 0.556)

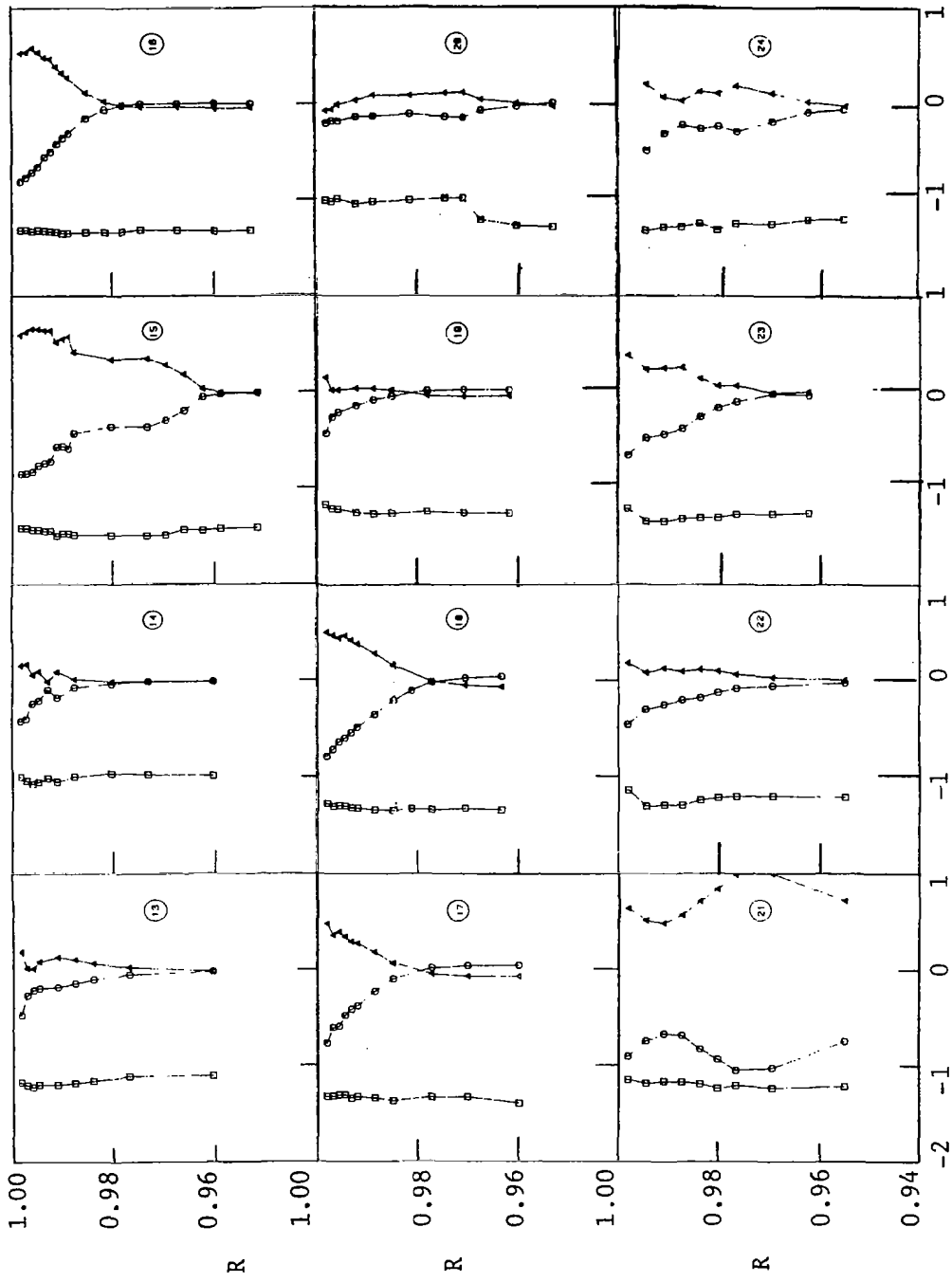

Figure 36. (continued)

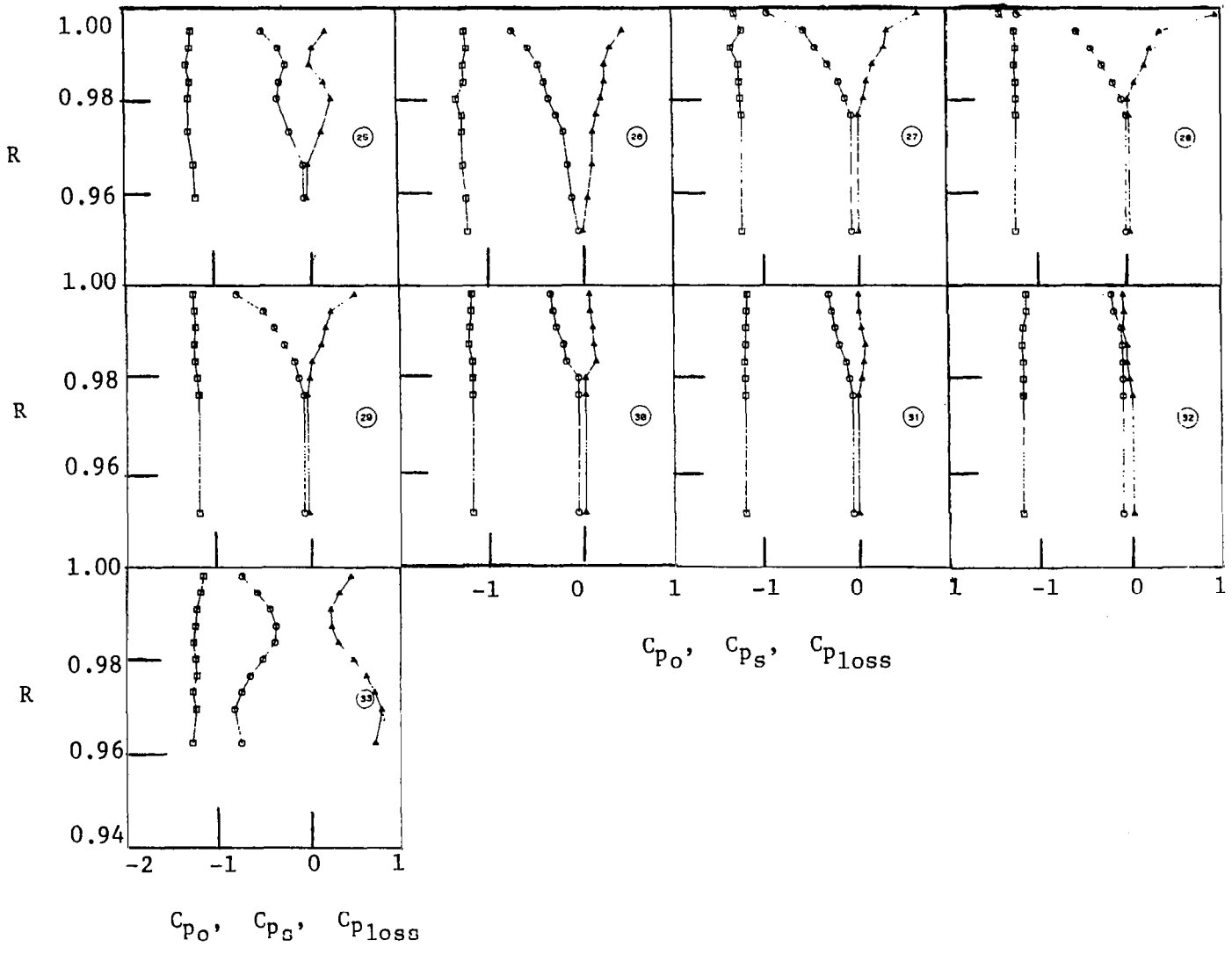

Figure 36. (continued)

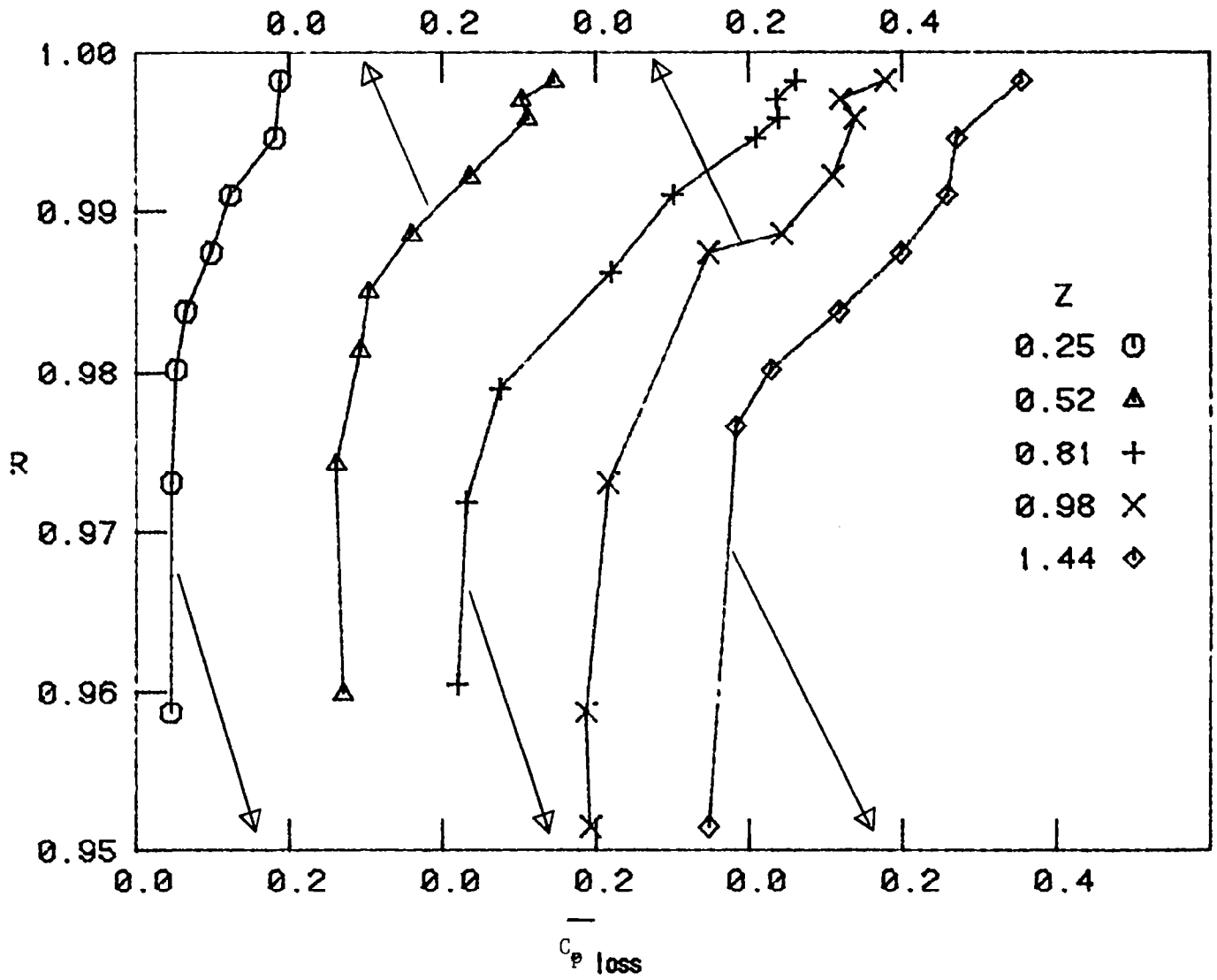

Figure 37. IGV Endwall Flow: Passage Averaged Stagnation Pressure Loss Coefficients ($\bar{\phi}$ = 0.555)

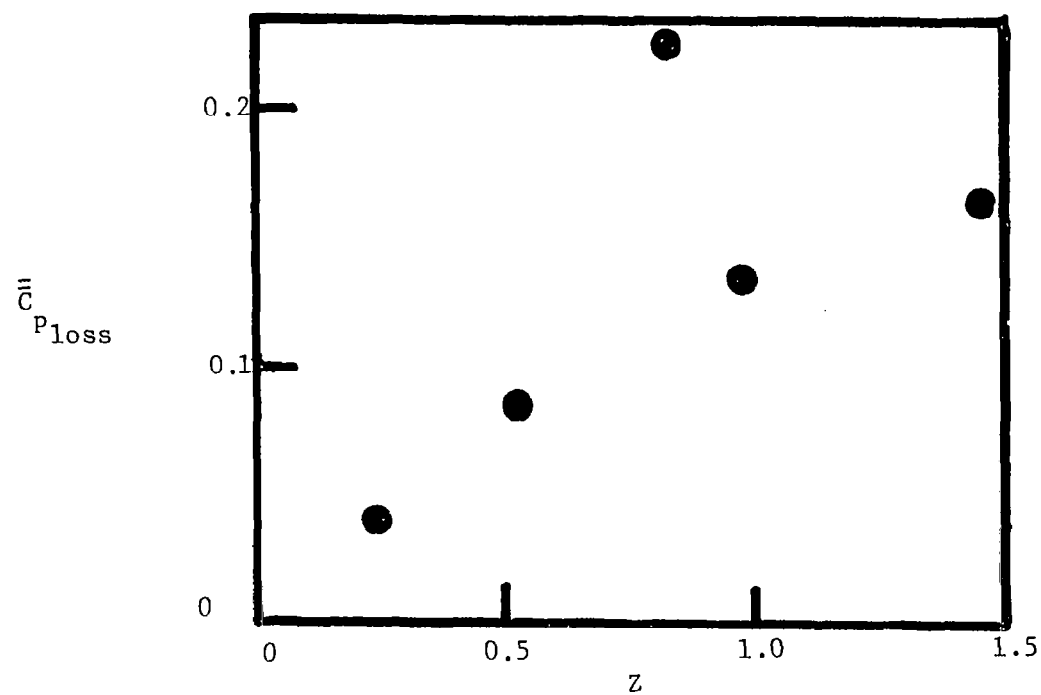

Figure 38. IGV Endwall Flow Overall Stagnation Pressure Loss Coefficient ($\bar{\phi}$ = 0.556)

The overall loss coefficient at axial station Z = 0.81 is larger than those downstream. This is due to the flow separation near the suction surface at this axial station. Overall and passage averaged stagnation pressure loss coefficients at axial station Z = 1.14 are not shown, due to the insufficient number of measurement stations across the passage. The overall loss coefficient increases linearly (except at Z = 0.81) along the passage from zero at Z = 0 to 0.16 at Z = 1.44 (Fig. 38).

Boundary Layer Integral Thicknesses

The boundary layer integral parameters at various axial locations are shown in Figure 39 a and b and tabulated in Tables VII, VIII, and IX. These are obtained from the measured data utilizing the definitions given in Appendix B. Since these parameters vary considerably from the suction surface to the pressure surface, they are calculated for all the measuring positions. The parameters based on passage averaged values are given in Figure 40.

The boundary layer at inlet and at Z = 0.25 is very thin and gives very small values of δ^*_x, θ^*_x, δ^*_s, θ^*_s (Figure 39a). At Z = 0.25 and at Z = 0.52, δ^*_x, θ^*_x, δ^*_s, θ^*_s are larger on the pressure surface side than the corresponding values on the suction surface. This trend reverses beyond Z = 0.52. δ^*_θ and θ^*_θ are negative at most measuring locations, since V_θ is increasing radially. The momentum and displacement thickness in streamwise coordinate system is shown in Figure 39b. The trend is similar to those observed for θ^*_x.

The axial shape factor is greater than 2.20 near the suction surface beyond Z = 0.98, indicating separation.

The passage averaged boundary layer integral quantities are presented in Figure 40. The velocity profiles are first passage averaged and then integrated along the radius.

The momentum and displacement thicknesses both in the axial and streamwise directions show a rapid increase beyond Z = 0.52 and levels off at Z = 0.98, beyond which a slight decrease is noted. As mentioned earlier, the values at Z = 1.14 should be viewed cautiously. The axial shape factor is higher than the streamwise shape factor and increases at slightly faster rate.

IGV Wake in the Endwall Region

A dual sensor hot wire probe was used to measure the axial and tangential velocities and turbulence intensities at two axial stations (0.64 cm and 17.76 cm downstream of the IGV trailing edge) and at R = 0.973, 0.986 radial stations. One complete IGV blade passage is surveyed at the design flow coefficient (ϕ = 0.555). The results are plotted in Figures 41 and 42 for Z = 1.11 and 1.92 for R = 0.973 and 0.986, respectively. At each radial location, the axial velocity, tangential velocity, axial and tangential components of turbulence intensity are plotted. At Z = 1.11, the velocity defect in the wake is appreciable. The wake width is nearly the same at both radii. As expected the turbulence intensities are high

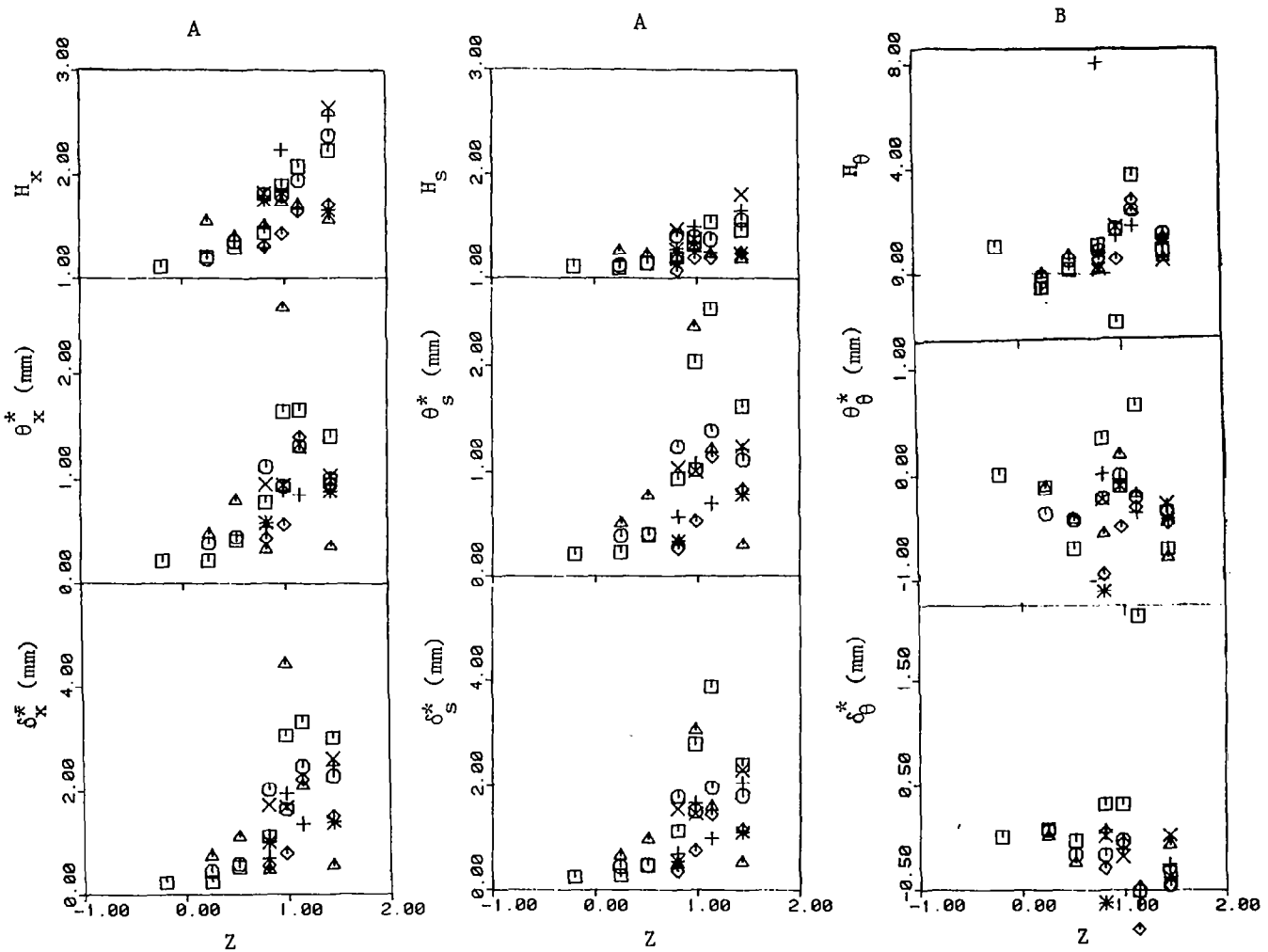

Figure 39. IGV Endwall Flow Integral Parameters (for Legend See Table VI.and Appendix B).

Table VII. IGV Boundary Layer Edge Quantities, $\bar{\phi} = 0.556$

No.	δ mm	V_e m/sec	V_{x_e} m/sec	V_{θ_e} m/sec	V_{r_e} m/sec	α_e	β_e
1	4.20	29.40	29.40	0	0	0	0
2	5.88	34.47	31.15	14.75	-0.79	25.33	-1.46
3	7.56	31.47	30.24	8.61	-1.35	15.90	-2.55
4	7.00	24.45	21.29	12.03	-0.07	29.46	-0.20
5	7.00	36.86	33.69	14.25	-4.51	22.93	-7.63
6	7.00	32.69	29.45	13.97	-2.389	25.38	-4.64
7	8.68	30.40	28.60	10.20	-1.38	19.63	-2.77
8	9.80	33.40	28.61	17.16	1.42	30.96	2.85
9	9.24	35.24	32.28	14.14	0.21	23.65	0.37
10	12.55	34.87	30.66	16.59	-0.79	28.41	-1.47
11	10.87	34.10	30.57	15.09	-0.75	26.27	-1.41
12	9.24	30.23	26.53	14.28	-2.46	28.28	-5.29
13	10.87	29.66	25.53	14.99	-1.84	30.42	-4.11
14	9.24	27.80	23.17	15.34	-0.55	33.50	-1.37
15	17.59	33.89	27.73	19.49	-0.54	35.11	-1.11
16	8.68	32.59	27.46	17.53	-0.42	32.55	-0.88
17	10.59	33.47	29.06	16.60	-0.52	29.73	-1.02
18	8.68	31.89	27.98	15.30	-0.21	28.66	-0.43
19	10.31	32.30	28.14	15.79	-1.61	29.30	-3.27
20	25.43	32.22	27.94	15.93	1.90	29.70	3.89
21	20.95	19.82	14.29	13.73	0.07	43.85	0.28
22	14.23	30.82	26.42	15.87	-0.54	31.00	-1.17
23	14.23	32.18	27.80	16.21	-0.32	30.24	-0.65
24	20.95	30.87	25.54	17.32	0.07	34.14	0.15
25	15.91	31.62	25.34	17.50	-0.27	33.60	-0.60
26	19.27	30.99	25.28	17.76	-2.36	35.08	-5.33
27	10.87	31.53	26.16	17.44	-2.31	33.69	-5.05
28	10.84	31.73	26.64	17.14	-1.78	32.75	-3.82
29	10.87	30.91	26.16	16.36	-1.93	32.02	-4.22
30	10.87	30.96	26.21	16.31	-2.24	31.89	-4.89
31	10.87	31.21	26.23	16.79	-1.96	32.62	-4.28
32	10.87	30.17	24.50	17.26	-3.48	35.16	-8.07
33	14.23	18.67	15.13	10.95	0.51	35.90	1.92

Table VIII. IGV Boundary Layer Integral Quantities--Cartesian Coordinate System, $\bar{\phi} = 0.556$

No.	δ^*_x mm	δ^*_θ mm	δ^*_r mm	θ^*_x mm	$\theta^*_{x\theta}$ mm	θ^*_{xr} mm	$\theta^*_{\theta x}$ mm	θ^*_θ mm	$\theta^*_{\theta r}$ mm	θ^*_{rx} mm	$\theta^*_{r\theta}$ mm	θ^*_r mm
1	0.22	0	0	0.2	0	0	0	0	0	0	0	0
2	0.233	0.077	-0.153	0.195	0.094	-0.006	0.064	0.030	-0.002	-0.133	-0.064	0.004
3	0.431	0.062	-0.431	0.369	0.114	-0.030	0.056	0.016	-0.004	-0.384	-0.114	0.027
4	0.726	0.010	-0.161	0.472	0.352	-0.020	0.004	0.003	0.001	-0.120	-0.080	0.114
5	0.513	-0.044	-0.866	0.398	0.205	-0.071	-0.034	-0.018	0.006	-0.721	-0.341	0.114
6	0.584	-0.713	-0.547	0.436	0.277	-0.051	-0.127	-0.082	0.015	-0.442	-0.249	0.046
7	1.096	-0.244	-0.553	0.791	0.437	-0.090	-0.160	-0.105	0.024	-0.430	-0.209	0.042
8	1.094	0.319	0.456	0.771	0.515	0.047	0.226	0.150	0.014	0.343	0.220	0.024
9	0.679	0.038	-0.001	0.530	0.267	-0.006	0.032	0.015	0.000	0.005	-0.001	0.001
10	1.698	0.014	-0.400	0.936	0.765	-0.090	-0.030	-0.008	-0.006	-0.261	-0.184	0.017
11	2.004	-0.169	-0.447	1.114	0.963	-0.146	-0.076	-0.093	0.013	-0.254	-0.211	0.038
12	0.535	-0.290	-1.223	0.416	0.282	-0.095	-0.226	-0.154	0.052	-0.978	-0.629	0.190
13	0.992	-0.633	-1.566	0.573	0.642	-0.200	-0.404	-0.398	0.127	-1.147	-0.918	0.269
14	0.459	0.062	-0.773	0.310	0.240	-0.058	0.039	0.031	-0.011	-0.586	-0.416	0.085
15	3.029	0.307	-0.218	1.629	1.669	-0.036	0.178	0.168	-0.005	-0.142	-0.120	0.005
16	1.919	-0.138	-0.219	0.867	1.083	-0.064	-0.065	-0.078	0.004	-0.121	-0.122	0.007
17	1.639	-0.218	-0.226	0.917	0.869	-0.048	-0.133	-0.115	0.006	-0.148	-0.118	0.006
18	1.587	-0.085	-0.099	0.903	0.785	-0.025	-0.050	-0.042	0.001	-0.061	-0.049	0.001
19	0.729	-0.109	-0.690	0.529	0.362	-0.054	-0.088	-0.057	0.007	-0.547	-0.345	0.049
20	4.349	-1.802	0.050	2.590	2.568	-0.094	-1.146	-1.051	0.026	0.138	-0.001	0.043
21	3.263	2.061	1.050	1.615	1.701	0.157	0.928	0.793	0.086	0.600	0.642	0.114
22	1.296	-0.621	-0.528	0.813	0.787	-0.030	-0.412	-0.381	0.021	-0.423	-0.293	0.026
23	2.382	-0.567	-0.389	1.269	1.403	-0.062	-0.286	-0.353	0.017	-0.274	-0.213	0.014
24	2.140	-0.939	-0.581	1.361	1.384	-0.099	-0.595	-0.519	0.045	-0.381	-0.371	0.026
25	2.015	-0.529	-0.415	1.228	1.243	-0.083	-0.312	-0.340	0.023	-0.262	-0.253	0.016
26	2.910	-0.391	-1.149	1.347	1.767	-0.133	-0.220	-0.238	0.021	-0.804	-0.680	0.079
27	2.363	-0.321	-0.610	0.950	1.374	-0.113	-0.199	-0.198	0.018	-0.393	-0.356	0.040
28	2.458	-0.050	-0.573	0.962	1.257	-0.114	-0.113	-0.072	0.008	-0.367	-0.318	0.033
29	2.130	-0.524	-0.668	0.931	1.294	-0.112	-0.277	-0.316	0.031	-0.453	-0.385	0.045
30	1.357	-0.532	-0.734	0.840	0.854	-0.099	-0.311	-0.346	0.038	-0.564	-0.451	0.059
31	1.238	-0.453	-0.739	0.793	0.770	-0.823	-0.277	-0.289	0.029	-0.538	-0.427	0.053
32	0.377	-0.137	-1.185	0.257	0.236	-0.039	-0.092	-0.087	0.014	-0.924	-0.692	0.135
33	-1.169	-4.097	0.092	-1.210	-1.177	-0.037	-3.810	-3.873	-0.017	0.111	0.071	0.028

Table IX. IGV Boundary Layer Integral Quantities--Streamline Coordinate System, $\bar{\phi} = 0.556$

No.	D_f mm	δ^* mm	θ^* mm	δ^*_s mm	δ^*_n mm	θ^*_s mm	θ^*_{sn} mm	θ^*_{sr} mm	θ^*_{ns} mm	θ^*_n mm	θ^*_{nr} mm	θ^*_{rs} mm
1	0	0.22	0.20	0.22	0	0.20	0	0	0	0	0	0
2	0.164	0.242	0.225	0.242	-0.030	0.225	-0.001	-0.006	-0.029	0.000	0.001	-0.147
3	0.174	0.422	0.380	0.423	-0.058	0.381	-0.008	-0.029	-0.050	0.002	0.005	-0.402
4	0.361	0.611	0.496	0.635	-0.349	0.509	-0.065	-0.017	-0.284	0.036	0.010	-0.144
5	0.165	0.433	0.384	0.443	-0.243	0.391	-0.029	-0.061	-0.214	0.016	0.034	-0.805
6	0.123	0.421	0.376	0.447	-0.407	0.395	-0.048	-0.039	-0.358	0.045	0.036	-0.508
7	0.207	0.877	0.736	0.936	-0.602	0.770	-0.120	-0.075	-0.482	0.093	0.053	-0.478
8	0.788	1.090	0.927	1.098	-0.289	0.932	-0.045	0.048	-0.245	0.012	-0.012	0.408
9	0.304	0.629	0.552	0.637	-0.237	0.557	-0.031	-0.006	-0.206	0.013	0.002	0.004
10	0.778	1.417	0.999	1.491	-0.798	1.028	-0.203	-0.081	-0.595	0.102	0.038	-0.318
11	0.811	1.541	1.170	1.699	-1.050	1.226	-0.308	-0.122	-0.742	0.215	0.078	-0.325
12	0.027	0.237	0.227	0.264	-0.519	0.251	-0.025	-0.046	-0.494	0.052	0.093	-1.177
13	0.097	0.254	0.226	0.418	-1.076	0.330	-0.141	-0.086	-0.936	0.268	0.217	-1.480
14	9.292	0.364	0.311	0.372	-0.204	0.316	-0.025	-0.048	-0.178	0.013	0.023	-0.724
15	1.920	2.492	1.956	2.652	-1.490	2.014	-0.370	-0.032	-1.120	0.218	0.017	-0.185
16	0.967	1.336	0.994	1.541	-1.149	1.055	-0.360	-0.051	-0.790	0.266	0.038	-0.168
17	9.679	1.187	0.926	1.312	-1.003	0.979	-0.243	-0.039	-0.760	0.178	0.029	-0.187
18	0.711	1.254	0.957	1.350	-0.836	0.994	-0.218	-0,022	-0.618	0.134	0.013	-0.077
19	0.268	0.548	0.479	0.568	-0.453	0.494	-0.046	-0.042	-0.406	0.034	0.033	-0.648
20	1.005	2.435	2.028	2.905	-3.724	2.330	-0.655	-0.069	-3.069	0.772	0.069	0.119
21	3.188	3.642	2.436	3.713	-0.777	2.491	-0.025	0.165	-0.751	0.127	-0.047	0.885
22	0.255	0.651	0.560	0.780	-1.201	0.651	-0.160	-0.014	-1.041	0.230	0.034	-0.514
23	0.913	1.473	1.201	1.765	-1.691	1.338	-0.414	-0.044	-1.278	0.428	0.046	-0.345
24	0.606	1.024	0.935	1.230	-1.982	1.093	-0.213	-0.056	-1.767	0.363	0.093	-0.525
25	0.802	1.203	1.056	1.377	-0.557	1.172	-0.234	-0.056	-1.324	0.290	0.066	-0.359
26	1.448	1.847	1.440	2.168	-1.996	1.562	-0.514	-0.097	-1.482	0.443	0.094	-1.052
27	1.108	1.480	1.073	1.796	-1.582	1.147	-0.486	-0.085	-1.096	0.389	0.078	-0.526
28	1.214	1.780	1.147	2.037	-1.376	1.180	-0.453	-0.091	-0.923	0.291	0.069	-0.482
29	0.850	1.200	0.934	1.523	-0.578	1.036	-0.448	-0.078	-1.130	0.425	0.086	-0.590
30	0.404	0.717	0.644	0.869	-1.172	0.752	-0.171	-0.064	-1.002	0.260	0.085	-0.720
31	0.389	0.677	0.613	0.792	-1.052	0.698	-0.135	-0.053	-0.917	0.199	0.069	-0.685
32	0.124	0.207	0.193	0.230	-0.332	0.212	-0.026	-0.023	-0.305	0.042	0.034	-1.162
33	-4.495	-3.591	-4.866	-3.359	-2.635	-4.507	0.730	-0.040	-3.365	0.590	0.008	0.132

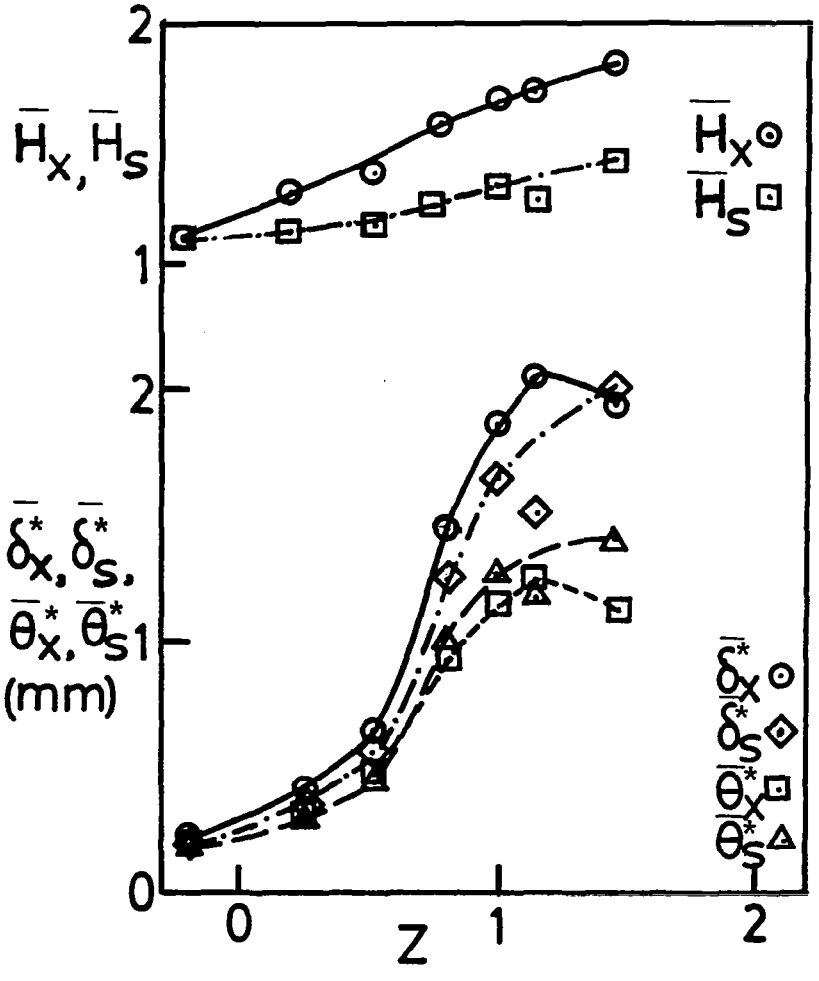

Figure 40. IGV Endwall Flow: Passage Averaged Boundary Layer Integral Parameters ($\bar{\phi}$ = 0.556)

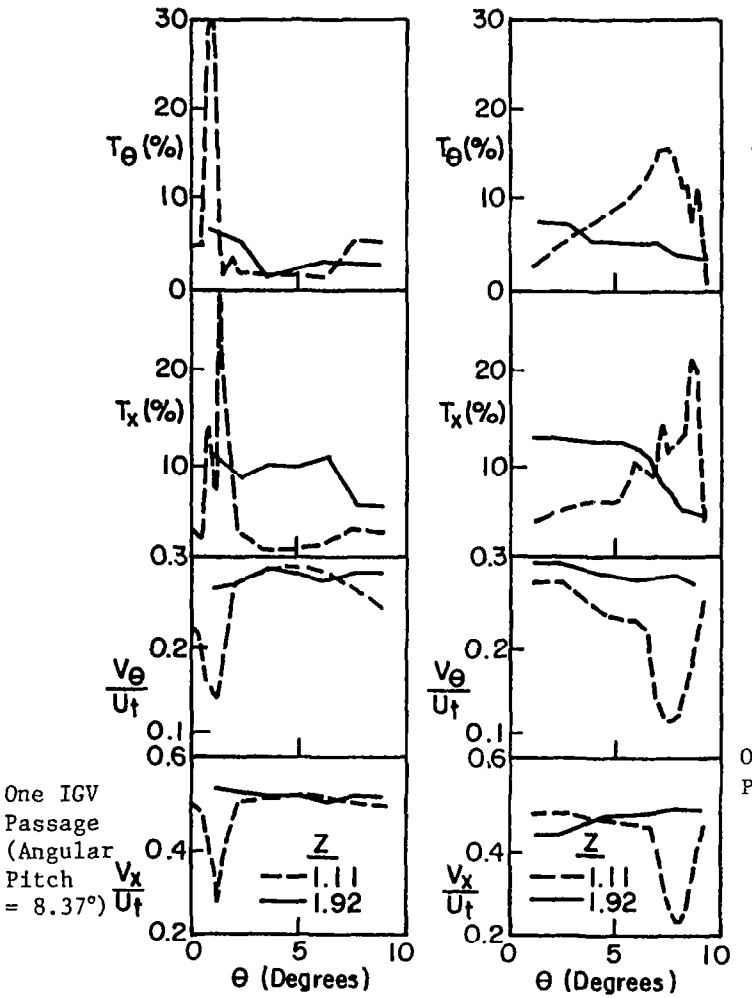

Figure 41. IGV Wake at R = 0.973 ($\bar{\phi}$ = 0.556)

Figure 42. IGV Wake at R = 0.986 ($\bar{\phi}$ = 0.556)

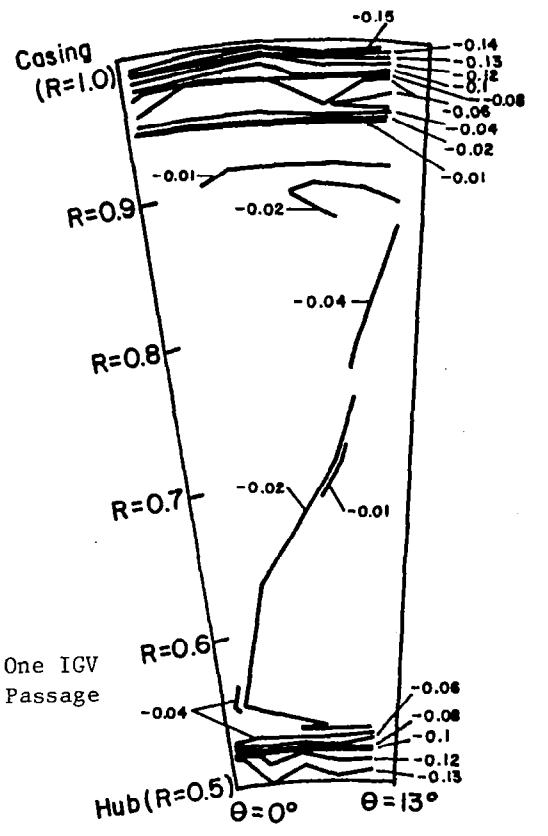

Figure 43. Stagnation Pressure Loss Contours ($C'_{p_{loss}}$) at Z = 1.92 ($\bar{\phi}$ = 0.556)

in the wake region. The turbulence intensities at the edge of the wake are also high, and this is caused by the presence of the hub and casing wall boundary layers.

At the axial station 17.76 cm downstream of the IGV trailing edge, the wake has decayed completely at R = 0.973 and the velocity defect in the wakes is very small at R = 0.986. The turbulence intensities are relatively high as these two radii are inside the annulus wall boundary layer. Details of the wake in the mid-span region are reported and correlated in ref. 210.

The stagnation pressures were measured at 17.76 cm downstream of IGV trailing edge (7.62 cm or half-a-chord upstream of the rotor leading edge) at various radial stations across one IGV blade passage. Boundary layer type pitot probe were used in the hub and casing boundary layers and a conventional pitot probe was used at other radial stations. All pressures were measured by a pressure transducer. The stagnation pressures, non-dimensionalized with respect to the dynamic head based on tip speed ($\rho U_t^2/2$), are plotted in contour form in Figure 43. Since the measuring station is far downstream, the defect in stagnation pressure in the wake is small. The stagnation pressure coefficient less than zero indicates losses. The loss is confined to 10 percent of the blade tip, with maximum value of -0.15 occurring near the wall. The losses in the wake region are evident at all radial locations.

Concluding Remarks

The wall boundary layer development in the IGV blade passage of a low speed moderately loaded axial flow compressor stage is reported. The following conclusions can be drawn from this investigation.

1. Even though the inlet boundary layer is quite thin, the turning is small, flow separation is observed near suction surface close to the trailing edge.

2. Strong secondary vorticity is developed, giving rise to highly three dimensional flow in the IGV endwall region with considerable flow deviation from inviscid flow.

3. The character of flow changes considerably along the axial distance. The boundary layer on the suction surface is thinner than that on the pressure surface in the first half of IGV chord length. Beyond this point, the trend reverses.

4. The wake defect and turbulence intensities are high close to the trailing edge. Far downstream the wake defect is negligibly small, but turbulence intensities are high.

CONCLUSIONS

A low speed axial flow compressor stage with capabilities to measure flow field inside the rotor blade passage is used to study the flow field in the rotor endwall region and the IGV endwall region. Extensive radial flow surveys were carried out at the design and at various off design conditions. Theoretical investigations of the endwall flows include the secondary flow calculation and the development of the momentum integral equations for the prediction of the annulus wall boundary layers. The exhaustive review on the endwall flows included in this report highlights the achievements and limitations of the previous investigations and directions along which future experimental and theoretical investigations on the endwall flows should take place. These concluding remarks are not repeated here and the reader is referred to these conclusions elsewhere in this report. The other conclusions that are drawn from the present investigation are as follows.

1. The secondary flow analysis reported here includes the effects of rotation and viscosity in the generation of secondary vorticity. The comparison between the results from this analysis and the secondary vorticity obtained from the simple inviscid analysis shows considerable difference. The difference is attributed to the effects of rotation and viscosity.

2. The axial flow compressor stage described is suitable for measurements inside the rotor blade passage, because of its unique features (i.e., the rotating traverse mechanism and the data transmission system to transmit the signals from the rotating probes to the stationary instruments). The overall performance presented in this report shows that the compressor stage is operating well and its efficiency is quite high.

3. Comparison of the radial distribution of flow properties with an axisymmetric streamline curvature program shows large discrepancies in the endwall regions. The losses in these regions are high, and hence, a proper correlation including the endwall effects should be incorporated in the streamline curvature method to obtain better prediction of the flow.

4. The boundary layer incoming to the rotor tip is fairly thick (35 mm), three dimensional and unconventional in nature. The three-dimensional and unconventional nature of this boundary layer is attributed to the secondary flow at the IGV exit. The turbulence intensities observed in the boundary layer are much higher than those observed in the inlet boundary layer.

5. The static pressure distribution measured on the rotor blade at midspan compares well with that predicted by two-dimensional Douglas Neumann cascade program. Comparison at other radii shows considerable difference, the difference increasing towards the blade hub and tip. The blade static pressure near the tip shows large decrease in the loading. Also the suction peak occurs beyond the mid-chord.

6. The tip clearance effect for this rotor is seen to extend to 20 percent of the span at flow coefficients above stall. Larger leakage flow is observed at the design flow coefficient (where the pressure rise coefficient is maximum).

7. Even though the inlet boundary layer is quite thin, the turning is small, flow separation is observed near the suction surface close to the trailing edge in the end wall region of the inlet guidevane. Strong secondary vorticity is developed in these regions giving rise to highly three dimensional flow in the IGV endwall region with considerable flow deviation from inviscid flow.

8. The character of flow in the end wall region of IGV changes considerably along the axial distance. The boundary layer on the suction surface is thinner than that on the pressure surface in the first half of IGV chord length. Beyond this point, the trend reverses.

REFERENCES

1. Lindsay, W. L. "Tip clearance effects in the growth of annulus wall boundary layers in turbomachines," Ph.D. Thesis, Cambridge University, 1974.

2. Sjolander, S. A., "The endwall boundary layer in an annular cascade of turbine nozzle guide vanes," T. R. No. ME/A75-4, Carleton University, 1975.

3. Lakshminarayana, B., "Loss evaluation methods in axial compressors," in Proceedings of the Workshop on Flow in Turbomachines (Ed. M. H. Vavra, K. D. Papailiou and J. R. Wood) pp. 11-1 to 11-24, 1971.

4. Railly, J. W. and Howard, J. H. G., "Velocity profile development in axial-flow compressors," Journal of Mechanical Engineering Science, Vol. 4, p. 166, 1962.

5. Gruschwitz, E., "Turbulente reibungsschichten mit sekundarstromung," Ingenieur-Archiv., Bd. 6, pp. 355-365, 1935.

6. Jansen, W., "The application of end-wall boundary layer effects in the performance analysis of axial compressor," ASME Paper 67-WA/GT-11, 1967.

7. Stratford, B. S., "The use of boundary layer techniques to calculate the blockage from the annulus boundary layers in a compressor," ASME Paper 67-WA/GT-7, 1967.

8. Smith, L. H., "Casing boundary layers in multistage axial flow compressors," in Flow Research on Blading, Brown Boveri Symposium (Ed. L. S. Dzung), 1970.

9. Mellor, G. L. and Wood, G. M., "An axial compressor end-wall boundary layer theory," Journal of Basic Engineering, Transactions of ASME, Vol. 93, pp. 200-216, 1971.

10. Horlock, J. H. and Hoadley, D., "Calculation of the annulus wall boundary layers in axial flow turbomachines," ARC CP 1196, 1972.

11. Mellor, G. L. and Strong, R. E., "End-wall effects in axial compressors," ASME Paper 67-FE-16, 1967.

12. Moore, R. W., Jr., and Richardson, D. L., "Skewed boundary layer flow near the endwalls of a compressor cascade," Transactions of ASME, Vol. 79, pp. 1789-1800, 1957.

13. Taylor, E. S., "The skewed boundary layer," Journal of Basic Engineering, Transactions of ASME, pp. 297-307, 1957.

14. Johnston, J. P., "On the three-dimensional turbulent boundary layer generated by secondary flow," Journal of Basic Engineering, Transactions of ASME, Vol. 81, 1960.

15. Mellor, G. L. and Balsa, T. F., "The prediction of axial compressor performance with emphasis on the effect of annulus wall boundary layers," AGARDograph No. 164, pp. 363-378, 1972.

16. Balsa, T. F. and Mellor, G. L., "The simulation of axial compressor performance using an annulus wall boundary layer theory," Journal of Engineering for Power, Transactions of ASME, Vol. 97, pp. 305-317, 1975.

17. Mellor, G. L., "Reconsideration of the annulus flow problem in axial turbomachinery," Journal of Basic Engineering, Transactions of ASME, Vol. 84, pp. 579-586, 1962.

18. Hirsch, Ch., "Endwall boundary layers in axial compressors," Journal of Engineering for Power, Transactions of ASME, Vol. 97, pp. 413-426, 1974.

19. Hirsch, Ch., "Flow prediction in axial flow compressors including endwall boundary layers," ASME Paper 76-GT-72, 1976.

20. Hirsch, Ch. and Warzee, G., "A finite-element method for through-flow calculations in turbomachines," Journal of Fluids Engineering, Transactions of ASME, Vol. 98, pp. 403-421, 1976.

21. DeRuyck, J., Hirsch, Ch., and Kool, P., "Investigation on axial compressor endwall boundary layer calculations," International Joint Gas Turbine Congress and Exhibition, Israel, 1979.

22. DeRuyck, J., Hirsch, Ch., and Kool, P., "An axial compressor endwall boundary layer calculation method," Journal of Engineering for Power, Transactions of ASME, Vol. 101, pp. 233-249, 1979.

23. DeRuyck, J. and Hirsch, Ch., "Investigations of an axial flow compressor endwall boundary layer prediction method," Journal of Engineering for Power, Transactions of ASME, Vol. 103, pp. 20-33, 1981.

24. Comte, A., Ohayon, G., and Papailiou, K. D., "A method for the calculation of the wall layers inside the passage of a compressor cascade," ASME Paper 81-GT-168, 1981.

25. Marsh, H. and Horlock, J. H., "Wall boundary layers in turbomachines," Journal of Mechanical Engineering Science, Vol. 14, pp. 411-423, 1972.

26. Horlock, J. H. and Perkin, H. J., "Annulus wall boundary layers in turbomachines," AGSRDograph No. 185, 1974.

27. Daneshyar, M., "Annulus wall boundary layers in turbomachines," Ph.D. Thesis, Cambridge University, 1974.

28. Horlock, J. H., "Cross-flows in bounded three-dimensional turbulent boundary layers," Journal of Mechanical Engineering Science, Vol. 15, No. 4, p. 274, 1973.

29. Daneshyar, M., Horlock, J. H., and Marsh, H., "Prediction of annulus wall boundary layers in axial flow turbomachines," AGARD-ograph No. 164, 1972.

30. Gregory-Smith, D. G., "An investigation of annulus wall boundary layers in axial flow turbomachines," Journal of Engineering for Power, Transactions of ASME, Vol. 92, pp. 369-376, 1970.

31. Railly, J. W. and Sharma, P. B., "Treatment of the annulus wall boundary layer using a secondary flow hypothesis," Journal of Engineering for Power, Transactions of ASME, Vol. 98, pp. 29-36, 1976.

32. Sockol, P. M., "Endwall boundary layer prediction for axial compressors," NASA TM-78928, 1978.

33. Carrick, H. B., "Secondary flow and losses in turbine cascades with inlet skew," Ph.D. Thesis, Cambridge University, 1976.

34. Stuart, A. R. and Hetherington, R., "The solution of the three-variable duct-flow equations," in Fluid Mechanics, Acoustics and Design of Turbomachinery, (Ed. B. Lakshminarayana, W. R. Britsch, and W. S. Gearhart) Vol. 1, pp. 135-153, 1974.

35. Dring, R. P., "A momentum integral analysis of the three-dimensional turbine endwall boundary layer," Journal of Engineering for Power, Transactions of ASME, Vol. 93, pp. 386-396, 1971.

36. Smith, P. D., "An integral prediction method for three-dimensional compressible turbulent boundary layers," ARC R & M 3739, 1974.

37. Booth, T. C., "An analysis of the turbine end wall boundary layer and aerodynamic losses," ASME Paper 75-GT-23, 1975.

38. Patankar, S. V., Pratrap, V. S. and Spalding, D. B., "Prediction of turbulent flow in a curved pipe," Journal of Fluid Mechanics, Vol. 67, No. 3, p. 583, 1975.

39. Pratrap, V. S. and Spalding, D. B., "Numerical computations of the flow in curved ducts," Aeronautical Quarterly, Vol. 26, p. 219, 1975.

40. Lakshminarayana, B., "Leakage and secondary flows in axial compressor cascades," Ph.D. Thesis, Liverpool University, 1963.

41. Turner, J. T., "An investigation of the endwall boundary layer on a turbine nozzle cascade," Transactions of ASME, Vol. 79, pp. 1801-1806, 1957.

42. Horlock, J. H., "Annulus wall boundary layers in axial compressor stages," Journal of Basic Engineering, Transactions of ASME, Vol. 85, pp. 55-65, 1963.

43. Hansen, A. G., Harzóg, H. Z. and Costello, G. R., "A visualization study of secondary flows in cascades," NACA TN 2947, 1953.

44. Johnsen, I. A. and Bullock, R. O. (Editors), Aerodynamic Design of Axial-Flow Compressors, NASA SP-36, 1965.

45. Senoo, Y., "The boundary layer on the endwall of a turbine nozzle cascade," Transactions of ASME, Vol. 80, pp. 1711-1720, 1958.

46. Senoo, Y., "Three-dimensional laminar boundary layer calculation in curved channel with acceleration," Transactions of ASME, Vol. 80, pp. 1721-1733, 1958.

47. Bario, F., Leboeuf, F., and Papailiou, K. D., "Study of secondary flows in blade cascades of turbomachines," paper presented at the International Symposium on "Applications of Fluid Mechanics and Heat Transfer to Energy and Environmental Problems," University of Patras, Greece, 1981.

48. Langston, L. S., Nice, M. L., and Hooper, R. M., "Three-dimensional flow within a turbine cascade passage," Journal of Engineering for Power, Transactions of ASME, Vol. 99, No. 1, pp. 21-28, 1977.

49. Marchal, Ph. and Sieverding, C., "Secondary flows within turbomachinery bladings," AGARD CP-214, Paper 10, 1977.

50. Klein, A., "Investigation of the effect of the entry boundary layer on the secondary flows in blading of axial flow turbines," BHRA Translation 1004, 1969.

51. Bindon, J. D., "The effect of hub inlet boundary layer skewing on the endwall shear flow in an annular turbine cascade," ASME Paper 79-TT-13, 1979.

52. Mahoney, J. J., Dugan, P. D., Budinger, R. E., and Goelzer, H. F., "Investigation of blade-row flow distributions in axial-flow compressor stage consisting of guide vanes and rotor-blade row," NACA RM E50G12.

53. Boxer, E., "Influence of wall boundary layer upon the performance of an axial flow fan rotor," NACA TN 2291, 1951.

54. Fujii, S., Nishiwaki, H., Gomi, M., and Kavanagh, P., "Some observations on the velocity profiles in fully developed viscous flow in turbomachines," ASME Paper 70-WA/FE-24, 1970.

55. Ikui, T., Inoue, M., and Kuroumaru, M., "Development of velocity profile through a stage of axial flow turbomachinery," JSME Paper 38, 1977.

56. Bois, G., Leboeuf, F., Comte, A., and Papailiou, K. D., "Experimental study of the behavior of secondary flows in a transonic compressor," AGARD CP-214, Paper 3, 1977.

57. Bitterlich, W. and Rubner, K., "Annulus wall boundary layers in axial-flow turbomachines," AGARDograph No. 164, pp. 393-415, 1972.

58. Lakshminarayana, B. and Poncet, A., "A method of measuring three-dimensional rotating wakes behind turbomachinery rotors," Journal of Fluids Engineering, Transactions of ASME, Vol. 96, No. 4, pp. 87-91, 1974.

59. Hirsch, Ch. and Kool, P., "Measurements of the three-dimensional flow field behind an axial compressor stage," ASME Paper 76-GT-18, 1976.

60. Davino, R. M. and Lakshminarayana, B., "Characteristics of mean velocity in the annulus wall region at the exit of turbomachinery rotor passage," AIAA Paper 81-0068, 1981.

61. Davino, R. M. and Lakshminarayana, B., "Turbulence characteristics in the annulus wall boundary layer and wake mixing region of a compressor rotor exit," ASME Paper 81-GT-148, 1981.

62. Dring, R. P., Joslyn, H. D., and Hardin, L. W., "An investigation of axial compressor rotor aerodynamics," ASME Paper 81-GT-56 (also published in Journal of Engineering for Power, Vol. 104, 1982), 1981.

63. Sitaram, N., Lakshminarayana, B., and Ravindranath, A., "Conventional probes for the relative flow measurement in a turbomachinery rotor blade passage," Journal of Engineering for Power, Transactions of ASME, Vol. 103, pp. 406-414, 1981.

64. Davino, R. M., "Three dimensional mean and turbulence characteristics in the annulus wall region of an axial flow compressor rotor blade passage," M.S. Thesis, The Pennsylvania State University, 1980.

65. Koch, C. C. and Smith, L. H., "Loss sources and magnitudes in axial-flow compressors," Journal of Engineering for Power, Transactions of ASME, Vol. 98, pp. 411-424, 1976.

66. Hanly, W. T., "A correlation of endwall losses in plane compressor cascades," Journal of Engineering for Power, Transactions of ASME, Vol. 90, pp. 251-257, 1968.

67. Coles, D. E., "The law of the wake in the turbulent boundary layer," Journal of Fluid Mechanics, Vol. 1, No. 2, p. 191, 1956.

68. Stratford, B. S., "The prevention of separation and flow reversal in the corners of compressor blade cascades," Aeronautical Journal, pp. 249-256, 1973.

69. Peacock, R. E., "Boundary layer suction to eliminate corner separation in cascades of airfoils," ARC R & M 3663, 1971.

70. Hartmann, M. J., Benser, W. A., Hauser, C. H., and Ruggeri, R. S., "Fan and compressor technology," NASA SP-259, pp. 1-36, 1971.

71. Papailiou, K. D., "Review of the history of boundary layer calculation methods and the present state of the art," in Proceedings of the Workshop on Flow in Turbomachines (Ed. M. H. Vavra, K. D. Papailiou, and J. R. Wood), 1971.

72. Seyb, N., "Determination of cascade performance with particular reference to the prediction of boundary layer parameters," ARC Report 27, 214, 1965.

73. Seyb, N., "The role of boundary layers in axial flow turbomachines and the prediction of their effects," AGARDograph No. 164, pp. 241-259, 1972.

74. Dunham, J., "Prediction of boundary layer transition on turbomachinery blades," AGARDograph No. 164, pp. 55-71, 1972.

75. Dunham, J., "The effect of stream surface convergence on turbomachine blade boundary layers," Aeronautical Journal, Vol. 25, pp. 90-92, 1976.

76. Fogarty, L. E., "The laminar boundary layer on a rotating helical blade," Journal of Aeronautical Science, p. 247, 1951.

77. Horlock, J. H. and Wordsworth, J., "The three-dimensional laminar boundary layer on a rotating helical plate," Journal of Fluid Mechanics, Vol. 23, p. 305, 1965.

78. Banks, W. E. and Gadd, G. E., "A preliminary report on boundary layers on screw propellers and simpler rotating bodies," ARC R & M 3150, 1962.

79. Lakshminarayana, B., Jabbari, A., and Yamaoka, H., "Three-dimensional turbulent boundary layers on a single rotating helical blade," Journal of Fluid Mechanics, Vol. 51, p. 545, 1972.

80. Anand, A. K. and Lakshminarayana, B., "An experimental and theoretical investigation of three-dimensional turbulent boundary layer inside an axial flow inducer," NASA CR 2888, 207 pp., 1973.

81. Lakshminarayana, B. and Govindan, T. R., "Analysis of turbulent boundary layer on cascade and rotor blades of turbomachinery," Fifth International Symposium on Air Breathing Engines, Bangalore, India, 1981.

82. Johnston, J. P., "The effects of rotation on boundary layers in turbomachine rotors," Fluid Mechanics, Acoustics, and Design of Turbomachinery, (Ed., B. Lakshminarayana, W. R. Britsch, and W. Gearhart) NASA SP 304, 1974.

83. Litvai, E. and Preszler, L., "The velocity profile of a turbulent boundary layer on the blading of radial impellers," Proceedings of Third Conference on Fluid Mechanics and Fluid Machinery, Akademiai Kiado, Budapest, 1969.

84. Litvai, E. and Preszler, L., "On the velocity profile of the turbulent boundary layer on rotating impeller bladings," Periodica Polytechnica, Mechanical Engineering, Vol. 13, p. 215, 1969.

85. Staniz, J. D., "Design of two-dimensional channels with prescribed velocity distributions along the channel walls," NACA Report 1115, 1953.

86. Shekhar, P. N. R. and Norbury, J. F., "Design of aerofoils in two-dimensional cascades to support compressible prescribed velocity distribution," Report of Mechanical Engineering, Liverpool University, 1969.

87. LeFoll, J., "A theory of representation of the properties of boundary layer on a plane," Proceedings of Seminar on Advanced Problems in Turbomachinery, Von Karman Institute for Fluid Dynamics, 1965.

88. Papailiou, K. D., "Boundary layer optimization for the design of high turning axial flow compressor blades," Journal of Engineering for Power, Transactions of ASME, Vol. 93, 1971.

89. Loudet, C., "Dessin d'une aube de turbine de petite dimension au moyen de la methode d'optimisation des couches limites de Le Foll.," These Annexe, Universite de Libre de Bruxelles, 1971.

90. Huo, S., "Blade optimization based on boundary layer concepts," AGARDograph No. 164, pp. 141-170, 1972.

91. Huo, S., "Optimization based on the boundary layer concept for compressible decelerating flows," Von Karman Institute for Fluid Dynamics TN 111, 1975.

92. Perkins, H. J., "The formulation of streamwise vorticity in turbulent flow," Journal of Fluid Mechanics, Vol. 44, pp. 721-740, 1970.

93. Oldfield, M. L. G., Kiock, R., Holmes, A. T., and Graham, C. G., "Boundary layer studies on highly loaded cascades using thin films and a traversing probe," ASME Paper 80-GT-137, 1980.

94. Sharma, O. P., Bailey, D. A., and Blair, M. F., "Boundary layer development on turbine airfoil suction surface," ASME Paper 81-GT-204, 1981.

95. Meauze, G., "Transonic boundary layer on compressor stator blades as calculated and measured in wind tunnel," Fourth International Symposium on Air Breathing Engines, Orlando, Florida, 1979.

96. Walker, G. J., "Observations of separated laminar flow on axial compressor blading," ASME Paper 75-GT-63, 1975.

97. Moon, I. M., "Effects of coriolis force on the turbulent boundary layer in rotating fluid machines," M.I.T., G.T.L., Report No. 74, 1964.

98. Moore, J., "The development of turbulent boundary layers in centrifugal machines," M.I.T., G.T.L. Report No. 99, 1969.

99. Halleen, R. M. and Johnston, J. P., "The influence of rotation on flow in a long rectangular channel--An experimental study," Stanford University Report MD-18, 1967.

100. Gorton, C. A. and Lakshminarayana, B., "A method of measuring three-dimensional mean flow and turbulence characteristics inside a rotating turbomachinery blade passage," Journal of Engineering for Power, Transactions of ASME, Vol. 98, No. 2, pp. 137-146, 1976.

101. Reynolds, B. and Lakshminarayana, B., "Characteristics of lightly loaded fan rotor blade wakes," NASA Contractor Report 3188, 1979.

102. Ravindranath, A., "Three-dimensional mean and turbulence characteristics of the near wake of a compressor rotor blade," M.S. Thesis, The Pennsylvania State University, 1979.

103. Lieblein, S., "Loss and stall analysis of compressor cascades," Journal of Basic Engineering, Transactions of ASME, Vol. 81, pp. 387-400, 1959.

104. Stewart, W. L., Whitney, W. J., and Wong, R. Y., "A study of boundary layer characteristics of turbomachine blade rows and their relation to overall blade losses," Journal of Basic Engineering, Transactions of ASME, Vol. 82, pp. 588-592, 1960.

105. Schlichting, H., "Application of boundary layer theory in turbomachinery," Journal of Basic Engineering, Transactions of ASME, Vol. 81, pp. 543-551, 1959.

106. Papailiou, K. D., "Correlations concerning the process of flow deceleration," Journal of Engineering for Power, Transactions of ASME, Vol. 97, pp. 295-300, 1975.

107. Herring, H. J. and Mellor, G. L., "Computer program for calculating laminar and turbulent boundary layer development in compressible flow," NASA CR-2068, 1972.

108. Sheets, H. E., "The slotted blade axial-flow blower," Transactions of ASME, Vol. 78, pp. 1683-1690, 1959.

109. Sheets, H. E. and Brancourt, C. P., "A multistage slotted blade axial flow pump," Journal of Engineering for Power, Transactions of ASME, Vol. 88, pp. 105-110, 1966.

110. Armstrong, W. D., "An experimental investigation of secondary flow occurring in a compressor cascade," Aeronautical Quarterly, Vol. 8, pp. 240-256, 1957.

111. Horlock, J. H., "Recent developments in secondary flows," in Secondary Flows in Turbomachines, AGARD CP 214, 1977.

112. Horlock, J. H. and Lakshminarayana, B., "Secondary flows: Theory, experiment and application in turbomachinery aerodynamics," Annual Review of Fluid Mechanics, Vol. 5, p. 247, 1973.

113. Lakshminarayana, B. and Horlock, J. H., "Review: Secondary flows and losses in cascades and axial flow turbomachines," International Journal of Mechanical Engineering Science, Vol. 5, pp. 287-307, 1963.

114. Lakshminarayana, B. and Horlock, J. H., "Generalized expressions for secondary vorticity using intrinsic coordinates," Journal of Fluid Mechanics, Vol. 59, No. 1, pp. 97-115, 1973.

115. Billet, M. L., "Secondary flow related vortex cavitation," Ph.D. Thesis, The Pennsylvania State University, 182 pp., 1978.

116. Lakshminarayana, B., "Effects of inlet temperature gradients on turbomachinery performance," Journal of Engineering for Power, Transactions of ASME, Vol. 97, pp. 64-74, 1975.

117. Lakshminarayana, B., "Three dimensional flow field in rocket pump inducers, Part 1: Measured flow field inside the rotating blade passage and at the exit," Journal of Fluids Engineering, Transactions of ASME, Vol. 95, p. 567, 1973.

118. Dixon, S. L., "Secondary vorticity in axial compressor blade rows," Fluid Mechanics, Acoustics and Design of Turbomachinery (Ed. B. Lakshminarayana, W. R. Britsch, and W. S. Gearhart), Part I, pp. 173-204, 1974.

119. Kawai, T. and Adachi, T., "Effects of hub ratio of axial flow fan on stator endwall flow," Bulletin of JSME, Vol. 22, pp. 521-528, 1979.

120. Adachi, T., Sashikuma, H. and Kawai, T., "Study of the secondary flow in the downstream of a moving blade row in an axial flow fan," Bulletin of JSME, Vol. 24, pp. 332-339, 1981.

121. Lakshminarayana, B., "Methods of predicting the tip clearance effects in axial flow turbomachinery," Journal of Basic Engineering, Transactions of ASME, Vol. 92, pp. 467-482, 1970.

122. Gessner, F. B., "The origin of secondary flow in turbulent flow along a corner," Journal of Fluid Mechanics, Vol. 58, pp. 1-25, 1973.

123. Renken, J. H., "Corner boundary layer and secondary flow within a straight compressor cascade," AGARD CP-214, Paper 21, 1977.

124. Gersten, K., "Corner interference effects," AGARD Report No. 299, 1965.

125. McCune, J. E. and Hawthorne, W. R., "The effects of trailing vorticity on the flow through highly-loaded cascades," Journal of Fluid Mechanics, Vol. 62, 1976.

126. Tan, C. S., "Vorticity modelling of blade wakes behind isolated annular blade-rows induced disturbances in swirling flows," Journal of Engineering for Power, Transactions of ASME, Vol. 193, pp. 279-287, 1981.

127. Dodge, P. R., "A numerical method for two dimensional and three dimensional viscous flows," AIAA Paper 76-425, 1976.

128. Ghia, K. N., Ghia, U., and Studerus, C. J., "Analytical formulation of three-dimensional laminar viscous flow through turbine cascades using surface oriented coordinates," ASME Paper 76-FE-22, 1976.

129. Ghia, K. N. and Sokhey, J. S., "Laminar incompressible viscous flow in curved ducts of rectangular cross-sections," Journal of Fluids Engineering, Transactions of ASME, Vol. 99, p. 640, 1977.

130. Briley, W. R. and McDonald, H., "An approximate analysis for three-dimensional viscous subsonic flows with large secondary velocities," SRA Report R78-3000014, 1978.

131. Dunham, J., "A review of cascade data on secondary losses in turbines," Journal of Mechanical Engineering Science, Vol. 12, pp. 48-59, 1970.

132. Gersten, K., "Results of systematic investigations on secondary flow losses in cascades, Part I: Secondary flow losses in compressor cascades of profile NACA 8410," Institut fur Stromungsmechanik, TH Braunschweig, Report No. 54/29a, 1955.

133. Scholz, N., "Systematic investigation on secondary flow losses in cascades," Institut fur Stromungsmechanik, T. H. Braunschweig, Report No. 56/184, 1957.

134. Salvage, J. W., "Investigation of secondary flow behavior and end-wall boundary layer development through compressor cascades," Von Karman Institute for Fluid Dynamics Technical Note 107, 1974.

135. Moiseev, N., Lakshminarayana, B., and Thompson, D. S., "Noise due to interaction of boundary layer turbulence with a compressor or a propulsor rotor," AIAA Paper 76-568, 1976.

136. Trunzo, R., "The effect of inlet turbulence and strut generated disturbances on turbomachinery noise," M.S. Thesis, The Pennsylvania State University, 1981.

137. Huard, J. C., "Influence de distorsions initiales sur les ecoulements secondaires dans une grille d'Aubes annulaire fixe," AGARD CP-214, Paper 6, 1977.

138. Fujie, K., "A study of flow through the rotor of an axial compressor--Evaluation of drag coefficients," Bulletin of JSME, Vol. 5, No. 18, 1962.

139. Thompkins, W. T. and Kerrebrock, J. L., "Exit flow from a transonic compressor rotor," M.I.T., G.T.L. Report 123, 1975.

140. Gallus, H. E. and Kummel, W., "Secondary flows and annulus wall boundary layers in axial flow compressor and turbine stages," AGARD CP 214, Paper 4, 1977.

141. Barry, B., Oral presentation at the AGARD Conference on "Secondary Flows in Turbomachinery," at the Hague, The Netherlands, 1977.

142. Came, P., "Secondary loss measurements in a cascade of turbine blades," Institution of Mechanical Engineering, Conference Proceedings 3, pp. 75-83, 1973.

143. Morris, A. W. H. and Hoare, R. G., "Secondary loss measurements in a cascade of turbine blades with meridional wall profiling," ASME Paper 75-WA/GT-13, 1975.

144. Lakshminarayana, B. and Horlock, J. H., "Leakage and secondary flows in compressor cascades," ARC R & M No. 3483, 1967.

145. Gustafson, G. A., "Some observations from low-speed cascade tests concerning side wall boundary layer suction," AGARD CP-214, Paper 19, 1977.

146. Meauze, G., "Effet des ecolements secondaires dans les grilles d'aubes," AGARD CP-214, Paper 10, 1977.

147. Horlock, J. H., Louis, J. F., Percival, P. M. E. and Lakshminarayana, B., "Wall stall in compressor cascades," Journal of Basic Engineering, Transactions of ASME, Vol. 88, p. 637, 1966.

148. Schlegel, J. C., Liu, H. C. and Waterman, W. F., "Reduction of end-wall effects in a small, low aspect ratio turbine by radial work redistribution," Journal of Engineering for Power, Transactions of ASME, Vol. 98, pp. 130-136, 1976.

149. Taylor, E. S., Stevenson, R. and Dean, R. C., "The control of secondary flow in the wall boundary layers of axial turbomachines," M.I.T., G.T.L. Report No. 27-4, 1954.

150. Senoo, Y., Taylor, E. S., Batra, S. K. and Hinck, E., "Control of wall boundary layer in an axial compressor," M.I.T., G.T.L. Report No. 59, 1960.

151. Deich, M. E. and Zaryankin, A. E., "Method of increasing the efficiency of turbine stages with short blades," Translations No. 2816, AEI (Manchester) Ltd., T. P./T2816, 1960.

152. Kopper, F. C., Milano, R. and Vanco, M., "An experimental investigation of endwall profiling in a turbine vane cascade," AIAA Paper 80-1089, 1980.

153. Due, H. F., Easterling, A. E. and Rogo, C., "Cascade research on a small, axial, high work, cooled turbine," ASME Paper 75-GT-62, 1975.

154. Ewen, J. S., Huber, F. W. and Mitchell, J. P., "Investigation of the aerodynamic performance of small axial turbines," Journal of Engineering for Power, Transactions of ASME, Vol. 95, pp. 326-332, 1973.

155. Goldman, L. J. and McLallin, K. L., "Effect of endwall cooling on secondary flows in turbine stator vanes," AGARD CP 214, Paper 15, 1977.

156. Sieverding, C. H. and Wilputte, Ph., "Influence of Mach number and endwall cooling on secondary flows in a straight nozzle cascade," Journal of Engineering for Power, Transactions of ASME, Vol. 103, pp. 257-264, 1981.

157. Peacock, R. E., "Blade tip gap effects in turbomachines, A review," Naval Postgraduate School Report NPS 67-81-016, 1981.

158. Reeder, J. A., "Tip clearance problems in axial compressors (A survey of available literature)," Report No. K-1682, Union Carbide Corporation, 62 pp., 1968.

159. Jefferson, J. L., "Some practical effects of tip clearance in turbine blading," Transactions of North East Coast Institution of Engineers and Shipbuilders, Vol. 70, p. 49, 1954.

160. Wu, C. H. and Wu, W., "Analysis of tip-clearance flow in turbomachines," Polytechnic Institute of Brooklyn, G.T.L. TR No. 1, 1954.

161. Rains, D. A., "Tip clearance flow in axial flow compressors and pumps," Mechanical Engineering Lab. Report 5, C.I.T., 1954.

162. Betz, A., "The phenomena at the tips of Kaplan turbines," Hydraulische Probleme, 1925.

163. Lewis, R. I. and Yeung, E. H. C., "Vortex shedding mechanisms in relation to tip clearance flows and losses in axial fans," ARC R & M No. 3824, 1977.

164. Croner, H. M. and Yeh, H., "Tip clearance research on an unshrouded compressor rotor," GEC Report No. R59FPD963, 1959.

165. Bollay, W. A., "A non-linear wing theory and its application to rectangular wings of small aspect ratio," Z. Angew. Math. Mech., Vol. 19, pp. 21-35, 1939.

166. Sugiyama, Y., "A theory for rectangular wings with small tip clearance in a channel," Vol. 24, pp. 103-119, 1973.

167. Dean, R. C., Jr., "The influence of tip clearance on boundary layer flow in a rectilinear cascade," M.I.T., G.T.L. Report No. 27-3, 1954.

168. Gearhart, W. S., "Tip clearance flow in turbomachines," M.S. Thesis, The Pennsylvania State University (see also Journal of Aircraft, Vol. 3, No. 2, 1966, pp. 185-192), 1964.

169. Hubert, G., "Untersuchungen uber die sekundarverluste in axialen turbomachinen," VDI Forschungsheft No. 496, 1963.

170. Novoderezhkin, R. A., Karelin, V. Y., and Demidov, V. V., "Experimental studies on tip clearance cavitation," Proceedings of Fifth Conference on Fluid Machinery, Budapest, Hungary, 1975.

171. Hurlimann, R., Discussion of Traupel, 1970, Ref. 178.

172. Williams, A. D., "The effect of tip clearance flows on performance of axial flow compressors," A. E. Thesis, C.I.T., 1960.

173. Ufer, H., "Analyse der geschwindigkeitsverteilung an den schaufelspitzen von axialgeblasen," Technische Mitteilungen Krupp (Forschungs berichte), Vol. 26, No. 2, pp. 33-45 (see also NASA TT F-16366), 1968.

174. Ryan, F. J. and Ohashi, H., "The effect of tip clearance on the performance of an axial flow fan," M.S. Thesis, M.I.T., 1955.

175. Thinh, N. D., "Contribution a l'etude de l'ecoulement au voisinage de l'extremite des pales d'un rotor," Thermique et Aeraulique, Vol. 5, pp. 449-502, 1971.

176. Fabri, J. and Reboux, J., "Effect of outer casing treatment and tip clearance on stall margin of a supersonic rotating cascade," ASME Paper 75-GT-95, 1975.

177. Jefferson, J. L. and Turner, R. C., "Some shrouding and tip clearance effects in axial flow compressors," Transactions of the North East Coast Institution of Engineers and Shipbuilders, Vol. 74, pp. 78-101, 1958.

178. Traupel, W., "Ergebnisse von Trubinenversuchen am Institut fur Thermische Turbomachinen an der ETH, Zurich," Flow Research on Blading (Ed. L. S. Dzung), pp. 88-150, 1970.

179. Stobbe, H., Discussion of Traupel, 1970, Ref. 178.

180. Rogo, C., "Experimental aspect ratio and tip clearance investigation on small turbines," SAE Paper 680448, 1968.

181. Haas, J. E. and Kofskey, M. G., "Effect of rotor tip clearance and configuration on overall performance of a 12.77 centimeter tip diameter axial-flow turbine," ASME Paper 79-GT-42, 1979.

182. Flot, R., "Contribution a L'etude des ecoulements secondaires dan les compresseurs axiaus," These de Docteur-Ingenieur, Universite de Lyon, 1975.

183. Pandya, A. and Lakshminarayana, B., "Investigation of tip clearance flow inside and at the exit of a compressor rotor passage, Part 1: Mean velocity field," ASME Paper 82-GT-12 (to be published in Journal of Engineering for Power), 1982.

184. Hesselgreaves, J. E., "A correlation of tip clearance/efficiency measurements on mixed-flow and axial-flow turbomachines," Proceedings of Third Conference on Fluid Mechanics and Fluid Machinery, 1969.

185. Vavra, M. H., Aero-thermodynamics and flow in turbomachines, John Wiley and Sons, pp. 374-383, 1960.

186. Smith, L. H., "The effect of tip clearance on the peak pressure rise of axial flow fans and compressors," ASME Symposium on Stall, 1958.

187. McNair, R. E., "Tip clearance effects on stalling pressure rise in axial flow compressors," ASME Symposium on Compressor Stall, Surge, and System Response, pp. 47-50, 1960.

188. Beitler, R. S., Saunders, A. A. and Wanger, A. A., "Fuel conservation through active control of rotor clearances," AIAA Paper 80-1087, 1980.

189. Booth, T. C., Dodge, P. R., and Hepworth, H. R., "Rotor tip leakage Part 1: Basic methodology," Journal of Engineering for Power, Vol. 104, No. 1, pp. 154-161, 1982.

190. Patel, K. V., "Research on a high work axial gas generator turbine," SAE Paper No. 800681, 1980.

191. Kofskey, M. G. and Allen, H. W., "Smoke study of nozzle secondary flows in a low-speed turbine," NACA TN 3260, 1954.

192. Watanabe, I., Referenced in Senoo (1971), 1969, ref. 196.

193. Lakshminarayana, B., "Techniques for aerodynamics and turbulence measurements in turbomachinery rotors," Journal of Engineering for Power, Transactions of ASME, Vol. 103, pp. 374-392, 1981.

194. Horlock, J. H., "Boundary layer problems in axial turbomachines," in Flow Research on Blading, Brown Boveri Symposium, (Ed. L. S. Dzung), 1970.

195. Otsuka, S., "Theory of secondary flow in cascades," Memoirs of the Faculty of Engineering, Nagoya University, Vol. 29, No. 2, pp. 165-231, 1977.

196. Senoo, Y., "Shear flow, vortices and secondary flow," Memoirs of the Faculty of Engineering, Kyushu University, Vol. 30, No. 3, pp. 69-86, 1971.

197. Bailey, D. A., "Study of mean- and turbulent-velocity fields in a large-scale turbine-vane passage," ASME Paper 79-GT-33, 1979.

198. Kummel, W., "Untersuchung der verlustbehofteten raumlichen stromung in einem axial verdichter mit tesonderer beriicksichtigung der seitenwane-grenzschichten," Doktor-Ingenieur Dissertation, Technischen Hochschule Aachen, 1976.

199. Squire, H. B. and Winter, K. G., "The secondary flow in a cascade of airfoils in a non-uniform stream," Journal of the Aeronautical Sciences, pp. 271-277, 1951.

200. Eskay, L. E., "Douglas Neumann cascade source program and Douglas Neumann plotting program," Applied Research Laboratory, The Pennsylvania State University, TM 506 2491-24, 1968.

201. Lakshminarayana, B., Discussion of the paper by Wilson et al., NASA SP 304, Vol. 1, pp. 127-130, 1974.

202. Loos, H. G., "Analysis of flow in the stator of an axial flow turbomachine," Cal. Inst. Tech. Report No. 53, 1953.

203. Treaster, A. L., "Computerized application of the streamline curvature method to the indirect, axisymmetric turbomachine problem," TM 514.2491-16, Applied Research Laboratory, The Pennsylvania State University, 1969.

204. Smith, L. H., "Three-dimensional flow in axial-flow turbomachinery--Part 1," Report No. I-14, Johns Hopkins University, 1953.

205. Lakshminarayana, B., "An axial flow compressor facility with instrumentation for relative flow measurement," Journal of Fluids Engineering, Transactions of ASME, Vol. 102, 1980.

206. Carter, A. D. S. and Hughes, H. P., "A theoretical investigation into the effect of profile shape on the performance of aerofoils in cascade," ARC R & M No. 2384, 1946.

207. Venkatarayaln, N., Prithvi Raj, D. and Narayanamurthi, R. G., "Influence of freely rotating inlet guide vanes on the return flows and stable operating range of an axial flow fan," Journal of Engineering for Power, Transactions of ASME, Series A, 1980.

208. Kolesnikov, Yu. N., "Investigation of losses of total pressure in the inlet guide vane of an axial flow compressor," in Blade Machines and Jet Devices, FTD-MT-24-69-68, 1968.

209. Treaster, A. L. and Yocum, A. M., "The calibration and application of five hole probes," ISA Transactions, Vol. 18, No. 3, pp. 23-34, 1979.

210. Lakshminarayana, B. and Davino, R., "Mean velocity and decay characteristics of the guide vane and stator blade wake of an axial flow compressor," Journal of Engineering for Power, Transactions of ASME, Vol. 102, No. 1, pp. 50-60, 1980.

211. Sitaram, N. and Lakshminarayana, B., "Semi-annual progress report to NASA on compressor endwall flows," 1976.

APPENDIX A

ENDWALL FLOW MOMENTUM INTEGRAL EQUATIONS

Introduction

The objective of the analytical investigation is to model the end wall flows including leakage and secondary flows, casing and blade boundary layers and to include it in the analysis and design of axial flow compressors. The following momentum integral equations include the effect of both the casing and the blade boundary layer flow.

Assumptions

The following assumptions are made in the analysis of end wall momentum integral equations.

1. Flow is incompressible and steady relative to the rotor.
2. Blade camber is small.
3. Coles velocity profile is assumed for the blade boundary layer velocity in the θ direction and Mager's velocity profile is assumed for the blade boundary layer velocity in the r direction.
4. β in the blade boundary layer is assumed to be constant in the tangential direction.

Approach

The time-averaged equations of continuity and momentum are written in rotating cylindrical coordinate system (see Figure 44). The momentum equations are integrated in θ-direction. The integration is carried in three regions: 1) blade boundary layer on pressure side, 2) annulus wall boundary layer region between the two blade boundary layers, and 3) blade boundary layer on suction side. In integrating momentum equations in blade boundary layers, Cole's profile for the axial velocity and Mager's profile for the radial velocity are used. The momentum equations are then integrated in the radial direction within the annulus wall boundary layer.

Momentum Integral Formulation

Using the blade to blade averaged continuity equation and momentum equations, the momentum integral equations in terms of the annulus wall and blade boundary layer parameters are formulated by Sitaram and Lakshminarayana [211].

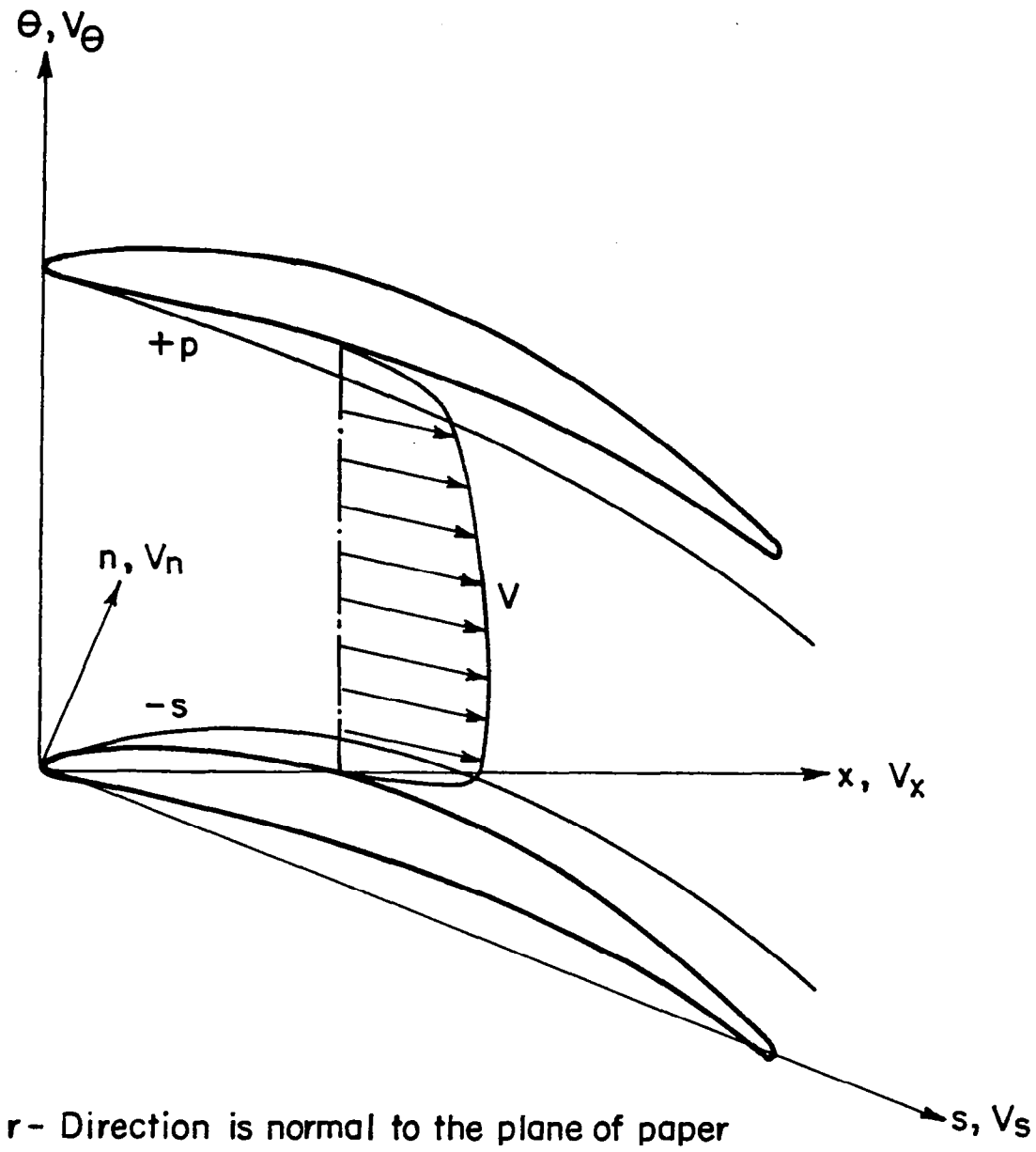

Figure 44. Coordinate System Used in the Endwall Flow Momentum Integral Equations Formulation

All the pressure gradient and shear stress terms, including those in the blade boundary layer, were retained in the momentum integral equations. Since it would be impossible to solve the momentum integral equations with all these terms, some of the shear stress and pressure gradient terms, whose magnitudes are negligible, are dropped from these equations. Furthermore, the turbulent normal stresses are neglected.

With these assumptions, the momentum integral equations can be written as follows: [211]. The symbols are defined in Appendix B and the nomenclature.

The Z momentum integral equation is,

$$\frac{\partial \theta_x^*}{\partial x} + (2+H_x)\frac{\theta_x^*}{\bar{V}_e}\frac{\partial \bar{V}_e}{\partial x} - \frac{1}{\bar{V}_e}\int_{r_t-\delta_t}^{r_t}\left(\frac{\partial \bar{V}_e}{\partial x} + \bar{\bar{X}}\right)dr - \frac{(\theta_{rx}^* - \delta_r^*)}{r_m}$$

$$= \frac{1}{\rho \bar{V}_e^2}\int_{r_t-\delta_t}^{r_t}\left[-\frac{\partial \bar{p}}{\partial x} + \frac{\Delta p}{\theta_a r}\tan\beta\right] + \frac{1}{\theta_a}\left[\frac{2\bar{\tau}_{bx}}{r} - \frac{\partial}{\partial x}(I_1 + I_1^*) + \frac{\partial}{\partial x}(I_2 + I_2^*)\right.$$

$$\left. + \frac{1}{r}\frac{\partial}{\partial r}(I_3 + I_3^*)\right] + \rho\frac{C_1}{\theta_a r}\left[\frac{\partial}{\partial x}(C + C^*) + \frac{\partial}{\partial r}(D + D^*)\right]dr - \frac{\bar{\tau}_{tx}}{\rho \bar{V}_e^2} \qquad (A1)$$

where $\bar{\tau}_{tx}$ is pitch averaged shear stress at the casing in the x-direction and $\bar{\tau}_{tx} = \bar{\tau}_o \cos \bar{\varepsilon}_o$, where $\bar{\tau}_o$ is pitch averaged shear stress at the casing and $\bar{\varepsilon}_o$ is the pitch averaged limiting streamline angle at the casing.

The r momentum integral equation is,

$$\frac{\partial \theta_r}{\partial r} + \frac{\partial}{\partial r}(\theta_{rx}^* + \delta_x^*) + \frac{1}{\bar{V}_e}\left[(2\theta_{rx}^* + \delta_x^* + \delta_t)\frac{\partial \bar{V}_e}{\partial x} - \int_{r_t-\delta_t}^{r_t}\frac{\partial \bar{V}_e}{\partial x}dr\right]$$

$$+ \frac{1}{r_m}(\theta_r^* - \delta_r^*) - \frac{1}{\bar{V}_e^2}\int_{r_t-\delta_t}^{r_t}\left[\bar{V}_e\bar{\bar{X}} + \frac{\overline{V_x^2\tan^2\beta}}{r_m} + \overline{2\Omega V_x \tan\beta}\right.$$

$$\left. + \Omega^2(r + \delta^* + \delta)\right]dr = \frac{1}{\rho \bar{V}_e^2}\int_{r_t-\delta_t}^{r_t}\left[\frac{\partial \tau_{xr}}{\partial x} - \frac{\partial \bar{p}}{\partial r} + \frac{2}{r}\frac{\bar{\tau}_{br}}{\theta_a}\right]$$

$$+ \frac{1}{\theta_a}\left[-\frac{\partial}{\partial r}(I_1 + I_1^*) + \frac{1}{r}\frac{\partial}{\partial x}(I_3 + I_3^*) + \frac{1}{r}\frac{\partial}{\partial r}(I_5 + I_5^*) + p_p\frac{\partial \theta_p}{\partial r}\right.$$

$$- p_s\frac{\partial \theta_s}{\partial r} - \frac{\rho C_1}{\theta_a r}\frac{\partial}{\partial x}(D + D^*) + \frac{\partial}{\partial x}(E + E^*) + \overline{(C\tan^2\beta + C^*\tan^2\beta^*)}$$

$$\left. + \frac{2\Omega r}{C_1}\overline{(A\tan\beta + A^*\tan\beta^*)}\right]dr \qquad (A2)$$

where

C_1, C_2, C_3	Constants in Cole's velocity profile
C_4	$C_3 - 1$
C_5	$C_3 - 1/2$
C_6	$C_2\ (1 - 4/\pi^2)$
C_7	$\frac{C_3}{3} - \frac{1}{9}$
C_8	$C_2\ (\frac{1}{3} - \frac{2}{\pi^2})$
C_9	$C_4 + C_7$
C_{10}	$C_2 - C_6 + C_8$
C_{11}	$(C_3 - 2)\ C_3$
C_{12}	$2C_3 - 3C_3 + \frac{2C_2}{\pi}\ Si(\pi)$
C_{13}	$C_3C_4 + 1/2$
C_{14}	$C_2^2\ (\frac{3}{2} - 8/\pi^2)$
C_{15}	$C_{12} - \frac{8}{\pi} - \frac{6C_2}{\pi}\ Si(\pi)$
C_{16}	$(2 + 4/\pi)\ C_2$
C_{17}	$2(C_4 - C_5 - \frac{4}{9}\ C_3)$
C_{18}	$(2C_2^2 - C_{14} + \frac{4C_2^2}{\pi^2}\ )$
C_{19}	$2C_2\ (\frac{4}{3} + \frac{2}{\pi^2}) + C_{16}$
C_{20}	$C_{12} + C_{15} + 2C_3\ (\frac{1}{3} - \frac{2}{\pi^2}) + C_2\ (\frac{7}{9} + \frac{2Si(\pi)}{\pi})$
C_{21}	$C_{11} + C_{13} + .2 + C_3\ (\frac{C_3}{3} - \frac{2}{9})$

C_{22} $\quad 1/5$

C_{23} $\quad 2C_4 - 4C_5 + 4(C_3 - \frac{1}{3}) + \frac{1}{2} - \frac{2}{25} + C_3\ (\frac{2}{5} + \frac{1}{2})$

C_{24} $\quad \frac{3}{2}\ C_2^2 - 2C_{14} + 6C_2\ (\frac{1}{2} + \frac{4}{\pi^2}) + (\frac{1}{5} - \frac{3}{2})\ C_2^2 + 8C_2$

C_{25} $\quad C_{12} - 2C_{15} - 2C_3\ (\frac{21}{25} + \frac{8}{\pi^2} + \frac{24}{\pi^4}) + C_2(\frac{74}{\pi}\ Si(\pi) + \frac{11}{2})$

C_{26} $\quad 2C_3 - 2C_{16} + 48C_2\ (\frac{1}{\pi^2} - \frac{2}{\pi^4})$

$Si(\pi)$ $\quad \int_o^t \frac{\sin t}{t}\ dt$

$\bar{U}$ $\quad \ln\ (\frac{V_\tau \delta}{\nu})$

$$\bar{\bar{X}} = \frac{C_1}{\theta_a r}\ [\frac{\partial}{\partial x}\ (A + A^*) + \frac{\partial}{\partial r}\ (B + B^*)]$$

$$A = V_\tau \cos\beta\ \delta\ (\bar{U} + C_2 \Pi + C_4)$$

$$A^* = V_\tau^* \cos\beta^* \delta^*\ (\bar{U} + C_2\ \Pi^* + C_4)$$

$$B = V_\tau \delta\ \varepsilon_o\ (\frac{\bar{U}}{3} + C_9 + C_{10}\ \Pi)$$

$$B^* = V_\tau^*\ \delta^*\ \varepsilon_o^*\ (\frac{\bar{U}^*}{3} + C_9 + C_{10}\ \Pi^*)$$

$$C = V_\tau^2 \cos^2\beta\ \delta\ [U^2 + 2C_4 U + \frac{3}{2}\ C_2^2 \Pi^2 + 2C_2 \Pi U + C_{11} + C_{12}\Pi]$$

$$C^* = V_\tau^{*2} \cos^2\beta^*\ \delta^*\ [\bar{U}^{*2} + 2C_4 \bar{U}^{*2} + \frac{3}{2}\ C_2^2 \Pi^{*2} + 2C_2 \Pi^* \bar{U}^* + C_{11} + C_{12}\Pi]$$

$$D = V_\tau^2\ \varepsilon_o \cos\beta\ \delta\ [\frac{U^2}{3} + C_{17} U + C_{18} \Pi^2 + C_{19} \Pi \bar{U} + C_{20} \Pi + C_{21}]$$

$$D^* = V_\tau^{*2}\ \varepsilon_o^* \cos\beta^*\ \delta^*\ [\frac{\bar{U}^{*2}}{3} + C_{17} \bar{U}^* + C_{18} \Pi^{*2} + C_{19} \Pi^* \bar{U}^* + C_{20} \Pi^* + C_{21}]$$

$$E = V_\tau^2\ \varepsilon_o^2\ \delta\ [C_{22} \bar{U}^2 + C_{23} \bar{U} + C_{24} \Pi^2 + C_{25} \Pi + C_{26} \Pi \bar{U} + C_{27}]$$

$$E^* = V_\tau^{*2}\ \varepsilon_o^{*2}\ \delta^*\ [C_{22} \bar{U}^{*2} + C_{23} \bar{U}^* + C_{24} \Pi^{*2} + C_{25} \Pi^* + C_{26} \Pi^* \bar{U}^* + C_{27}]$$

$$I_1 = \int_{\theta_s}^{\theta_s+\theta_1} p\,d\theta \qquad I_1^* = \int_{\theta_p-\theta_2}^{\theta_p} p\,d\theta$$

$$I_2 = \int_{\theta_s}^{\theta_s+\theta_1} \tau_{rx}\,d\theta \qquad I_2^* = \int_{\theta_p-\theta_2}^{\theta_p} \tau_{rx}\,d\theta$$

$$I_3 = r\int_{\theta_s}^{\theta_s+\theta_1} \tau_{rx}\,d\theta \qquad I_3^* = r\int_{\theta_p-\theta_2}^{\theta_p} \tau_{rz}\,d\theta$$

$$I_4 = \int_{\theta_s}^{\theta_s+\theta_1} \tau_{x\theta}\,d\theta \qquad I_4^* = \int_{\theta_p-\theta_2}^{\theta_p} \tau_{x\theta}\,d\theta$$

$$I_5 = r\int_{\theta_s}^{\theta_s+\theta_1} \tau_{rr}\,d\theta \qquad I_5^* = r\int_{\theta_1-\theta_2}^{\theta_p} \tau_{rr}\,d\theta$$

$$I_6 = r\int_{\theta_s}^{\theta_s+\theta_1} \tau_{r\theta}\,d\theta \qquad I_6^* = r\int_{\theta_p-\theta_2}^{\theta_p} \tau_{r\theta}\,d\theta \qquad \text{(A3)}$$

θ_1 - Edge of boundary on suction side, degrees

θ_2 - Edge of boundary on pressure side, degrees

θ_a - Angular pitch of inviscid region, degrees

In the above terms, the starred quantities refer to boundary layer on pressure side of the blade. Subscript t refers to the annulus wall boundary layer. All momentum integral parameters are derived for the annulus wall boundary layer.

Equations A1 and A2 are still complex. Some further information regarding pressure and shear stresses in the annulus wall boundary layer and blade boundary layer is necessary to solve these equations to determine θ^*_{xx} and V_τ.

Other annulus wall boundary layer parameters such as δ^*_x, etc. can be related by means of the shape factor.

APPENDIX B

DEFINITIONS OF BOUNDARY LAYER THICKNESSES

Cartesian (x,θ,r) Coordinate System

DELTA $$\delta^* = \frac{1}{V_e}\int_o^\delta (V_e - V)\, dr$$

DELTAX $$\delta_x^* = \frac{1}{V_e}\int_o^\delta (V_{x_e} - V)\, dr$$

DELTAT $$\delta_\theta^* = \frac{1}{V_e}\int_o^\delta (V_{\theta_e} - V)\, dr$$

DELTAR $$\delta_r^* = \frac{1}{V_e}\int_o^\delta V_r\, dr$$

THETA $$\theta^* = \frac{1}{V_e^2}\int_o^\delta (V_e - V)\, V\, dr$$

THETAXX $$\theta_x^* = \frac{1}{V_e^2}\int_o^\delta (V_{x_e} - V_x)\, V_x\, dr$$

THETAXT $$\theta_{x\theta}^* = \frac{1}{V_e^2}\int_o^\delta (V_{x_e} - V_x)\, V_\theta\, dr$$

THETAXR $$\theta_{xr}^* = \frac{1}{V_e^2}\int_o^\delta (V_{x_e} - V_x)\, V_r\, dr$$

THETATX $$\theta_{\theta x}^* = \frac{1}{V_e^2}\int_o^\delta (V_{\theta_e} - V_\theta)\, V_x\, dr$$

THETATT $$\theta_\theta^* = \frac{1}{V_e^2}\int_o^\delta (V_{\theta_e} - V_\theta)\, V_\theta\, dr$$

THETATR $$\theta_{\theta r}^* = \frac{1}{V_e^2}\int_o^\delta (V_{\theta_e} - V_\theta)\, V_r\, dr$$

THETARX $$\theta_{rx}^* = \frac{1}{V_e^2}\int_o^\delta V_r\, V_x\, dr$$

THETART $$\theta^*_{r\theta} = \frac{1}{V_e^2} \int_o^\delta V_r \, V_\theta \, dr$$

THETARR $$\theta^*_{rr} = \frac{1}{V_e^2} \int_o^\delta V_r^2 \, dr$$

DEFECT $$D_f = \frac{1}{V_e^2} \int_o^\delta (V_{x_e} \, V_{\theta_e} - V_x \, V_\theta) \, dr$$

Streamline (s,n,r) Coordinate System

$$V_s = V \cos (\alpha - \alpha_e) \quad ; \quad V_n = V_{\sin} (\alpha - \alpha_e)$$

DELTAS $$\delta^*_s = \frac{1}{V_e} \int_o^\delta (V_{s_e} - V_s) \, dr$$

DELTAN $$\delta^*_n = \frac{1}{V_e} \int_o^\delta V_n \, dr$$

THETASS $$\theta^*_s = \frac{1}{V_e^2} \int_o^\delta (V_{s_e} - V_s) \, V_s \, dr$$

THETASN $$\theta^*_{sn} = \frac{1}{V_e^2} \int_o^\delta (V_{s_e} - V_s) V_n \, dr$$

THETANS $$\theta^*_{ns} = \frac{1}{V_e^2} \int_o^\delta V_n \, V_s \, dr$$

THETANN $$\theta^*_{nn} = \frac{1}{V_e^2} \int_o^\delta V_n^2 \, dr$$

THETANR $$\theta^*_{nr} = \frac{1}{V_e^2} \int_o^\delta V_n \, V_r \, dr$$

THETARS $$\theta^*_{rs} = \frac{1}{V_e^2} \int_o^\delta V_s \, V_r \, dr$$

THETARN $$\theta^*_{rn} = \theta^*_{nr}$$

1. Report No.	2. Government Accession No.	3. Recipient's Catalog No.
NASA CR-3671		

4. Title and Subtitle	5. Report Date
END WALL FLOW CHARACTERISTICS AND OVERALL PERFORMANCE OF AN AXIAL FLOW COMPRESSOR STAGE	February 1983
	6. Performing Organization Code
7. Author(s)	8. Performing Organization Report No.
N. Sitaram and B. Lakshminarayana	PSU/TURBO 82-5
	10. Work Unit No.
9. Performing Organization Name and Address	
The Pennsylvania State University Department of Aerospace Engineering 153 Hammond Building University Park, Pennsylvania 16802	11. Contract or Grant No. NSG-3032
	13. Type of Report and Period Covered
12. Sponsoring Agency Name and Address	Contractor Report
National Aeronuatics and Space Administration Washington, D. C. 20546	14. Sponsoring Agency Code 505-15-83 (E-1514)

15. Supplementary Notes

Final report. Project Manager, Peter M. Sockol, Fluid Mechanics and Acoustics Division, NASA Lewis Research Center, Cleveland, Ohio 44135.

16. Abstract The existing literature on the complex endwall flows in the axial flow turbomachines is reviewed critically. This review also indicates the possible future directions for research on endwall flows in axial flow compressors. Theoretical investigations on the rotor blade endwall flows in axial flow compressors reported here include the secondary flow calculation and the development of the momentum integral equations for the prediction of the annulus wall boundary layer. The equations for secondary vorticity at the rotor exit are solved analytically. The solution includes the effects of rotation and the viscosity. The momentum integral equations derived include the effect of the blade boundary layers. The axial flow compressor facility of the Department of Aerospace Engineering at The Pennsylvania State University, which is used for the experimental investigations of the endwall flows, is described in some detail. The overall performance and other preliminary experimental results are presented. Extensive radial flow surveys are carried out at the design and various off design conditions. These are presented and interpreted in this report. The following experimental investigations of the blade endwall flows are carried out. 1) Rotor blade endwall flows: The following measurements are carried out at four flow coefficients. (a) The rotor blade static pressures at various axial and radial stations (with special emphasis near the blade tips). (b) The hub wall static pressures inside the rotor blade passage at various axial and tangential stations. 2) IGV endwall flows: The following measurements are carried out at the design flow coefficient. (a) The boundary layer profiles at various axial and tangential stations inside the blade passage and at the blade exit. These measurements are made with a five-hole probe of very small diameter (1.65 mm) head. The static and stagnation pressures and three components of mean velocities are obtained. (b) Casing static pressures and limiting streamline angles inside the blade passage. All these measurements are presented and interpreted in this report. The secondary flow is found to be strong in the inlet guidevane. Substantial effects of tip clearance are observed in the blade pressure distribution taken in the tip region of the blade.

17. Key Words (Suggested by Author(s))	18. Distribution Statement
Endwall flow; Axial compressor stage; Performance	Unclassified - unlimited STAR Category 02

19. Security Classif. (of this report)	20. Security Classif. (of this page)	21. No. of Pages	22. Price*
Unclassified	Unclassified	140	A07

* For sale by the National Technical Information Service, Springfield, Virginia 22161

NASA-Langley, 1983